Transport properties and coherence in $YBa_2Cu_3O_{7-\delta}$ submicron structures

Gianpaolo Papari

30th November 2009

Thesis submitted in partial fulfillment of the requirements for the degree of Doctor of Philosophy in Physics at University of Naples "Federico II"

Contents

To Ely my immortal love

Introduction

The research activity has been mostly focused on the study of the transport properties of high critical temperature superconductor (HTS) nanostructures. The experiments have been carried on $YBa_2Cu_3O_{7-\delta}$ (YBCO) submicron samples. This is one of the very first systematic studies of HTS devices at these length scales and represents an intermediate step towards the pure nanoscale transport experiments, whose dimensions should be closer also to the HTS coherence length. Study on nanostructures respond to strong fundamental motivations. The physics of superconductivity in structures with reduced dimensions is very intriguing and still unsettled, touching interesting arguments as quantum suppression of superconductivity in nanowires, the phase diagram of the superconductor-insulator transition, the dissipative dynamics induced by phase slips mechanism and, in perspective, the possibility of controlling the superconducting or insulating state of a nanowire by changing its environment. In complex oxides and strongly correlated systems, where the electrons self-organize in ways qualitatively different from those of conventional metals and insulators, nanoscale ordering and phase transition are among the most outstanding problems in physics today, and studies of nanoscale devices may have a formidable impact on that.

HTS nanowires have also great applicative potentials. Their short coherence lengths, which are a problem for several applications, turn to be very important to determine phase slips on a very short scale differently from low critical temperature superconductors, which are characterized by longer coherence lengths. As a consequence HTS nanowires can be scaled in principle to lower sizes.

Dimensions of the order of a few hundred nanometers guarantee a high level of homogeneity and reproducibility of physical phenomena, and give access to a series of experiments where the macroscopic quantum coherence manifest more pronounced properties than at larger scales. The measurements on nanobridges have been carried on samples with different widths while the nanorings have about the same size but differ for the doping. The transport measurements in magnetic field on nanobridges aim to investigate the transport in presence of high correlated vortices. The submicron rings have been designed to analyze the gauge invariance effects in HTS.

The thesis is divided in eight chapters. The first and second chapters give essential elements on the theory of superconductivity and on the main properties of the cuprates, which are of relevance for the discussion of the experiments. The third chapter is dedicated to the description of the process used for the fabrication of YBCO nanostructures. Bridges and rings have widths typically ranging from $1\,\mu m$ down to 150 nm. In the fourth chapter the set up for the measurements of transport properties is described along with the typical procedures we use. The measurements have been carried in a He3 cryostat we have equipped with two stages of filtering and shielded against electromagnetic noise. Experimental measurements are distributed in four different chapters. After an overview on the basic properties of the nanostructures, as the critical temperature (T_C) and the critical current density (J_C) as a function of the width of the channel (chapter 5), the current-voltage (I-V) characteristics are described in chapter 6. $I-V$ curves of microbridges of width down to about 150 nm are highly reproducible and both (T_C) and J_C well scale with the width of the channel. Reproducibility is poor for widths below 100 nm even if we have superconducting wires also for widths down to 60 nm at relatively high temperatures (20 K). These results can be compared with the best and very few results available in literature on HTS nanostructures. From I-V curves and the temperature dependence of J_C, indications on flux dynamics and dissipation in nanobridges are obtained. In the last two chapters magnetoresistance measurements on nanobridges and nanorings are presented respectively. These provide additional elements on flux dynamics and macroscopic coherence in superconducting mesoscopic structures.

Part I: Theoretical background.

Chapter 1

Basic concepts of low and high critical temperature superconductivity

In this chapter are described the fundamental properties of superconductivity. Following the historical development of theory of superconductivity the London's, Ginzburg-Landau and BCS theories are presented respectively. Then the Lawrence and Doniach model is introduced. This model is the extension of the Ginzburg-Landau theory to the layered high critical temperature superconductors. The chapter is concluded with a comment on the gauge invariance in hollow superconductors and the Little and Parks effect.

1.1 The perfect conductivity and perfect diamagnetism

Superconductivity was discovered by Kamerlingh Onnes in 1911 by measuring the mercury resistance as function of the temperature. The scientist found that below a critical temperature (T_C) the metal resistance rapidly fell down to zero. The zero resistance state in superconducting ring has been largely proved by measuring the magnetic field emitted from circulating currents. Measurements have proved the dissipationless state of circulating supercurrents which did not show any decay also after years. The phenomenon of the perfect conductivity has been the first hallmark characterizing the *superconductivity*(SC). Twenty-two years later, Meissner and Ochsenfeld (1933) discovered another property of superconductors: the perfect diamagnetism. This is the second hallmark of the superconductivity, that refers to the complete magnetic field exclusion by the interior of a superconductor. Nevertheless perfect conductivity and perfect diamagnetism are properties in common also with a normal metal with zero resistivity. The supercon-

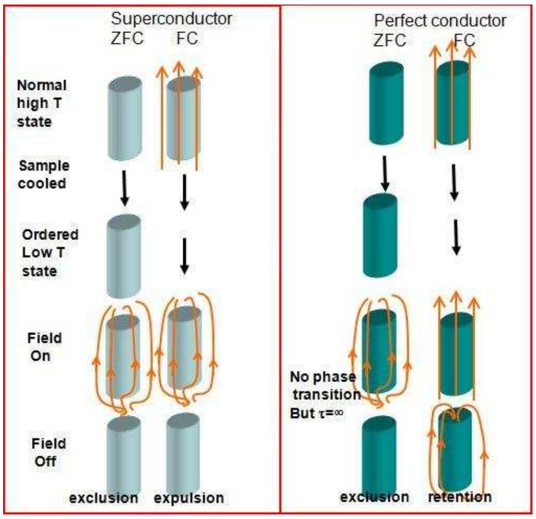

Figure 1.1: schematic experiment to distinguish the perfect conductivity from superconductivity.

ductivity is thermodynamical state different from the normal state. The easiest experiment showing the difference between the perfect- and superconductivity is depicted in figure 1.1.

If we start cooling through T_C and then we apply a magnetic field both a perfect conductor and the superconductor would exclude the field. The perfect conductor excludes the field by means of screening currents induced by Faraday's law. In principle also the superconductor would exclude the magnetic flux for the same mechanism, but in this case it more appropriate to say that the field is expelled because of the Meissner effect. If we now reverse the order by first applying the magnetic field and then cooling through T_C, the superconductor and the perfect metal behave differently. The superconductor expels the field (Meissner effect) instead the perfect conductor remain fully permeated by the field. As opposed to a perfect conductor a superconductor experiences a phase transition, when it is cooled through T_C. This means that the transition depends only on the evolution of its thermodynamic variables (H, T) and not by its *history*. However a superconductor can exhibit the Meissner effect as long as the external magnetic field is smaller than a critical field H_c. For each temperature exists a precise magnetic field at which the superconductivity disappears.

1.2 The London's equations

The London-London equations describe the classical properties of a superconductor,

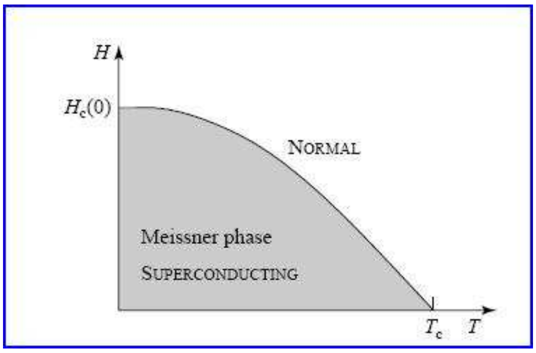

Figure 1.2: The Meissner phase of a superconductor. Under the curve, in the shaded area, the material is perfectly screened against an external magnetic field.

$$\vec{E} = \partial_t \Lambda \vec{J_s} \tag{1.1}$$

$$\vec{h} = -c\vec{\nabla} \times \left(\Lambda \vec{J_s}\right) \tag{1.2}$$

$$\Lambda = \frac{4\pi\lambda^2}{c^2} = \frac{m}{n_s e^2} \tag{1.3}$$

.

In the above equations $\vec{E}$ is the electric field $\vec{J_s}$ is the supercurrent density "h" is the magnetic field density, n_s is the density of superconducting electrons and Λ is a phenomenological parameter. λ is the London penetration depth and represents the distance at which the magnetic field can penetrate into the superconductor. The equation 1.1 describes the perfect conductivity while the equation 1.2 is related to magnetic field expulsion. The former equation states that the super-electrons subjected to an electric field accelerate continuously while the latter one refers to a phenomenon that was discovered by Meissner and Ochsenfeld in 1933 and is also called the Meissner effect. The London penetration depth λ is one of the two length (the second is the coherence length) that defines the behavior of a superconductor in presence of an external magnetic field. It is a meaningful parameter since its value is related to the the superfluid density 1.2. It is worthwhile to notice that the second London equation asserts that the magnetic field and the current are joined variables. In a superconductor the supercurrent can flow only in a layer as deep as the London penetration depth.

1.3 The Ginzburg-Landau Theory

The London's equations(LE) consider the superfluid density a constant in the volume of the superconductor. This assumption limits enormously the applicability of London equations to real systems where generally the superfluid density n_s is a function strictly dependent on spatial variables. Ginzburg and Landau proposed a theory capable to study systems where the superfluid was spatial dependent. In fact the novelty of GL theory with respect to the London one resides in the introduction of an order parameter, a complex pseudo-wavefunction, whose square modulus retrieves the London superfluid density as function of spatial variables

$$|\Psi(\vec{r})|^2 = n_s(\vec{r}) \tag{1.4}$$

.

The GL theory is developed by postulating that the order parameter $\Psi\vec{r}$ is small and varies slowly in the space. Hence the Helmotz free energy of the superconducting system, immersed in a magnetic field of density "h", can be expanded in series of Ψ and $\nabla\,\Psi$ leading to the parametric equation

$$f_s = f_n + \alpha\,|\Psi|^2 + \frac{\beta}{2}\,|\Psi|^4 + \frac{1}{2m*}\left|\left(\frac{\hbar}{i}\nabla - \frac{e*}{c}\vec{A}\right)\right|^2 + \frac{h^2}{8\pi} \tag{1.5}$$

with m^* and e^* the mass and the electric charge of superconducting electrons, which typically are assumed to take the double value of the elementary charge in the normal state of the mean, i.e. $m^* = 2m_e$ and $e^* = 2e$. In order to get the equilibrium configuration the variational principle is applied. Imposing the minimum of the free energy, integrated on the system volume, with respect to the variation of the order parameter and of the vector potential two equations are gained

$$\frac{1}{2m^*}\left(\frac{h}{i}\nabla - \frac{e^*}{c}\vec{A}\right)^2\Psi + \beta|\Psi|^2\,\Psi = -\alpha(T)\Psi \tag{1.6}$$

$$\vec{J_s} = \frac{e^*\hbar}{i2m^*}\left(\overline{\Psi}\nabla\Psi - \Psi\nabla\overline{\Psi}\right) - \frac{e^{*2}}{m^*c}|\Psi|^2\vec{A} \tag{1.7}$$

The equation 1.7 matches with the definition of the Schroedinger current for a quantum particle of charge $2e^*$ and mass 2m. Within the GL framework the superfluid assumes the role of a single particle described by a single (pseudo) wave function $\Psi = |\Psi|e^{i\phi}$. Hence substituting the the complex order parameter Ψ in the equation 1.7 and using the definition of generalized momentum the supercurrent density acquires the simple form

$$\vec{J_s} = \frac{e^*}{m^*}|\Psi|^2\left(\hbar\nabla\phi - \frac{e^*}{c}\vec{A}\right) = e^*|\Psi|^2\vec{v}_s \tag{1.8}$$

The equation 1.6 resembles the Schroedinger equation but supplied with non linear terms. According to what mentioned at the end of the previous paragraph in a system whose transversal dimensions are strictly smaller than λ and taking into account that the GL theory holds for small Ψ either, it is reasonable to keep in the equation 1.6 only the linear terms in Ψ

$$\frac{1}{2m^*}\left(\frac{h}{i}\nabla - \frac{e^*}{c}\vec{A}\right)^2 \Psi = -\alpha(T)\Psi \tag{1.9}$$

One should consider that, in general, GL equations are solvable only numerically. Instead the equation 1.9 is the familiar hamiltonian equation whose solution lead to the Landau levels. The equation 1.9 is widely used for studying the response of a small superconductor immersed in a magnetic field. Furthermore the above equation allows to get a better confidence with a fundamental parameter in GL theory, the coherence length. Indeed, since the alpha parameter is a kinetic energy it can be written as follows

$$\alpha(T) = \frac{\hbar}{2m^*\,\xi(T)^2} \tag{1.10}$$

The coherence length represents the distance at which the order parameter can vary without the system undergoes any energy increase[1]. The ratio between the London penetration depth and the coherence length defines the GL parameter

$$k = \frac{\lambda}{\xi} \tag{1.11}$$

The temperature dependance of the two lengthes is experimentally found to be [24]

$$\frac{\lambda(T)}{\lambda(0)} = \frac{1}{\sqrt{1-\left(\frac{T}{T_c}\right)^4}} \tag{1.12}$$

$$\frac{\xi(T)}{\xi(0)} = \frac{1}{\sqrt{1-\frac{T}{T_c}}} \tag{1.13}$$

so k is a constant that identify univocally the superconductor. Two classes of superconductors are formed depending wether k is bigger or smaller than 1. More precisely Abrikosov showed that the breakpoint is $1/sqrt2 \approx 0.7$. The class satisfying $k < (>)1$ are called superconductors of the first(second) type. The principal difference between I and II type resides in the way to react to an external magnetic field. The first type manifest a sharp breakdown (first order transition) of the superconducting phase when the external magnetic field reaches a critical value H_c, while the II type undergoes a phase that continuously absorbers the external field in what is named the mixed

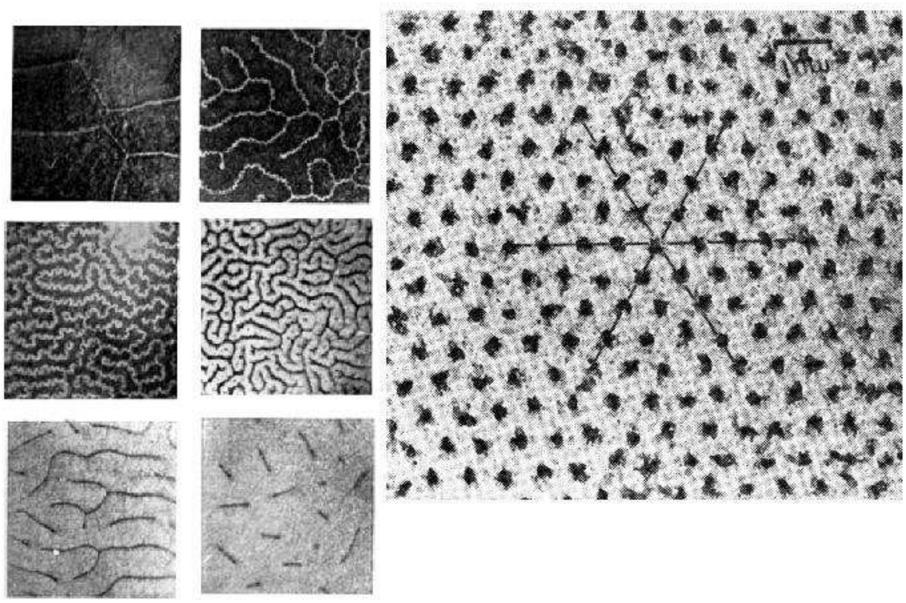

Figure 1.3: Left: Mendering laminar structure of first type superconductor immersed in a perpendicular magnetic field. Right: Abrikosov triangular lattice of quantum flux in a second type superconductor.

phase. Furthermore in the II type can be identified two different critical field, the first H_{c1} provides the value at which the field begins to enter the mean and the second H_{c2} marks the transition to the normal phase. The second type allows the entering of magnetic field through flux tubes each one carrying one quantum of flux

$$\phi_0 = \frac{h}{2e} = 2.07\,10^{-15} T\,m^2 \tag{1.14}$$

The flux tubes can be thought as vortices of current flowing around magnetic field line threading the sample. Abrikosov proved that at the equilibrium the vortices assume a particular configuration aiming to minimize the free energy of the system. As opposed to the second type the first type of superconductors make possible to the external magnetic field to enter inside, but in shape of laminar foils. In here the magnetic field lines penetrate forming intricate patterns which continuously move[24]. In figure 1.3 are presented the two types of superconductors subjected to a perpendicular magnetic field. On the right the Abrikosov lattice has assumed the triangular configuration.

Within the GL theory is possible to achieve the relations between the critical magnetic field the magnetic penetration depth and the coherence length[brandt]

$$B_{c1} = \frac{\Phi_0}{4\pi\,\lambda^2}\left(\ln(k+0.5)\right) \qquad B_c = \frac{\Phi_0}{\sqrt{8}\pi\xi\lambda} \qquad B_{c2} = \frac{\Phi_0}{2\pi\xi^2} = \sqrt{2}kB_c \tag{1.15}$$

B_c is the unique critical field for I type superconductors and B_{c1-c2} define the first and second critical field in type II superconductors. It is interesting to note that the B_{c1} formula depends on k only by a logarithm, so for low temperature superconductors, characterized by small values of k can be dropped, but it is not true for high critical temperature superconductors. In fact the high critical temperature superconductors are called strong II type superconductors, because are characterized by a huge k value. For instance the YBCO has $k \approx 100$ because the coherence length is incredibly small, on the order of 1-2 nm and the London penetration depth is typically 150 nm[19]. The comparison between low and high critical temperature vortices can be verified using the niobium k value that is about 1-2[5].

1.4 The Lawrence Doniach model

One of the most important feature of YBCO is its layered structure[1]. The electric conduction in this compound is enhanced in some planes of its elementary cell, so as long as the c-axis coherence length is smaller than the distance between the conducting planes the transport is two-dimensional. The superconducting transport in stacks of two dimensional layers affect mainly the vortex properties especially in terms of thermal fluctuations, and consequently the dissipation dynamic in terms of vortex creep/flow(see chapter 3). Now will be introduced the formalism of the Lawrence Doniach model that basically is the extension of the Ginzurg Landau theory to anisotropic systems. Following [1] we rewrite the GL free energy in system composed of a stack of layers. By using the crystallografic notation it is assumed that the current flows in the ab planes and the c axis is parallel to the z axis. Defining "s" as the distance between the conducting planes the equation 1.5 becomes

$$F = \sum_n \int \alpha|\Psi_n|^2 + \frac{1}{2}\beta|\Psi_n|^4 + \frac{\hbar^2}{2m_{ab}}\left(\left|\frac{\partial\Psi_n}{\partial x}\right|^2 + \left|\frac{\partial\Psi_n}{\partial y}\right|^2\right) + \frac{\hbar^2}{2m_c\, s^2}|\Psi_n - \Psi_{n-1}|^2 \; dV \tag{1.16}$$

In the the above equation the anisotropy turn out only in the c and ab directions because the anisotropy intrinsic anisotropy in the ab plane can be neglected especially in YBCO. In addition the derivative in z-direction has been replaced by a division with respect to interlayer distances because s is in general very small. Indeed typical interlayer distances holds 12 Å for YBCO([6] and references therein). If now the order parameter is expressed via the complex form $\Psi_n = |\Psi_n|e^{i\,\phi_n}$ the last term of 1.16 becomes

$$\frac{\hbar^2}{m_c\, s^2}|\Psi_n|^2\,[1-\cos{(\phi_n-\phi_{n-1})}] \tag{1.17}$$

that resembles the Josephson energy coupling between two adjacent layer. In order to get the GL equation for a single Layer we minimize with respect to Ψ^* achieving

$$\alpha\Psi_n+\beta|\Psi_n|^2\Psi_n-\frac{\hbar^2}{2\,m_{ab}}\left(\frac{\partial^2}{\partial_{x^2}}+\frac{\partial^2}{\partial_{y^2}}\right)\Psi_n-\frac{\hbar^2}{2\,m_c\,s^2}\left(\Psi_{n+1}-2\Psi_n+\Psi_{n-1}\right)=0 \tag{1.18}$$

and again the c axis coupling has been expressed in a discrete form. Defining as ∇ and $\vec{A}$ the gradient operator and the vector potential in the ab-plane we can write the full form of the Lawrence and Doniach equation

$$\alpha\Psi_n+\beta|\Psi_n|^2\Psi_n-\frac{\hbar^2}{2m_{ab}}\left(\nabla-i\frac{2e}{\hbar\,c}\vec{A}\right)\Psi_n-\frac{\hbar^2}{2m_c\,s^2}\left(\Psi_{n+1}e^{-i\frac{2e}{\hbar\,c}A_z}-2\Psi_n-\Psi_{n-1}\,e^{i\frac{2e}{\hbar\,c}A_z}\right)=0 \tag{1.19}$$

In anisotropic superconductors both the coherence length and the penetration depth depend on the crystallographic orientation, consequently the relation between λ, ξ an critical field has to be written(that, without subscripts is the generalized formula of 1.15)

$$1\sqrt{2}\pi\,H_c(T)\,\xi_i(T)\,\lambda_i(T)=\Phi_0 \tag{1.20}$$

where "i" refers to crystallographic axis. It is important to stress that physics phenomena depends strictly on the layered structure only if $\xi_c \geq s$ [1]. The temperature at which the dynamic skip from the tridimensional to bidimensional affect mostly the vortex dynamic.

1.5 The history of the Bardeen, Cooper, Schrieffer theory

The discovery of the isotope effect by Maxwell (1950) and Reynolds et al. (1950) has given the first hint on the mystery of superconductivity. This phenomenon establishes that $T_C \propto M^{-\alpha}$, where M is the ionic mass and $\alpha \approx 1/2$, and gives strong support to the view that superconductivity is the result of the electron-phonon interaction. Another relevant issue concerns the impossibility to derive the superconducting properties by using a perturbation theory. In fact, Shafroth (1958) proved that the Meissner effect could only be obtained by going beyond perturbation theory in treating the effective interaction between electrons.
In 1955 Bardeen considered the problem by employing the quantum field

theory and invited Cooper to join the effort since CooperŠs background was in particle physics. Bardeen stressed the importance of an energy gap in the excitation spectrum and that superconductivity is due to a condensation in momentum space of a coherent superposition of normal-state configurations. Another problem was associated to the scale energies. The correlation energy in the normal phase is of order 1 eV per electron, while the energy distinguishing the normal and super phases(the excitation gap) is of order 10^{-6} eV per electron. With the aid of the Landau's Fermi liquid theory, the excitation was treated with a correspondence with the free electron gas so enabling to isolate the small condensation energy that separates the normal and the superconducting phase. Cooper in 1956 studied the problem of two electrons interacting through an attractive effective potential above a frozen Fermi sea. He found that the normal state is unstable independently on how weak is the attraction. Bardeen, Cooper, and Schrieffer (1957) then studied a reduced Hamiltonian which included interactions involving only paired states,

$$H = \sum_{k,s} \epsilon_k \, n_{k,s} + \sum_{k,\,k'} V_{k,\,k'} \, b_k^\dagger \, b_{k'} \tag{1.21}$$

where $b_k^\dagger$ creates an electron pair $(k \uparrow, \, -k \downarrow)$ and ϵ_k represent the normal energies of quasi particles measured with respect to the chemical potential. Schriffer constructed a trial function for a variational problem in analogy with Tomonaga approach to the pion nucleon problem

$$\Psi = \prod_k \left(u_k + v_k \, b^\dagger \right) |0 > \tag{1.22}$$

where the parameters u and v are found by using $u_k^2 + v_k^2 = 1$ and another the minimization of energy with respect to, say, v_k. The solution of the problem yields the equation

$$\Delta_k = \sum_{k'} V_{k\,k'} \, \Delta_{k'} / E_{k'} \tag{1.23}$$

with

$$v_k^2 = \frac{1}{2} \left(1 - \frac{\epsilon_k}{E_k} \right) \tag{1.24}$$

and

$$E_k = \sqrt{\Delta_k^2 + \epsilon_k^2} \tag{1.25}$$

The excitation spectrum based exhibits quasiparticles energies E_k with an energy gap Δ_k. For k far above the Fermi surface the excitations are electronlike, and far below the Fermi energy they are holelike, while close k_F

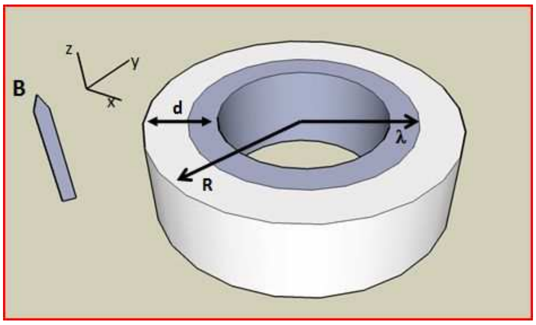

Figure 1.4: Sketch of a superconducting cylinder immersed in a perpendicular magnetic field. The darker region represents the space where the screening currents circulate.

they are an equal mixture of electron and hole, having charge zero but spin one-half. This is an example of charge-spin separation.
The BCS theory confirms the non locality of the electrodynamics derived by Pippard (1953). The electrons pair is delocalized in a distance equals to $\xi_0 = \hbar\, v_F / \pi \Delta$ that is called the coherence length(ξ). Magnetic flux trapped in a superconducting ring is predicted to be in units of $h/2e$. The first experimental proof of the pairing was performed by Deaver and Fairbank (1961) and by Doll and Nabauer (1961). GorŠkov in 1958 succeeded to deriving the Ginzburg-Landau phenomenological theory from the BCS theory.

1.6 The fluxoid quantization

The most important phenomena that proves the macroscopic quantum behavior of superconductivity is the fluxoid quantization. The term fluxoid was introduce by F. London to take into account of the whole phase acquired by a superconducting mean when it is subjected to an external magnetic field. The quantization effect is consequence of a constraint on the flux-periodicity of the phase of the order parameter.
Within the London theory a superconducting cylinder immersed in an axial magnetic field is pushed to generate circular Meissner currents that satisfy 1.2. The integration of the second London equation on a closed path yields to

$$\Phi = \int_{S_\gamma} \vec{H} \cdot d\vec{S} + \oint_{\gamma} \Lambda\, \vec{J}_s\, d\vec{l}. \tag{1.26}$$

The first term in the above equation is the contribution to the total flux due to $\vec{B}$, instead the second terms takes into account of the magnetic field produced by screening currents. According to 1.2, Φ would be zero if the superconducting sample was full, because the screening currents can compensate point by point the magnetic field entrance. In the other case Φ is not only different from zero but rather quantized. The right member of equation 1.26 embodies the phase of the superfluid (order parameter) after a cycle around the curve γ, this is evident applying the Stokes theorem to the external flux term in 1.26

$$\Phi = \frac{c}{2e} \oint_{\gamma} \left(m\,\vec{v}_s + \frac{2e}{c}\vec{A} \right) \cdot d\vec{l} \tag{1.27}$$

The above integrand is the generalized moment of the order parameter, that we can simply write as $\vec{p}$. Hence, within this notation, the phase factor of the order parameter holds

$$\Psi = |\Psi| \exp\left(\frac{i}{\hbar} \oint_{\gamma} \vec{p} \cdot d\vec{l} \right)$$

which acquire physical sense only if Ψ is a one-value wave function. This means that the phase difference after each complete turn can assume only a discrete set of values

$$\frac{c}{2e} \oint_{\gamma} \vec{p} \cdot d\vec{l} = n\frac{hc}{2e} = n\Phi_0 \tag{1.28}$$

$\Phi_0 = 2.07\,10^{-15}$ Tm^2 is the flux quanta. The condition 1.28 matches with the Bohr-Sommerfeld quantization condition for an electron stationary bonded to an atom. In order to "feel" the quantization of flux in the equation 1.28 the integration path has to include the magnetic field inside the hole and the anti-field produced by the screening current as well. Taking as reference the system described in figure 1.4, the latter condition leads to choose as integration path γ a curve whose radius is equal or bigger than the penetration depth λ. Extending the integration path beyond the penetration depth the first term on the right of equation 1.27 can be dropped ($J_s = 0$) providing the flux quantization. The first experiments on flux quantization were supplied independently by R. Doll & M. Nabauer(DN) and B. S. Deaver & W. M. Fairbank(DF)[7] in sample satisfying the condition. Before going further it is important to state that the original flux quantization, performed by F. London, implied a flux quanta periodicity $\Phi_0 = h/e$. Indeed the first couple of scientist (DN)found that the flux periodicity verified in their experiment showed some anomalies with respect the single electron flux quantum. Instead DF claimed that the flux trapped in the cylinder showed a periodicity more confident with $h/2e$.

Hence the fluxoid quantization established one of the most important basement of the BCS theory, namely that the superconducting fluid is composed by couples of electrons and not by single charges.

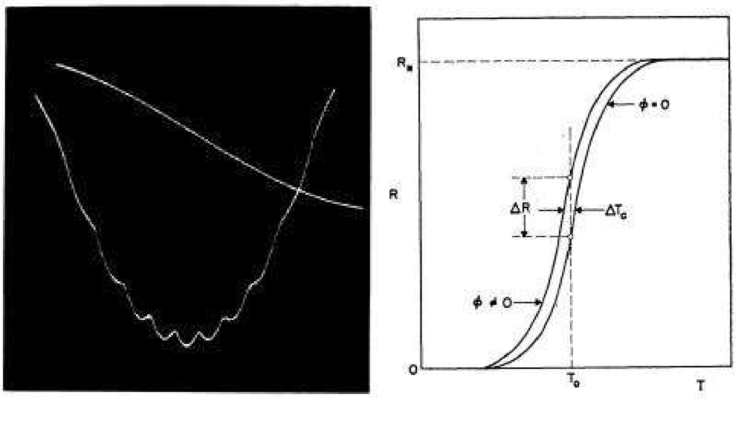

Figure 1.5: Left:Magneto-resistance measurement(parabolic-like curve) performed in the Little and Parks experiment. Right: Little and Parks hypothesis on the change of the resistive transition and hence of Tc when a perpendicular magnetic field is applied.

The quantization constraint on the sample dimensions might suggest that only in systems whose radial thickness is bigger than λ is possible observing the flux quantization, but it not true. However the experiments led by R. Doll, & M. Nabauer(DN) and B. S. Deaver & W. M. Fairbank(DF), were performed in superconducting cylinders having a wall thickness "d" bigger than λ. The first experiment showing the meaningless of the constraint $\lambda << d$ was performed one year later by W.A. Little and R. W. Parks and it will be discussed in the next section.

1.6.1 The Little and Parks effect

The flux quantization implies that the order parameter describing the superconducting state is a periodic function of the external magnetic field. Since the free energy of a superconductor f_s also depends on the order parameter it is trivial arguing that the free energy inherits the order parameter periodicity in not simply connected geometries[8]. Furthermore the free energy of the normal state f_n is independent on the order parameter therefore the critical temperature defined as the temperature Tc at which $f_s(Tc) = f_n$ must be a periodic function of the external magnetic field. This effect has been observed for the first time in small superconducting cylinder of tin in 1962[9]. Aiming to measure the phase diagram Tc(H) Little and Parks measured the magnetoresistance of a cylinder at a temperature close to the critical one. The experimental result is presented in the figure 1.5

Once magneto-resistance measurement was collected the two scientists hypothesized that the effect of the external magnetic field on the resistance consisted just in a horizontal translation of the resistive transition (see right

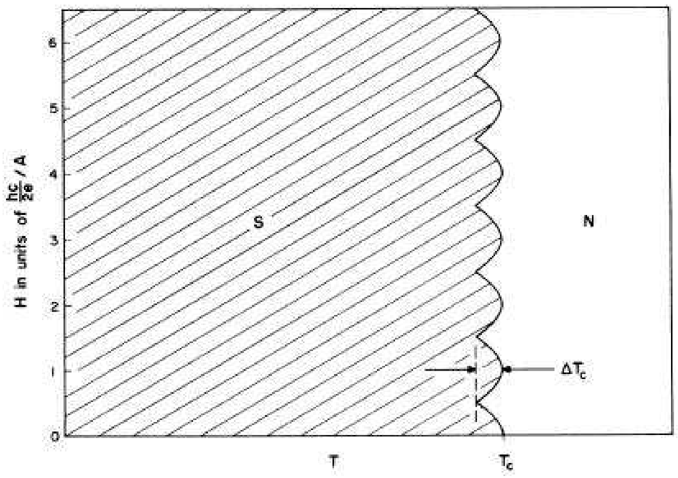

Figure 1.6: Little and Parks phase diagram.

panel of figure 1.5). As consequence the critical temperature oscillations can be provided once is monitored the resistance oscillations versus the magnetic field by using the formula

$$\triangle T_c \approx \triangle R(B) \left(\frac{\partial R}{\partial T}\right)^{-1} \tag{1.29}$$

The above assumption is true as long as the magnetoresistance is acquired close to T_C. The phase diagram reconstructed by Little and Parks is showed in the figure 1.6.

Little and Parks took into account of the critical temperature shift induced by the magnetic field by means of the BCS theory. They obtain,

$$\triangle T_c = \frac{\hbar^2}{16\, m^*\, R_0^2\, k_B} \left(\frac{\Phi}{\Phi_0} + n\right)^2 \tag{1.30}$$

where R_0 is the mean radius of the cylinder and k_B is the Botzmann constant. Another expression for the maximum relative variation of the critical temperature was achieved by Tinkham [8], that is just dependent on the superconducting parameter of the sample

$$\frac{\triangle T_c}{T_c} = \frac{\left(n\,\Phi_0 - \pi\, R^2\, H\right)^2}{8\,\pi^2\, R^2\, \lambda^2(0)\, H_{cb}^2(0)} \tag{1.31}$$

and H_{cb} is the bulk critical field. Nevertheless both formulas 1.30 and1.31 return substantially the same critical temperature change $\frac{\triangle T_c}{T_c}$, that in LP effect was on the order of 10^{-4}.

The Little and Parks effect differs from the two foregoing experiments on flux quantization because the cylinder thickness is pretty smaller than the London penetration depth. In this case the screening currents flow everywhere in the sample and it is not possible to choose a circular path with a radius bigger than λ along which the screening currents are null. If rather Little and Parks measured flux quantization, evidently the equation 1.27 has been misunderstood. In superconducting hollow cylinder/rings, clearly smaller than λ, the phase periodicity effect takes the name of fluxoid quantization. The first paper treating the dependance of flux periodicity by the cylinder thickness d (see figure **??**) was written by R. P. Gross and R. D. Parks(GP)[10].

Gross and Parks were completely in agreement with Tinkham calculations on the critical temperature shift calculated within the GL theory. In addition GP deduced that the quantization effect has to arise from the macroscopic quantum behavior of the screening current, and showed that the effect depend not only by the mean radius of the cylinder but on its thickness as well. The most important equation of the Gross and Parks article is the following

$$\frac{k^2}{\lambda^2} = \frac{1}{R_m^2}\left[(h-n)^2 + h^2\left(\frac{d}{2R_m}\right)^2 + n^2\left(\frac{d}{2R_m}\right)^2\left\{\frac{1}{3} + \frac{1}{5}\left(\frac{d}{2R_m}\right)^2 + o\left[\left(\frac{d}{2R_m}\right)^4\right]\right\}\right] \tag{1.32}$$

where R_m is the mean radius, $h = \pi R_m^2 H/\Phi_0$ and "d" is the thickness of the of the cylinder. The equation 1.32 displays on the left the thermal dependent critical field in terms of coherence length[1] and on the right a function of the flux depending on external magnetic field. Looking for the minima of equation 1.32 satisfying the condition $dh/dt = \infty$, where t=T/Tc is the reduced temperature, that means we are finding the relative minima of the critical temperature with respect a variation of the external magnetic field. The minima are

$$h_M = \frac{n}{1-(d/2R_m)^2} \tag{1.33}$$

which substituted in the equation 1.32 returns

$$\frac{k^2}{\lambda^2} = \frac{1}{R_m^2}\left[(h-h_M)^2\left\{1 + \left(\frac{d}{2R_M}\right)^2\right\} + \frac{1}{3}h_M^2\frac{d^2}{R_m^2}\left\{1 + \frac{7}{5}\left(\frac{d}{2R_m}\right)^2 + o\left[\left(\frac{d}{2R_m}\right)^4\right]\right\}\right] \tag{1.34}$$

The result described in the equation 1.34 essentially describes the two principal features of the Little and Parks effect. Indeed the first term justify the parabolas centered each $\Phi/\Phi_0 = n$ and the second explains the parabolic drift of parabolas minima when the magnetic field increases. Furthermore the Gross and Parks theory is implicitly stating that the effective fluxoid

---

[1] $H_{c2}(T) = \Phi_0/2_p i\xi^2(T)$

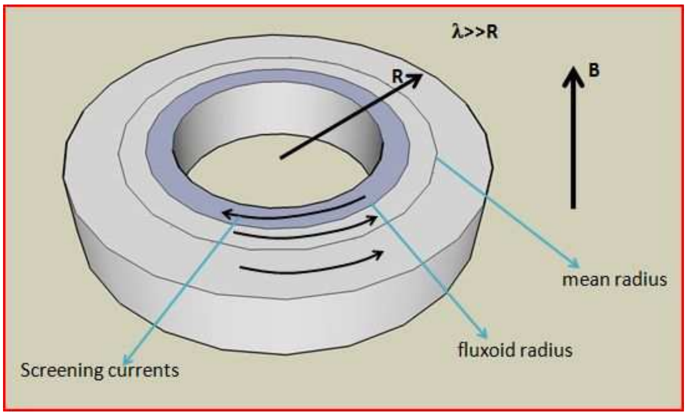

Figure 1.7: Sketch of the the screening currents directions in samples smaller than the penetration depth. λ

radius fall inside the cylinder thickness, and it does not match with the mean radius R_m. The effective radius that whose corresponds the minima in Tc versus H pattern satisfies the following relation[2]

$$R_{eff}^2 = \frac{R^2}{1 + \frac{1}{3}\left(\frac{d}{2R_m}\right)^2} \tag{1.35}$$

that is slightly smaller than the mean radius. The effective radius points to a line along which the critical current is null. Exactly the amount of the critical current flowing in the superconducting cylinder slice, limited by the internal radius and R_eff, satisfies the fluxoid quantization condition as sketched in figure 1.7. Another interesting outcome is suggested by noting that the embraced factor in the right side of 1.34 is basically just counting the flux quanta entering the cylinder, hence it can be deduced that the LP effect happens when [16]

$$\xi(T) \approx R_m$$

Other theoretical approaches mainly based on linearized GL equations have been developed to study the experimental pattern of the LP effect and on the other the screening current distribution inside a thick ring/annuli[11],[13],[19],[15],[28].

---

[2] dropping terms of the order of $\frac{d}{2R_m}{}^{4}$

Bibliography

[1] A. Barone and G. Paternò *Physics and applications of Josephson Effect* John Wiley & Sons 1982

[2] M. Tinkham *Introduction to superconductivity* (2ed., MGH, 1996)

[3] K. Fosseheim and A. Sudbø *Superconductivity Physics and Applications* John Wiley & Sons, (2004)

[4] J. E. *et al. Physical Review B* **76**, 134518, ; J. E. Sonier *et al. Physical Review Letters* **83**, 4156; L. E. Sonier *Physical Review Letters* **79**, 2875

[5] B. W. Mawfield and W. L. McLean *Physical Review* **139** A1515-A1522 (1965); Pradip Das *et al.*, *Physical Review B* **78** 214504(2008); J. Hua *et al Physical Review Letters* **101**, 077003 (2008)

[6] J. B. Bieri *et al. Physical Review B* **44**, 4709 (1991)

[7] B. S. Deaver and W. M. Fairbank *Physical Review Letters* **71**, 43 (1961); R. Doll and M. Nabäuer *Physical Review Letters* **71**, 51 (1961)

[8] M. Tinkham *Physical Review* **129**, 2413 (1963)

[9] W.A. Little and R. D. Parks *Physical review Letters* **9**, 9 (1962)

[10] R.P Gross and R. D. Parks *Physical review* **176**, 567 (1968)

[11] S. V. Yampolskii *et. al Physical Review B* **64**, 052504 (2001)

[12] Mathieu Morelle, *et al. Physical review B* **70**, 144528 (2004)

[13] Hu Zhao *et al. Solid State Communications* **125**, 59 (2003)

[14] G. Stenuit *et al.*, *Physica C* **322**, 277 (2000)

[15] V.V Moschchalkov *et al.*, *Physica C* **207**, 307 (1993)

[16] Nicholas C. Koshnick *et al.*,*Science* **318**, 1440 (2007)

Chapter 2

Properties of the Cuprates

In this chapter will be described the characteristics of cuprate materials, in terms of chemical structure, phase diagram as a function of doping, superconducting properties, and electronic transport dependance on critical temperature.

2.1 Chemical Structure and Doping

Cuprate materials have a stacked structure of perovskite-like crystals. The term perovskite denotes loosely all compounds (ferroelectrics, manganites, skutterudites, etc.) that have the crystal structure of the mineral $CaTiO_3$, and derives from the name of Russsian mineralogist, Perovski, who discovered this mineral.
In figure2.1, part A, is shown an ideal, cubic, perovskite structure of type ABX_3, where A and B indicate different positive charged ions, X the negative ones. This structure has BX_2 planes separated by AX planes, and his size is of the order of the large atomic radii of A and X ions, having B cations smaller radii.

Each B cation is surrounded by six anions, forming an octahedron.
In particular, in cuprates the CuO_2 planes correspond to the BX_2 planes, while AX planes may either be SrO or BaO planes. Moreover, in these materials the simple cubic structure is replaced by a tetragonal one.
Materials with perovskite-like structure tend to be ceramic-like and brittle, so that handle with them to fabricate high-Tc structures is non trivial. In particular, the material studied in these thesis is $YBa_2Cu_3O_{7-\delta}$ (YBCO), and his structure is reported in part B of figure2.1.

2.1.1 Doping of cuprates

Doping is the instrument that allows the cuprates to become superconducting. Usually, the dopant atoms are disposed in the AX (SrO or BaO) planes

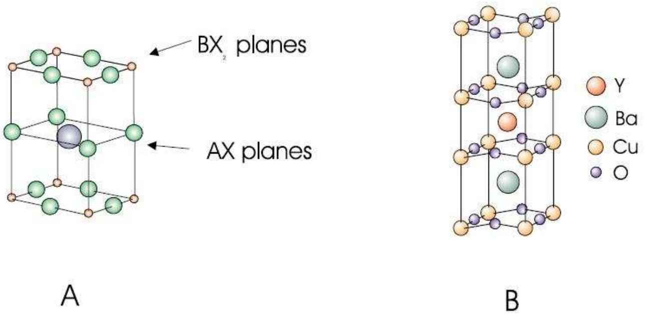

Figure 2.1: (A)Crystal structure ABX_3 of perovskite. (B)Crystal structure of YBCO, where the CuO_2 planes correspond to the BX_2 planes, the BaO planes to the AX ones.

interleaving the BX_2 (CuO_2) planes, and may be either cations with a different valence, or oxygen vacancies. Since the bond between AX and BX_2 layers has a ionic nature and have no free carries, the extra charge from the dopants is taken up in the BX_2 planes as an effective change in the B (Cu) valence.
In particular, in YBCO Cu is contained also in the interleaved layers with the structure $(BaO)(CuO_x)(BaO)$, forming CuO_x chains along the plane-to-plane directions, and the doping is obtained by changing the oxygen concentration in the CuO_x layers.
Figure 2.2 shows a general temperature versus doping phase diagram. In the extremely low doping side of the phase diagram the material is an antiferromagnetic (AF), Hubbard-Mott insulator with a Neel temperature of the order of hundred Kelvin. By increasing the doping, the first superconducting state with very low T_c is reached; then, as the doping increases, so T_c rises untill it levels off and begins to decrease.

Above T_c the phase of the system depends on the doping: for low doping the system is in the pseudo-gap (PG) regime. Some theories and experimental data suggest also the existence of a second crossover within the PG into another state. At higher doping the phase switches to the non-Fermi liquid state, indicated by Strange Metal in the figure. Finally, in the overdoped regime, the system reaches a metallic-like state, still not perfectly understood. There are many slight variants of this phase diagram used in the community, that substantially regard where, with respect to the doping concentration, the above-T_c phases begin and end.

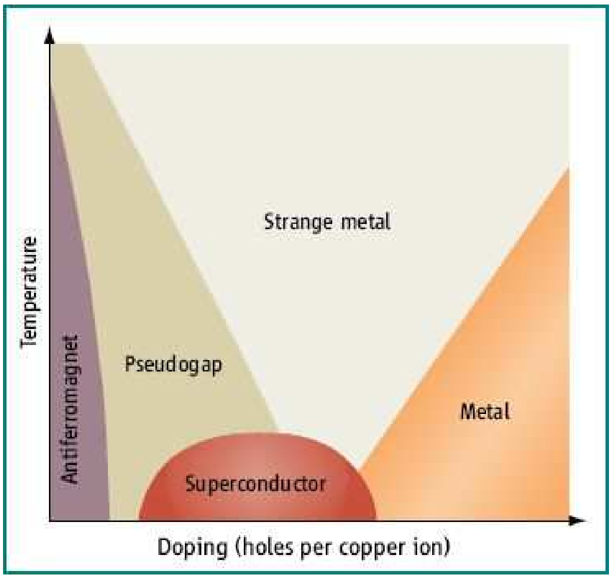

Figure 2.2: Phase diagram of YBCO

2.2 Superconducting properties

The most important superconducting feature for which cuprate materials are known is the high critical temperature T_c, but there are many other interesting properties that characterize them. In fact, they are hardly type II superconductors with extremely large second critical field H_{c2} (> 100 Tesla), and have very small coherence lengths ($\approx 1 - 3nm$) and large penetration depths ($\approx 100 - 500nm$). As explained in the previous section, the cuprates have a perovskite-like structure containing CuO_2 planes. Superconductive behavior has been theoretically predicted and experimentally verified in the cuprates only in these planes, while the superconductivity in the plane-to-plane direction is believed to occur via Josephson tunnelling. This means that all superconducting properties (coherence lengths, penetration depths, critical current densities, the critical fields, etc.) are highly anisotropic, with substantial differences between the in-planes and planes-to-planes directions. In particular, the order parameter is highly anisotropic within the in-planes, having 4 nodes, 4 lobes, and a sign change in the phase when going from lobe to lobe. Instead, no true plane-to plane order parameter exists because in this direction superconductivity occurs via Josephson tunnelling. An order parameter of this form is known as d-wave, in analogy with the orbitals of the hydrogen atom. It is relevant to underline that usually superconductors have an isotropic, constant phase order parameter, known as s-wave. The d-wave and s-wave order parameters are shown schematically in figure 2.3. The theoretical description of this property [1], [2], [3] has been successfully verified by experiments [4],[13],[6].

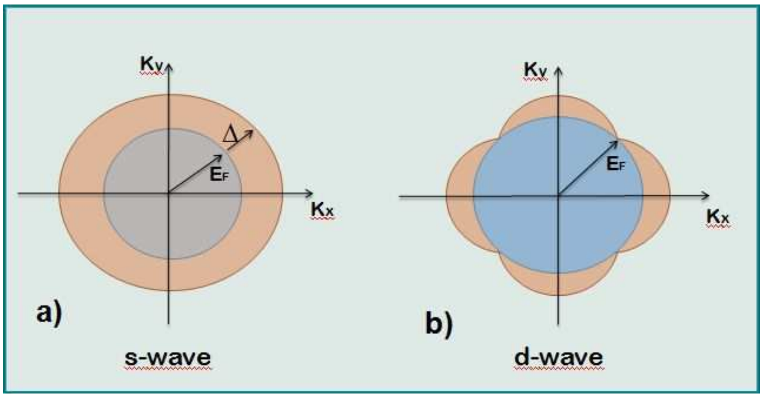

Figure 2.3: (a): S-wave order parameter in k-space. E_F is the Fermi energy, Δ is the superconducting gap; (b) D-wave order parameter

2.3 Electronic Transport

In the cuprates the charge carrier density is quite low, similar to the semi-conductors one. The main difference with the conductors, that have a high carrier density, is in the Coulomb interaction between electrons. In fact, while in conductors the electron states are extended and exist throughout the sample, in the semi-conductors these states are more localized due to Coulomb repulsions from neighboring electrons. The Coulomb interaction energy is given by

$$U = \frac{e^2}{4\pi\epsilon_0 r}, \tag{2.1}$$

where r is the electron spacing, while the kinetic energy by:

$$K = \frac{\hbar^2 k^2}{2m} \sim \frac{\hbar^2}{2mr^2} \tag{2.2}$$

Depending on r, one of the two terms prevails on the other and determines the conductor or the semi-conductor behavior. In particular, at low densities r is larger and the Coulomb term dominates and leads to an insulating (Mott) state because the carriers are trapped in Coulomb barriers. At high densities, instead, r is smaller and the electrons have enough kinetic energy to tunnel through the Coulomb barriers.

The Hubbard model describes the quantum-mechanic version of these two compelling terms with the following Hamiltonian:

$$H_{Hubbard} = -t \sum_{i,j,\sigma} c^{\dagger}_{i\sigma} c_{j\sigma} + U \sum_{i} n_i \uparrow n_i \downarrow \tag{2.3}$$

The first term is a tight-binding, independent-electron-model term, where t is the overlap integral of states of coordinates i and j; it creates an electron at site i with spin σ and removes an electron at site j with spin σ. The second term is the Coulomb term, that adds energy U when electrons with opposite spin occupy the same site. When $U = 0$ the standard tight-binding approximation applies: the system has a well defined Fermi surface and is described by the standard Fermi-liquid model. On the other hands, if U $\gg$ t and there is one carrier per site, an insulating, AF state with localized magnetic moments arises.

The description becomes more complicate in the intermediate regimes (U $\approx$ t), when no term is not dominant. For low doping, the system can show the so-called Hubbard bands, and the mobility of charges is in form of hopping. For what concerns the cuprates, it is known that the superconducting regime lies very close to the AF Mott insulator transition, but the true nature of the electronic structure in this regime is not known and there is still a debate on how the transport occurs, i.e. via Hubbard-band-like or in the Fermi liquid picture. The single Hubbard band model can demonstrare the electronic structure, but is too simple so most Hubbard models for the cuprates incorporate multiple Hubbard bands.

2.3.1 Transport in the cuprates above critical temperature

As mentioned above, no particular model that is generally accepted describes the transport in the cuprates in the superconducting regime, and experiments performed seem to be contradictory.

Focussing on the resistivity, ρ, in the non-superconducting state it is strongly dependent on direction, doping, and temperature. In particular, the planar CO_2 structure of cuprates leads to a 2-dimensional location of charge carrier density, and consequently, to an highly anisotropic resistivity when passing from the in-plane (a,b) directions to the plane-to-plane (c) direction. In fact, while for most cuprates the in-plane resistivities are $\rho_a \sim 2\rho_b$, ρ_c is typically higher than ρ_{ab} by an order of magnitude (YBCO) or more (BSCCO), and the anisotropy factor between them can vary enormously.

In most of the cases with an intermediate anisotropy the conduction in the c direction occurs via tunnelling and increases linearly with temperature T, while with an high anisotropy ρ_c increases with decreasing T suggesting a semiconducting or hopping behavior. In cuprates the resistivity is strongly related to doping. For very low doping they never become superconducting, and becomes insulating at low temperatures. For the over-doped case, instead, the resistivity is always linear, and never has an upward curvature or insulating phase. For cuprates having optimum or near optimum doping ρ_{ab} varies linearly with T and appears similar to that of a typical metal :

$$\rho = \frac{ne^2\tau}{m^*}, \tag{2.4}$$

where n is the carrier density, τ is the scattering relaxation time and $1/\tau$ the scattering rate. In a metal $\rho_{metal} \sim T$ and n doesn't depend on T, so the scattering rate, varies linearly with T.
In the optimally doped cuprates this linear behavior with T is more difficult to explain. Measurements of the Hall coefficient $R_H = 1/ne$, give indications about the carrier density and sign of the charge carriers. For most cuprates R_H is positive and the carriers are doped holes. Moreover, these measurement show that R_H varies linearly with T, implying that the scattering rate is proportional to T^2 rather than T.

Bibliography

[1] N. E. Bickers *et al.*, *Phys. Rev. Lett.* **62**, 961 (1989)

[2] P. Monthoux *et al.*, *Phys. Rev. Lett.* **67**, 3448 (1991)

[3] P. Monthoux and D. Pines, *Phys. Rev. Lett.* **72**, 1874 (1994)

[4] D. A. Wollman, *et al.*, *Phys. Rev. Lett.* **71**, 2134 (1993)

[5] C. C. Tsuei *et al.*, *Phys. Rev. Lett.* **73**, 593 (1994)

[6] F. Lombardi *et al.*, *Phys. Rev. Lett.* **89**, 207001 (2002)

Chapter 3

Fabrication of YBCO sub micron structures

This process is summarized in section 3.1. All single fabrication steps are then described in detail from section 3.2. The patterning process has been accomplished in collaboration with NEST (National Enterprise for nanoScience and nanoTechnology).

3.1 YBCO submicron structures fabrication

We have used c-axis YBCO thins films with thickness typically ranging between 50 nm and 100 nm. The YBCO films have been deposited by magnetron sputtering (sections 3.2, 3.3, 3.4). Films of different morphology and surface roughness were employed for testing. In what follows, we focus on 50 nm thick films with roughness less than 2 nm. Films were covered insitu by a gold layer of thickness of 20 nm deposited by RF sputtering [Fig. 3.1(a)]. The Au layer protects YBCO from oxygen loss in all nanofabrication steps and is removed only at the very end of the process before transport measurements. The YBCO/Au is first covered by a 950K molecular weight layer of PMMA and baked for 15 minutes at 120^oC on an hot plate [Fig. 3.1(b)](sections 3.6.1). Subsequently we define, by electron beam lithography at 30 keV, all YBCO nanostructures and the wiring to the pads. After developing the PMMA [Fig. 3.1(c)], a 30 nm thick Ti film is then deposited by thermal evaporation [Fig. 3.1(d)](section 3.7). Ti is ideal as a mask, because of its robustness. We can remove up to 200 nm of the YBCO thin film (with the parameters specified below) without substantially affecting the Ti layer. This turns as an important advantage to scale the process to thicker YBCO films, films with different epitaxial orientation and with higher intrinsic surface roughness. After the lift-off step in acetone the mask is defined [Fig. 3.1(e)](sections 3.6, 3.6.1). In order to define bonding pads we use optical lithography. As consequence we use an additional step of thermal evapora-

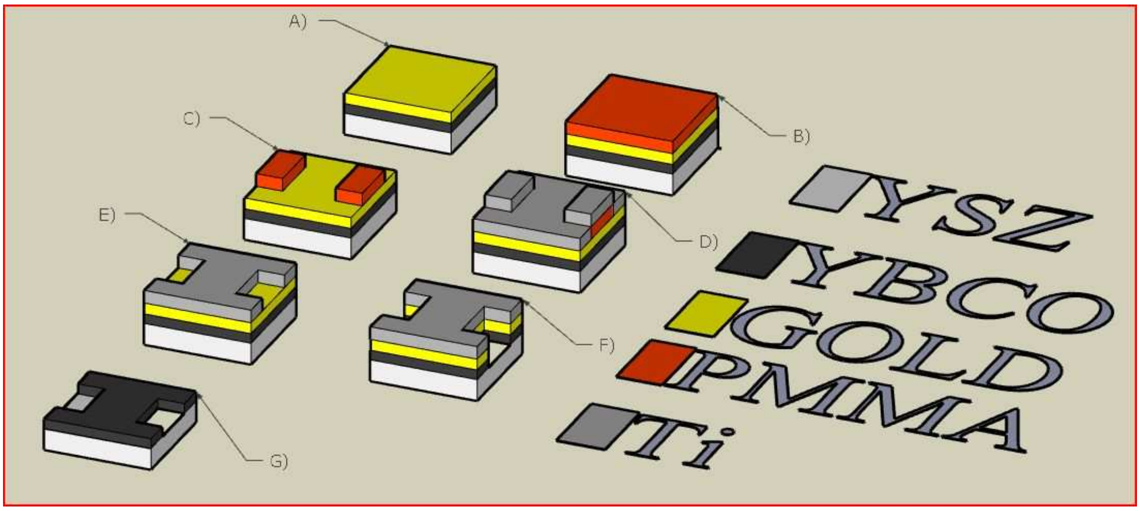

Figure 3.1: Description step by step of the YBCO sub micron structures. a) The c-axis YBCO thin film(50 nm) is deposited on YSZ and covered by a gold cup layer 20 nm thick. b) The electro resist is spun on the top of gold and the sample baked. c) Electron beam lithography and develop. d) A thin film of titanium (30 nm) is deposited. e) The titanium mask is prepared by means of lift-off. f) The hard mask is transferred on the YBCO film through cold(-140^oC) ion milling. e) The Ti mask is removed with a diluted solution of HF and the gold layer is etched away through another cold ion milling process.

tion of Au/Ti (30nm/150nm) and again lift-off. The entire mask, from large bonding pads to small nanometer size nanostructures, is then transferred to the YBCO by Ion Beam Etching at 350 eV [Fig. 3.1(f)](section 3.9). During this process the sample is kept at a temperature of -140^oC in order to reduce oxygen loss due to argon ion milling. The removal of Ti mask is then performed by a dip in 1/50 diluted HF solution for a few seconds). The very last step of the removal of Au protection layer, mentioned before, is made by a soft ion milling keeping again the sample cold at -140^oC [Fig.3.1(g)](section 3.10. The smallest feature width we could obtain with this process is 60 nm see figure3.2. The typical edge damage in our devices is estimated of the order of 20 nm.

In figures 3.2, 3.3 and 3.4 are presented some SEM images of the nanostructures patterned by employing the titanium mask technique. Both the size and quality of samples make our nanostructures very competitive when compared with [33],[5],[12]. The nanoring produced are unique in YBCO literature and in general they are among the smallest loops ever fabricated [3], [19], [25].

To better understand the advantages of Ti masking is useful to mention the C masking [33],[11], that is the most used technique to pattern YBCO films. Basically the process is similar to the one described above but the carbon mask technology requires additional steps [33]. The C mask is not patterned through lift off but through reactive ion etching. On the top of the Au cup layer are deposited the carbon film and an additional metal layer respectively. The metal film is just necessary to allow to the resist to adhere on the top. After the resist is processed by e-beam and developed. The patterned resist is transferred to the carbon mask through reactive ion etching. After the YBCO film is ion milled as for the Ti technique.

Our process is safer than the one based on C because the additional ion etching of the mask is not required.

3.2 Film deposition via Magnetron Sputtering

The thin YBCO films have been deposited through sputtering technique. The sputtering facility used for the fabrication is located at the superconductivity labs at the Engineering Faculty of University Federico II of Naples. In a typical sputtering system, the material to be deposited is in the form of a pellet called target. It is connected to the negative terminal of a dc or RF power supply, therefore represents the cathode of the system. The substrate that faces the cathode is usually grounded, and placed on a heater. After that a good level of vacuum is ensured in the chamber($\sim 10^{-7} mbar$), the process gas, typically argon, is introduced and serves as the medium in which a discharge is initiated and sustained. Microscopically, positive ions in the discharge strike the cathode plate and eject neutral target atoms through

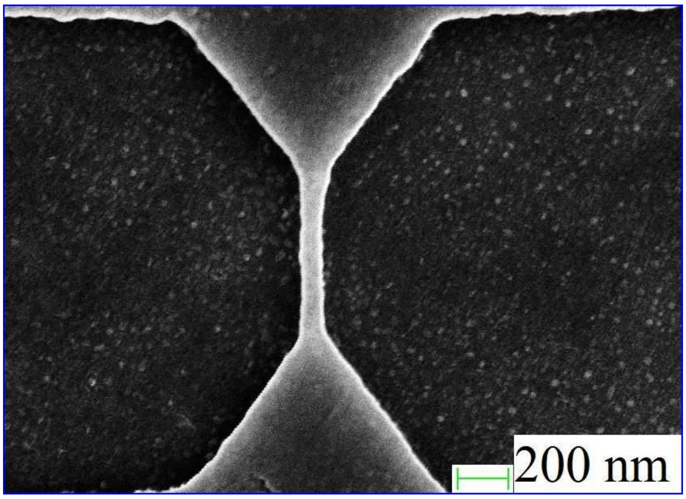

Figure 3.2: SEM images of a YBCO nanobridge 60 nm wide.

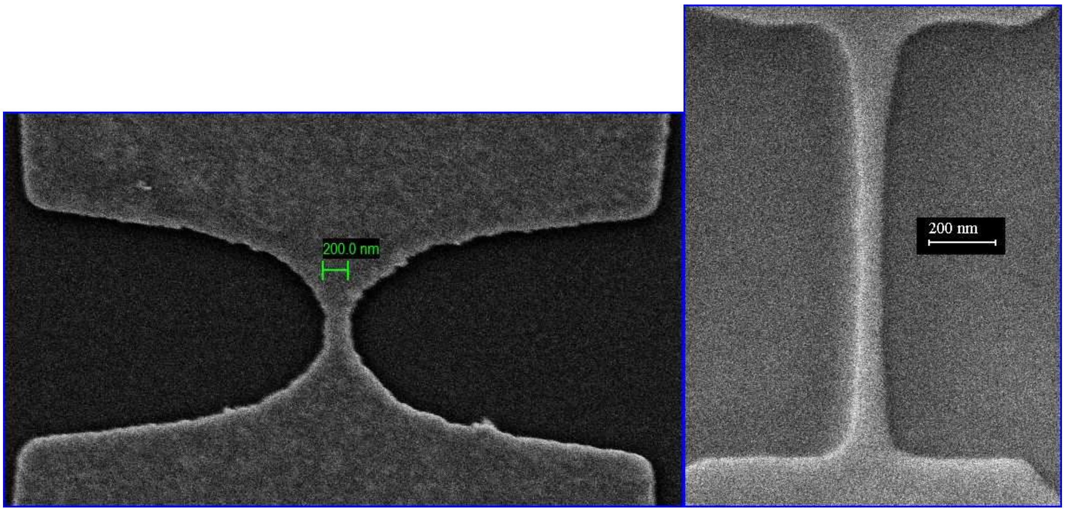

Figure 3.3: SEM images of two YBCO nanobridges. On the left the nanobridge is 200 nm wide and 300 nm long; on the right the nanobridge is 200 nm wide and 1 μm long.

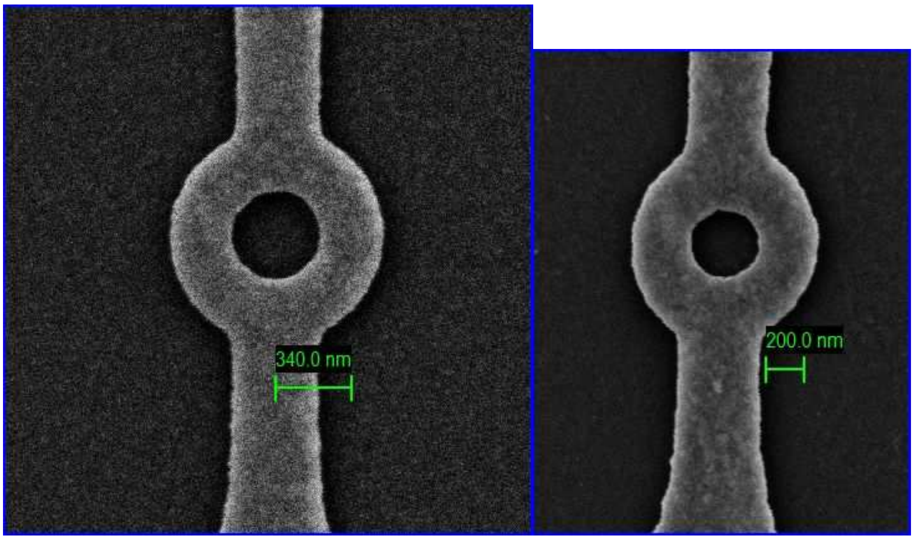

Figure 3.4: SEM images of two sub micron rings. On the left a nanoring with an average radius of 340 nm and with an arm 300 nm wide is reported. On the right the ring has an average radius of 300 nm and an arm 200 nm wide.

momentum transfer. These atoms enter and pass through the discharge region to eventually deposit on the growing film. The manner in which a glow discharge progresses in a low-pressure gas using a high impedance dc power supply is the following. A very small current flows at first due to the small number of initial charge carriers in the system. As the voltage is increased, sufficient energy is given to the charged particles to create more carriers. This occurs through ion collisions with the cathode, which release secondary electrons, and by impact ionization of neutral gas atoms. With charge multiplication, the current increases rapidly, but the voltage, limited by the output impedance of the power supply, remains constant. Large numbers of electrons and ions are created. Eventually, when the electrons generated produce sufficient ions to regenerate the same number of initial electrons, the discharge becomes self-sustaining. The gas begins to glow now, and the voltage drops, accompanied by a sharp rise in current, which signals the occurrence of "normal glow". A further increase in power results in higher voltage and current density levels. The "abnormal discharge" regime has now been entered, and this is the operative domain for sputtering and other discharge processes (e.g., plasma etching of thin films). The addition of a magnetic field to the plasma dynamic is used to enhance the sputtering yield. When a magnetic field is superimposed on the electric field between the target and substrate, electrons experience the Lorentz force in addition to electric field force and their trajectory becomes spiral-like. Therefore, magnetic fields prolong the electron residence time in the plasma and thus enhance the probability of ion collisions. This leads to larger discharge currents and increased sputter deposition rates. In magnetrons, electrons ideally do not even reach the anode but are trapped near the target, enhancing the ionizing efficiency there. This is accomplished by employing a magnetic field oriented parallel to the target and perpendicular to the electric field. Therefore, the magnetic field lines first emanate normal to the target, then bend with a component parallel to the target surface and finally return, completing the magnetic circuit (Figure 3.5). Electrons emitted from the cathode are initially accelerated toward the anode, executing a helical motion in the process; but when they encounter the region of the parallel magnetic field, they are bent in an orbit back to the target. By suitable orientation of target magnets, a "race track" can be defined where the electrons hop around at high speed. Target erosion by sputtering occurs within this track because ionization of the working gas is more intense above it.

It is important to stress the necessity to use a conductive target to promote a self sustained discharge in dc mode and a subsequent deposition yield. In fact when the target is insulating, the generation of charges in the glow is stimulated imposing an ac electric field between the sputtering electrodes. This makes it possible to sputter any material irrespective of its resistivity. Usually the oscillation frequency of the field is 50 kHz. The previous procedure is called *RF Magnetron Sputtering.* This type of sputtering presents also more difficulties to the deposition with respect to the dc magnetron sputtering because the ac field could induce a back sputtering, where the ions start to collide with the substrate and a certain careful is needed trying to prevent it. The fabrication process adopted for the YBCO sub micron structures has involved the ac magnetron sputtering to deposit the gold cup layer on the YBCO.

3.3 Thin Film deposition via inverted Dc Magnetron Sputtering

The right amount of oxygen is a crucial ingredient to have optimal doping and superconductivity in YBCO with high critical temperature. Therefore, the deposition of YBCO films takes place in a mixed atmosphere of oxygen and argon. In a standard planar magnetron configuration, the oxygen atoms would generate negative ions; they would be accelerated towards the substrate causing, in turn, the bombardment of the film which has just been deposited. One of the possible configurations to avoid this problem is the cylindrical configuration [5]. The target has the shape of a hollow cylinder, with the magnets placed along its internal or external surface. The external configuration is called inverted cylindrical magnetron (ICM) and is used since many years for the realization of high quality YBCO films [5]. The

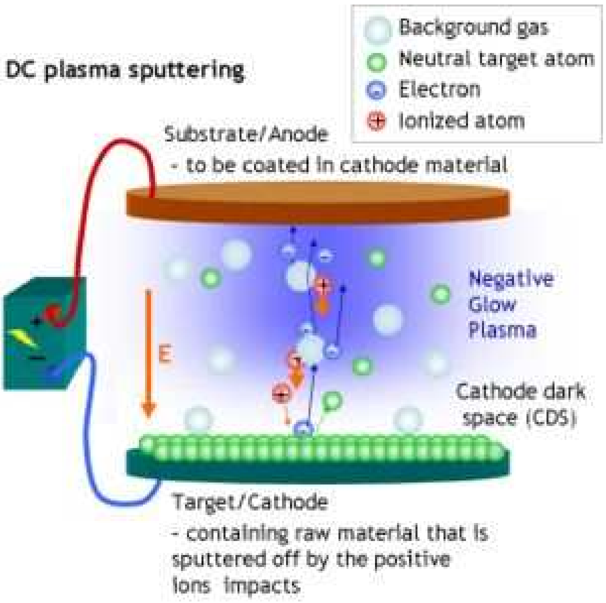

Figure 3.5: Sketch of a dc sputtering deposition system.

magnetic field lines are radially oriented with respect to the target surface, keeping the ions inside the target surface and preventing them from reaching the substrate where the deposition is taking place.

3.4 The epitaxial growth

The control of the YBCO crystallographic orientation is a fundamental issue to have high quality films. The desired epitaxy is promoted by a suitable choice of the substrate(crystal). Two types of epitaxy can be distinguished: the *homoepitaxy* regards the case where the film and the substrate are com-

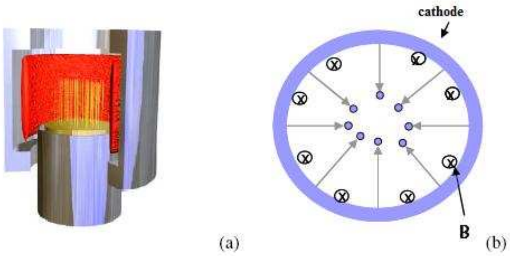

Figure 3.6: Two different perspectives of a cylindrical magnetron sputtering

posed by the same material, whereas *heteroepitaxy* deals with the film growth on a different material. The latter case is more common. In heteroepitaxy it is more common that the two elementary cells, the target one and the substrate one are different and occur always a mismatch between the two lattices. Therefore the defects in the film are inevitable. It is possible to catalogue the defects in four classes[6]:

1. Propagation of defects from the substrate into the epitaxial layer. This source of defects is certainly the most frequently cause of defects in homoepitaxial film deposition.
2. Stacking faults.
   Stacking faults are crystallographic defects in which the proper order of stacking planes in crystal lattice of the deposited material is interrupted. It is caused by an improper substrate preparation.
3. Formation of precipitates or dislocation loops due to supersaturation of impurities. These defects occur in the solid after growth due to intentional or accidental doping.
4. Formation of low-angle grain boundaries and twins due to rotation of islands. The defect is caused by a mismatch between the lattice parameter of the substrate and the epitaxial layer one, there is some ambiguity in the exact orientation of small nuclei.
5. Formation of dislocations due to the lattice parameter mismatch between substrate and epitaxial layer.

3.5 The YBCO deposition procedure and the gold protection

The YBCO thin film deposition is accomplished by cylindrical sputtering and by optimizing several parameters of the deposition process. The c-axis YBCO thin films have been grown on strontium titanate ($SrTi0_3$[100])(STO) substrates. First the STO substrate, is placed on a ceramic heater located inside the deposition chamber. During all the deposition steps the sample temperature is monitored by a thermocouple nested in the ceramic heater. A P.I.D. program controls both the temperatures and the ramps (time derivatives) among the different stages of the process with an accuracy of the 0.1%. The chamber pressure is lowered down to $2\,10^{-6}$ mbar, while the substrate is annealed at a temperature of 915^oC for 45 minutes. A mixture with a ratio 1:1 of pure oxygen and argon gas is introduced reaching an internal pressure of 0,7 mbar and the magnetron is switched on and tuned to the optimal working point of 100W. The heater is approached to the magnetron and kept at a distance of 2 mm from the magnetron and, the deposition

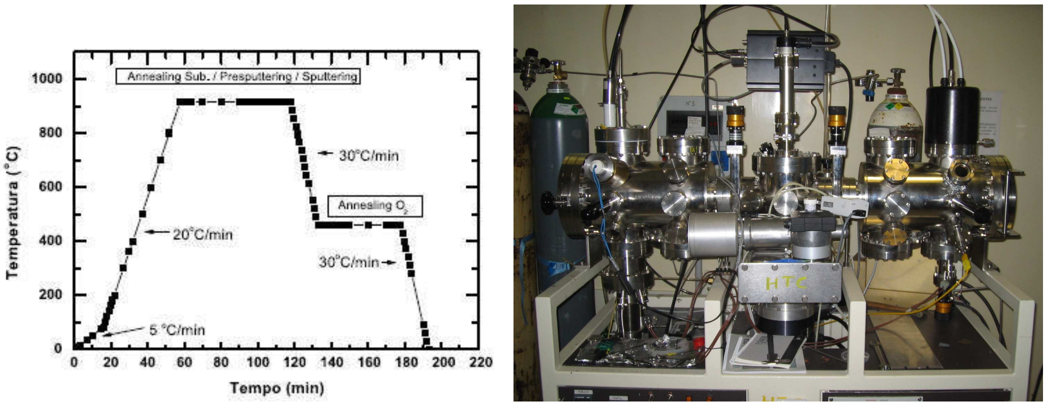

Figure 3.7: Left panel: The graph shows the duration and time variation of temperatures during the film deposition. Right panel: picture of the sputtering system.

starts. The procedure described allows a reproducible deposition rate of 3.5 nm/min. All samples fabricated are 50 nm thick, this means that the film deposition takes 15 minutes. The crucial step of the annealing in a pure oxygen atmosphere takes place at a temperature of 460^{o}C for 45 minutes in oxygen at a pressure of 800 mbar. The temperature is decreased at a rate of $30^o C/min$. During the last stage the oxygen enters the film promoting the change in crystal orientation from tetragonal to orthorhombic, that is essential for the onset of superconducting properties. The procedure is finished, and the substrate temperature is brought down to room temperature. In left side of figure 3.7 we report the variation in time of the temperature of the sample which signals all the different stages of the deposition. In the right side a picture of the deposition system is reported.
All films are covered with a thin film of gold 20 nm thick. The deposited gold works as cap layer to reduce any oxygen desorption during the successive patterning. The gold is deposited on the YBCO film by RF planar sputtering in the same chamber of YBCO deposition. The sputtering power is 40 W in an argon atmosphere ($2\,10^{-3}$ mbar), the substrate is not externally heated. In these conditions the 20nm thick gold layer is deposited in 1.5 minutes.

3.6 Patterning YBCO sub micron structures through lift off technique

The YBCO films are typically 50 nm thick and have been patterned using electron beam lithography, standard photolithography and ion milling respectively. The aim of the two lithographic procedures is "moulding" a titanium mask on the top of the gold layer. The hard mask reproduces the shape of all the samples, from bonding pads to nanostructures. The ion milling etching allows to transfer the titanium mask to the YBCO film. In the next sections all the patterning steps are commented in detail.

3.6.1 The electron beam lithography(EBL)

The EBL is a powerful technique for fabricating circuits/devices at nanoscale. Nowadays the EBL systems are capable to reach a width line on the order of 10 nm or less. In the next sections the efficiency of a processing does not depend only on the reliability of the e-beam lithography but concerns all the fabrication stages.

The electron beam (e-beam) lithography(EBL) refers to a technique employing a collimated beam of electrons for exciting selectively a polymeric film called *resist*. The operation allows to remove specific areas of resist covering, in this case, the gold layer. More precisely the resist areas irradiated by electrons undergo chemical-physical changes that involve the modification the bonds among the polymers of resist. Since positive resist is used in the process the irradiated areas become soluble in an appropriate solvent called *developer*.

The e-beam lithography system used for fabricating sub-micron structures studied in this PhD work is a "Scanning Electron Microscope"(SEM) (brand "ZEISS" model "GEMINI") converted into an electron beam lithography facility.

The procedure consists of the following passages.

First a viscous solution, the resist (Poly methyl methacrylate or PMMA), is laid on the gold via a *spin-coater*. The operation is accomplished by rotating at 6000turns/min the sample covered with an excess amount of resist. Hence the spun resist is baked on a hot plate at 120^oC for 15 minutes. After baking the resist layer is roughly 200 nm thick. Than the sample is ready to be processed by the electron beam.

The sample is placed on a suitable support inside a chamber where the pressure is reduced down to the order of 2 10^{-3} mbar. The electrons of the beam are generated by thermionic emission induced by Joule heating in a tungsten filament that is constantly at a pressure of 10^{-10} mbar. The emitted electrons are accelerated by a voltage of 30 kVolts and collimated by opportune accelerating plates and electromagnetic lenses (see figure 3.8). The electron beam is controlled by a software that follows the instructions of a "CAD" with which have been drawn the sub micron structures to be patterned. In figure 3.9 the CAD image of a sub micron ring is shown. After the exposure, that roughly takes 1 hour, the sample is rinsed in a developer for 2 minutes. The developer used for this process is the methyl isobutyl ketone (MIBK). Since the developer is very aggressive against the PMMA, after the 2 minutes the chemical attack of MIBK is quenched diving the sample in the

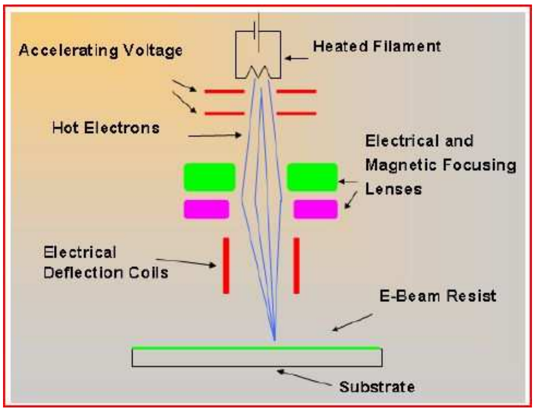

Figure 3.8: Schematic representation of an electron beam lithography system.

isopropanol for 30 seconds.
The efficiency of the process might be invalidated by spurious charge accumulation on the sample, that can induce an unwilling deflection of e-beam. The most incisive source of charge accumulation is due to the insulating nature of the substrate. The problem is circumvented grounding the sample. The operation is accomplished by applying some silver paste between the gold layer and the sample support. After the exposure, that roughly takes 1 hour, the sample is rinsed in a developer for 2 minutes. The developer used for this process is the methyl isobutyl ketone (MIBK). Since the developer is very aggressive against the PMMA, after the 2 minutes the chemical attack of MIBK is quenched diving the sample in the isopropanol for 30 seconds.

3.7 The titanium deposition

After the development the sample presents a patterned resist in shape of negative mould of nanostructures. Hence a thin titanium layer 30 nm thick is evaporated over the sample. The operation is performed in a vacuum chamber at a pressure of 10^{-6} mbar. The hard metal is vaporized by the injection of an high current that causes the diffusion and the deposition of the metal everywhere on the substrate. The deposition rate is measured via a *quartz crystal thickness monitor* or QTM. This device is constitutes by an oriented crystal of quartz that works as a resonator when it is inserted in an appropriate circuit. The oscillation frequency depends on the thickness of material deposited over it. The big advantage of this technique is that the QTM can measure in time the thickness of Ti deposited. When the right amount of Ti has been evaporated on the film a shutter closes the interconnection between the sample and the titanium melting pot. The titanium

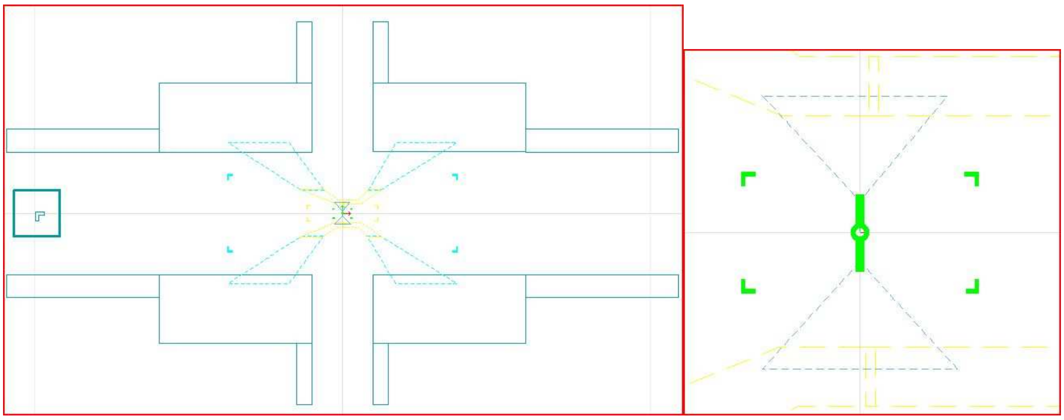

Figure 3.9: Left: CAD image for EBL procedure. In the image are also present the markers(in shape of "L") for the alignment with the chromium mask for patterning the bonding pads by photolithography. Right: zoom of the Left image on the sub micron ring.

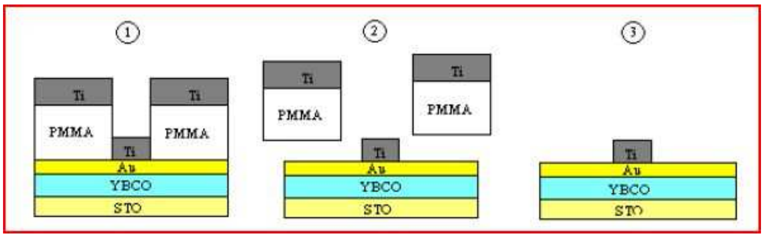

Figure 3.10: The three steps describes how the lift off works. The step 1) represents the sample after the titanium deposition. In 2) the sample is immersed in acetone that removes the resist. 3) On the sample remains only the titanium mask.

deposition rate when in the chamber is obtained a pressure of $2.9\,10^{-6}$ mbar is 9 Å/sec.
Once the titanium is deposited, the next step is the *lift-off*. This procedure concerns the selective removal of titanium by washing the sample in acetone, that is a solvent for the resist. The lift off process is depicted in figure 3.10. In order to obtain a good lift off the thickness/height of the resist has to be considerably larger than the resist one. Furthermore the removal of the resist can be faster if one uses hot acetone or an ultrasonic washer.

3.8 Photolithography and deposition of contact leads

In principle the EBL along with the ion etching could be sufficient for patterning all the nanostructures on the YBCO film. Nevertheless, since the bonding pads of each sample have micrometric dimensions it is faster to pattern the Ti mask of pads with standard photolithography.

The concepts of patterning procedure by using the photolithography are very similar to the EBL. A photoresist layer is spun on the film surface by using the same speed parameters of the PMMA. The photoresist used is the S1818 that is more viscous than the electro-resist, that is why the measured thickness of the photoresist is 2 microns rather than of the 200 nm of the PMMA. The photoresist is baked for 15 minutes at 90^{o}C. The photolithography uses UV light to impress the resist rather than an electron beam as in EBL. After the baking the sample is ready for the UV exposition. The sample is accommodated below a glass mask where is present a chromium layer patterned in the same shape of desired micro structures. In this case, the chromium is patterned in shape of pads, which basically are squares 100 $\mu m\times$ 100 μm. The following step is the alignment of micrometer pads with the nanometric structure. The alignment is favored by some markers patterned on the sample during the EBL process and are also present on the chromium mask either(see figure 3.9). The alignment is made by moving suitably the chromium mask acting on micrometer screws. After the alignment, the mask is pressed against the baked photoresist and the ultraviolet light is turned on. The irradiation takes just 20 seconds. In order to improve the definition line, after the exposition the resist is baked again at 120^{o}C for 20 seconds. The development stage of the resist is performed dipping the sample into MF319 for 20 seconds whereas the developer attack is blocked in deionized water. At this stage uncovered regions of resist in shape of electric pads are present on the sample. The real leads of nanostructures are achieved first evaporating chromium and subsequently gold. The chromium layer works as glue between the gold cup layer and the second gold deposition. The chromium layer 10 nm thick while the gold is about 80 nm thick. Note that the second gold deposition is on purpose much thicker than the Au deposited on the YBCO film cup layer, and the reason will be clearer in the next section. The metal evaporation stage ends with the deposition of a titanium layer 100 nm thick. The subsequent *lift off* removes the titanium from the undesired parts of the sample. The titanium mask is complete. Now it has to be transferred to the YBCO layer.

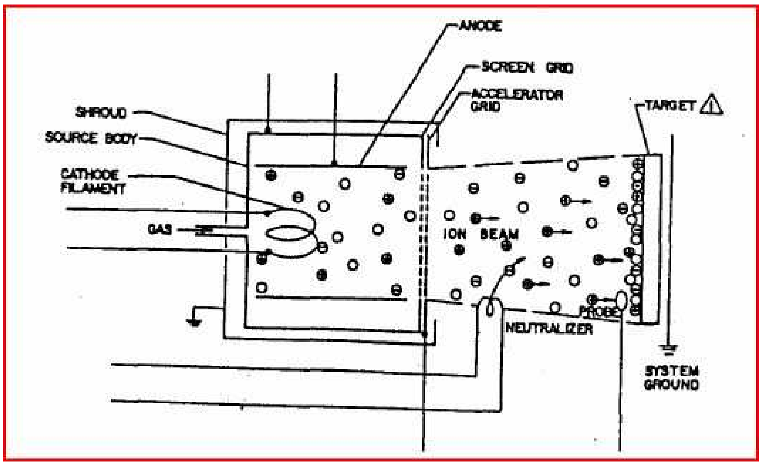

Figure 3.11: Sketch of the ion milling facility.

3.9 The ion milling

3.9.1 Basic concepts

The profile of each structure is obtained submitting the sample to the action of a directional ion bombardment. The procedure is accomplished by using an ion milling system. This facility is at the Engineering Faculty of University Federico II of Naples. The system uses argon ions as bullets to dig the sample spaces which are not protected by the titanium layer. The main components of an ion gun are reported in figure 3.11.

The ion etching basically works as a sputtering system, although in this case the target of argon ions is the sample. Inside the vacuum chamber a tungsten filament, acting as a cathode, is heated using a voltage V_f. The electrons emitted from the cathode by means of thermionic effect are accelerated toward the anode. On the way, they impact the argon atoms introduced in the chamber and ionize them. A grid held at a voltage V_g accelerates the ejected ions toward the target where they will hit the sample and remove the material not protected by the mask. Ions arrive at the target surface with an energy given by

$$E_{ion} = q\,|V_p - V_q| = q\,|V_a + V_{pa} - V_g| \tag{3.1}$$

where V_p is the plasma voltage with respect to ground, V_a the difference between V_f and the anode potential and V_{pa} the plasma voltage with respect to the anode. The latter quantity is only a few volts because of the large anode area (all he chamber acts as anode). Therefore, extracted ion energy is controlled by changing V_a and V_g.
In the system other parameters can be tuned as the argon pressure in the

chamber and the tilt of the sample holder with respect the beam direction.

3.9.2 Cold ion milling and used optimized parameters

The sample is attached with silver paste on the support that is kept perpendicular to the ion beam. Then the pressure inside the chamber is lowered down to 10^{-6} Torr. Since the heating generated by the impact of ions with the sample inevitably induce oxygen desorption, the etching begins only after the sample is cooled down to $-140^{o}C$. The cooling is performed feeding the sample support with cold nitrogen gas. Outside the facility the tube is in shape of solenoid and is inserted in a dewar containing liquid nitrogen. The temperature of the sample is monitored via a thermocouple inserted into the sample support. When the sample has reached the desired temperature, some argon gas is entered the chamber until the pressure is 10^{-4} Torr. Now the ion milling can start. In order to further decrease any damage the treatment duration is divided in several runs. Typically each minute of etching is followed by a minute of rest and so on. The etching rate and the mean parameters of the procedure are listed in the table 3.9.2. The sample holder has been always kept perpendicular to the ion gun.

cathode filament current	2.59 A
discharge current	0.07 A
beam current	5 mA
discharge voltage	55.0 V
beam voltage	315 V
neutralization emission current	6 mA
filament current	2.21 A
etching temperature	-140^{o}C
YBCO etching rate (nm/min)	2.5
Au etching rate (nm/min)	12
Ti etching rate (nm/min)	1

3.10 Titanium mask and gold removal

The etching process has finally transferred the titanium mask to the YBCO film. The metallic Ti hard mask is stripped out diving the sample in a diluted solution(20%) of Hydrofluoric acid(HF). The sample is first immersed for 12 seconds in the HF solution and subsequently the acid attack is blocked in deionized water.

Therefore the gold layer 20 nm thick is removed again by cold ion etching following the treatment discussed above. The whole fabrication process is finished. Now the sample presents between 40 and 50 sub micron structures available for four probes measurement. A gold 30 nm thick layer covers only

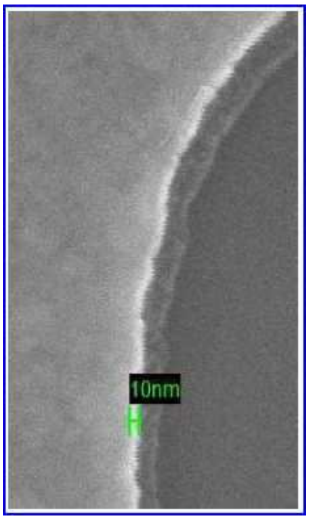

Figure 3.12: SEM image representing the edge of a sub micron bridge. The lateral damage(identified by the brighter region) is roughly 10 nm.

the bonding pads for improving the ultrasonic bonding of aluminium wires and reducing their contact resistance as well.

3.11 Final comments and outlook

The two main causes which can seriously degrade the YBCO quality are heating[7], [8] and water([9] and reference therein). As discussed before they both favor oxygen desorption and as consequence depress the superconducting properties of the compound. The heating deriving from the ion etching is quite reduced by cooling the sample. Instead the sample goes in contact with water mainly when is dipped in the HF solution that is composed of the 85% of water.
A reactive ion etching (RIE) process could be a promising alternative to the HF solution. Basically the RIE uses a chemically reactive plasma to remove selected materials on the sample. Aiming to remove only the titanium layer, first attempts have been executed by injecting in the vacuum chamber $SF6$. First results are promising but the process has still to be optimized. Fortunately the gold cup layer protects fairly well the YBCO and the sub micron structures are mainly damaged at the edge. A rough estimation of the *dead layer* has been achieved by SEM images. In these type of imaging the color can give some hints on the conductivity of the sample. In fig 3.12 is reported a SEM picture of a sub micron bridge edge. The borders are brighter highlighting the local insulating nature of the material.

Bibliography

[1] M. Morelle *et al.*, *Phys. Rev. B* **70**, 144528 (2004)

[2] R. P. Groff and R. D. Parks, *Phys. Rev.* **176**, 567 (1968)

[3] H. Wang *et al.*, *Phys. Rev. B* **75**, 064509 (2007)

[4] Leon I. Maissel, Reinhard Glang *Handbook of Thin Film Technology*, Mc Grow-Hill 1970

[5] Xi X.X., Geerk J., Linker G.Q., Li Q., Meyer O., *Applied Physics Letters*, 54 2367 (1989)

[6] G. B. Stringfellow, *Reports on Progress of Physics* 45, 469 (1982).

[7] J. R. Cooper *et al. Physical Review B* **44**, 12086 (1991)

[8] A. W. Hewat *et al. J. Less-Common Met.* ,**39**, 164Ű165 (1990)

[9] Ryusuke Kita & Fuhimiro Usumi *Physica C* 357-360 (2001) 792-795

[10] P. Larsson *et al. Journal of Vacuum Science Technology* B 18(1), (2000)

[11] Philippe V. Komissinski, *Applied Physics Letters* **80**, 10022 (2002)

[12] P. Mohanty *et al.. Physica C*, Physica C 408Ű410 666Ű669 (2004)

[13] Ke Xu and J.R Heath *NanoLetters* **8**, 3845 (2008).

[14] J. A. Bonetti *et al.*, *Phy. Rev. Lett.* **93** 087002 (2004)

Chapter 4

Low temperature measurements and technique

Transport measurements of YBCO nanostructures have been carried in labs of university of Naples "Federico II". The measurements displayed in this Ph.D. thesis have been acquired by employing a custom He3 cryostat capable to reach 0.3 K as base temperature. This section is dedicated to the measurement equipments and strategies adopted to perform low noise measurements.

4.1 He3 cryostat

The easiest procedure to perform low temperature transport measurements concerns the direct immersion of a suitable measuring probe into liquid nitrogen or helium. Lower temperatures can be reached by employing a series of commercially refrigerators that exploit the cooling He3 or of a mixture of He3/He4(dilution refrigerator). The He3 refrigerator reaches a base temperature of about 0.3 K while the dilution refrigerator can achieve a temperature of 20 mK or even lower. Essentially these refrigerators achieve the base temperature by pumping out the vapors of the liquified He3 or He3/He4 respectively. In what follows we focus on the He3 cryostat(Heliox).

3He refrigerators run by condensing a small amount of 3He and then pumping on it to reduce its vapor pressure. The decrease of the 3He vapor pressure down to about 10^{-3} mbar brings a decrease in temperature, down to 0.3K, as it can be seen form the vapor pressure versus temperature graph in Figure 4.1. The pumping power needed to reach such a pressure is provided by a sorption pump. They rely on the dispersion forces existing between a gas and a surface to bind gas molecules on chilled surfaces inside the pump (cryosorption). In 3He refrigerators they consist of a cylindrical body filled with zeolite, a highly porous material with a surface to volume ratio of about 800 square meters per cubic centimeter. Zeolite particles are, in fact, characterized by molecular sized cavities linked by pores of a few angstrom of diameter that can trap gas molecules, in this case helium. The number of gas molecules that can be held on a given zeolite surface depends on the temperature. Practically, a sorb in a 3He refrigerator is designed so that at ∼10 K almost all of the 3He is adsorbed, whereas at ∼30K all the molecules desorb.

Figure 4.2 shows a sketch of a typical 3He system and its main working parts. The sample is mounted on the 3He pot at the bottom of the system, in a sample holder providing the electrical connections. The inset is closed with a brass shield and vacuum is realized inside the inner vacuum chamber (IVC) to provide isolation from the main liquid helium bath. The cooling to the base temperature of 0.3K takes place in three phases. The first step regards the cooling from 300K down to 4.2K. This step of the cooling procedure is carried out by immersion in a liquid helium bath. The thermalization of the system is assured by a small amount of exchange helium gas previously inserted in the IVC.

The second stage of procedure cools the sample from 4.2K to 1.3K, and exploits the liquefaction of the He3 that happens below 2K. This temperature is achieved by pumping on liquid 4He extracted by the bath and contained in the 1K pot. From Figure 4.1 it is possible to see that to reach temperatures of about 1.3K a 4He vapour pressure of approximately 1 mbar is needed. The 1K pot is therefore connected to a rotary pump and the pumping power is regulated via a needle valve. During this phase of the cooling process the sorb is heated and kept at 35K. At this temperature, it will not absorb any 3He, therefore this can flow from the reservoir to the 1K pot, where it will condense, and then run down to cool the sample and the liquid 3He pot [4.2,a)]. The system is kept in this condition for about 20 minutes to allow all the 3He gas to condense.

The third stage of cooling allows to reach the base temperature of about 0.3K. Once the 3He pot is full of liquid 3He at approximately 1.3K, the sorb heater is now switched off for allowing the sorb to cool down. It will begin to reduce the vapor pressure above the liquid 3He so the sample temperature drops [4.2,b)]. As the limiting pressure is approached, the temperature of the liquid 3He can be reduced to below 0.3K.

4.2 Upgrades to system and measurement techniques

The He3 insert the measurement dewar and especially all the electrical wiring has been customized to improve the signal-noise ratio. We have used three different materials for the wiring: manganin, copper and a Nb-Ti. This choice reflects a strategy, because there are two important laws to obey for perform high quality measurements. Firstly the wiring has to have a low heat load, otherwise the base temperature can be invalidated or limited in time. Secondly it has to have a low thermal conductivity for both reducing the electrical noise due to any temperature gradient and of course to reduce as much as possible the thermal link with the room temperature. In order to accomplish these requirements we have selected the material of wiring accordingly to the three stages of temperature of the insert which are, 300K-4.2K, 4.2K-1K, 1K-0.3K. In the first two temperature stages we used manganin wires, which have low thermal conductivity, for all the lines apart the current ones. We used copper wires to carry the current to samples because of their low resistivity compared with the manganin one. All wires were twisted paired to reduce inductive coupling with the environment and inserted into german silver capillars, which have low thermal conductivity, for screening measurement signals against external electromagnetic irradiations [1]. Capillars were thermal anchored to each temperature stage. From the 1K pot to the 3He pot, instead, niobium-titanium superconducting wires have been used. The critical temperature of this alloy is 11K. The superconducting wiring is a very important improvement for this system. Thanks to it, we are able to bias the samples with higher currents without excessive heating.

The refrigerator was also equipped with a solenoid for the generation of magnetic field, which has been handmade. A superconducting Nb - Ti wire was used for the windings in order to generate magnetic fields with negligible heating. The superconducting wire is wrapped around a copper cylinder that is cooled by the 1K pot through a copper thermal link. We can provide 300 milliTesla to the sample up to 70 K.

The sample is mounted on a handmade sample holder made in copper. This is made in copper and has a cylindrical symmetry (fig...) the sample is placed inside a printed circuit board on which have been patterned the contact pads by hand. The sample is electrical connected to copper pads with aluminum wires which are stuck with an ultrasonic bonder. In turn the copper pads are electrically connected to a male Fisher connector that stretches out of the sample holder and works as electrical link between the sample and the wiring in the insert. Close to the sample is placed a diode thermometer. The sample holder is thermal connected to the He3 pot via a copper cold finger in which is also placed a female Fisher connector.

4.2.1 Cold filters and magnetic shields

The voltage measurements of samples require inevitably the use of filters. This necessity is due to very small voltages measured which are, at most of the order of hundreds of microvolt. The choice of the temperature stages positioning along with the bandwidths of filters rely on a precise strategy. The filters bandwidth are chosen to decrease inversely to the temperature stage. This protocol trivially derives from the conversion of temperature in frequency $k_B T = h\nu$ that yields $\sim 21GHz$ at 1 K and $\sim 6Gz$ at 0.3K. Our wiring is fitted with three stages of filters all handmade. The first two stages which are thermal anchored to the He3 pot are copper powder filters. These filters cut the frequencies in the GHz band. One stage is directly inserted in the cold finger, the second is coupled to the top of the He3 pot. The copper powder filters have been fabricated following the prescription of ref. [2]. The other stage is composed by RC filters which are anchored to the 1K pot(see fig. 4.3). These filters have at 300 K a cutoff frequency of 100MHz. The best way to estimate the quality of filtering consists into comparing the critical current of a superconducting sample before and soon after the filters installation. In fig 4.4is shown the improvement of the critical current of a biepitaxial Josephson junction followed to the insertion of filters in the measurement wiring. The noise has been reduced so carefully that the critical current has been improved of about the 35%.

The magnetic field couples with superconducting samples and can affect the transport measurements. In order to decouple the sample by any spurious magnetic field the measurement dewar has been equipped with a magnetic shield composed by a trilayer of cryoperm, lead and niobium foils. The magnetic shield is in shape of a cylinder and fitted to the bottom of the dewar to properly involve the insert at the height of the sample.

4.2.2 Scheme of instruments for 4-probe measurements

The setup for transport measurement is sketched in figure 4.5. We usually perform four probe measurements i.e. the current is injected and the voltage is acquired. The excitation current(I_0) is obtained dropping an ac voltage(triangular shape) on a shunt resistance. In order to simulate a perfect current source the shunt resistance is chosen to be much higher with respect the normal resistance of the sample. The frequency of I_0 is very small, at most 11 Hz, to reduce any cutoff effect due to the filters inserted into the wiring but also to avoid any deformation of the output signal which could result from parasitic capacity of the sample.

The voltage is acquired by a differential operational amplifier positioned at room temperature, and its principal role is decoupling the voltage(output) of the sample by the injected current(input). The operational amplifier itself is an integrate circuit but its working circuit along with the filtering from the electromagnetic environment is handmade. Hence the excitation and voltage curves are read by an oscilloscope. In order to clean further the signals by the noise the voltage and the current are averaged and finally stored in a pc. When we perform the measurement of the a voltage state at fixed excitation current we usually use a lock-in amplifier. In this measurement, for the reasons written above, a maximum frequency of 11Hz is adopted.

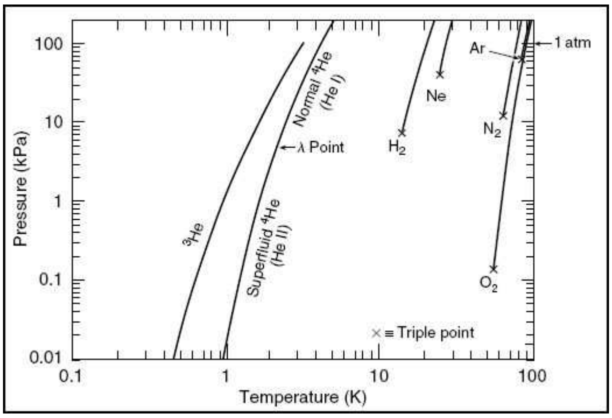

Figure 4.1: Vapor pressure of He3 and He4 as function of the temperature.

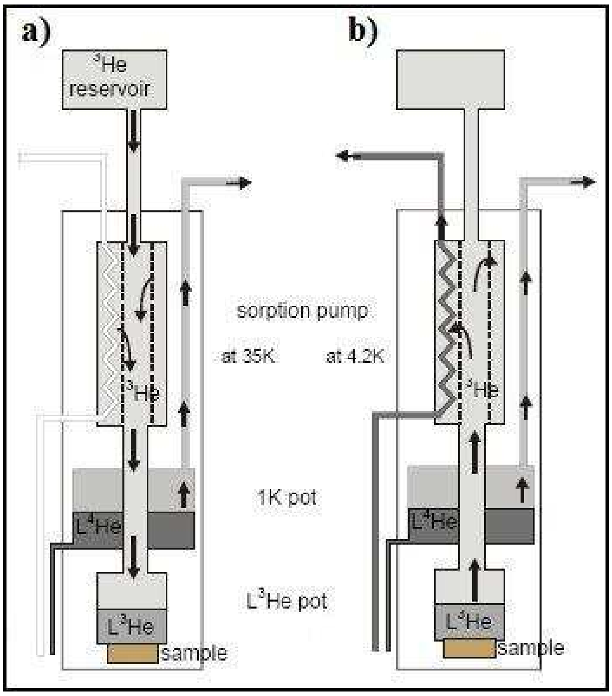

Figure 4.2: Sketch of the He3 insert and its working parts. a) He3 condensation by means of 1-K pot cooling. b) adsorption of He3 vapor through the cooling of sorption pump.

Figure 4.3: Picture of the copper case containing the RC filters.

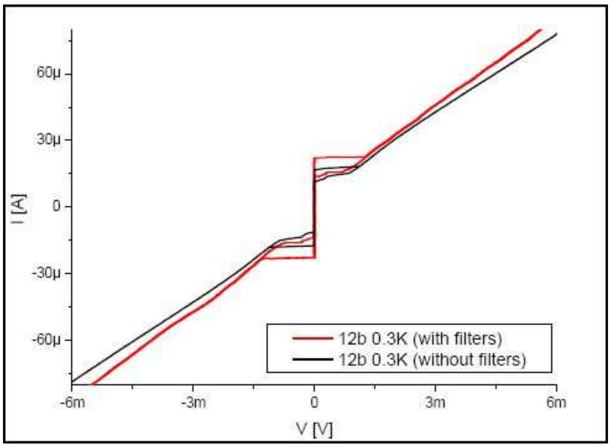

Figure 4.4: Picture of the copper case containing the RC filters.

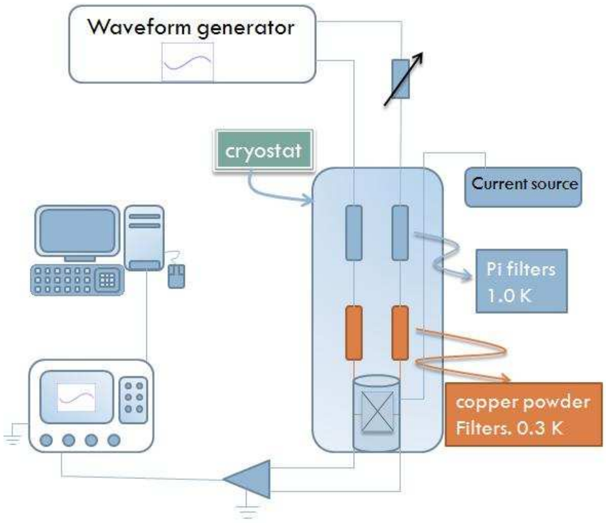

Figure 4.5: Sketch of the setup measurements.

Bibliography

[1] Zorin, A. B., *Rev. Sci. Instrum.* **66**, 4296 (1995).

[2] ZF. P. Milliken *et al.*, *Rev. Sci. Instrum.* **78**, 024701 (2007).

Part II: Experimental Measurements

Chapter 5

Resistive transitions

The first part of the chapter is dedicated to the analysis of the critical temperatures(T_C) and supercurrent densities(J_C) of YBCO nanostructures as function of channel width. The reported graphs show the high quality of samples and of the fabrication process. The analysis focuses on the shape of the resistive transitions R(T) for different widthes of the samples. After it is analyzed the effect of both the heating and the aging on the shape of R(T)'s. In the last two sections are reported the preliminary comments on two phenomena, the first one concerns the modifications on the R(T) induced by a perpendicular magnetic field and the second one focuses on the staircase shape of some resistive transitions when the zero resistance state is almost achieved.

5.1 Samples measured

The analysis of the R(T) curve is the very first way to characterize each sample. The R(T) curve is a powerful tool for investigating several aspects of the nanostructure. The analysis of the R(T)'s, based also on the geometry of the the sample, returns information both on the dissipation mechanism [1],[5] and on quality of fabrication process.

The large number of investigated samples hallow to have more reliable information on yield and reproducibility. In the tables 5.1 and 5.2 are listed the geometrical features and the critical temperatures(T_C) of the measured bridges and rings respectively. The T_C is defined as temperature at which the voltage is zero within the error of the instrument. The geometries of bridges and rings samples are sketched in figures 5.1 and 5.2 respectively. In table 5.2 ID and ED stay for "internal diameter" and "external diameter" respectively. The thickness of the samples is not reported in the tables because all the films processed were 50 nm thick.

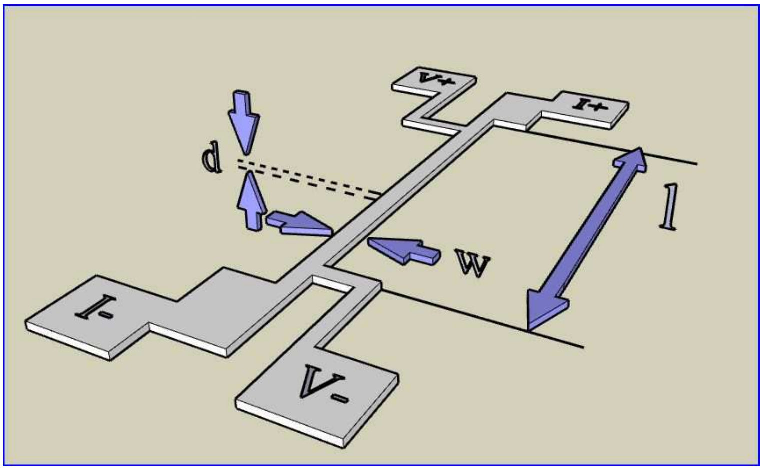

Figure 5.1: Sketch of a bridge-like sample.

bridge shaped sample	W(nm)± 5nm	L(nm)± 5nm	Tc(K) ± 0.1 K
YNB0802-dev25	300	1600	40
YNB0802-dev29	500	1800	48
YNB0802-dev32	1200	1700	48.5
YNB0802-dev37	450	1300	82
YNB0809p1-dev27	600	1000	85
YNB0809p1-dev37	450	1000	82.5
YNB0809p2-dev29	200	400	10
YNB0809p2-dev35	200	500	31
YNB0809p2-dev15	400	3000	25
YNB3R-dev29	160	1000	63
YNB3R-dev44	180	1000	28
YNB3R-dev47	550	1000	75
YNB5Dp2-0203	200	1000	71
YNB5Dp2-0207	200	1000	77.5

(5.1)

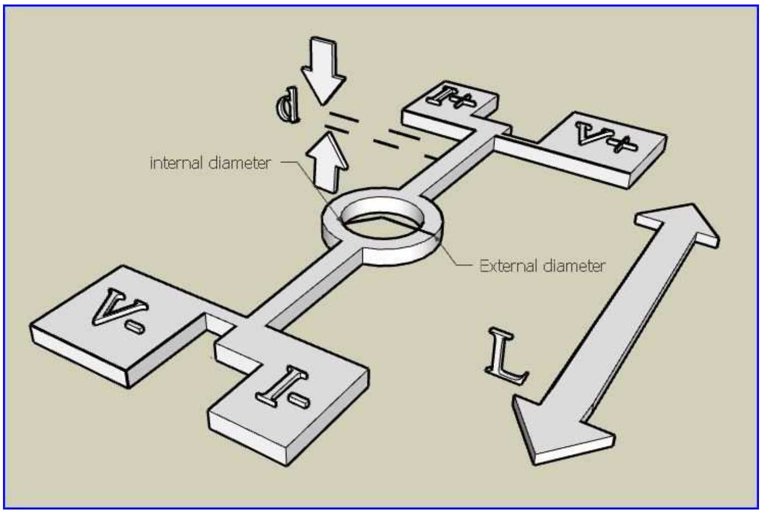

Figure 5.2: Sketch of a sample in shape of ring.

ring shaped samples	ID (nm) ± 5nm	ED(nm) ± 5nm	L(μm)± 0.1 μm	Tc(K) ±0.1 K
YNB0802-dev6	1200	1600	3	62
YNB0802-dev10	450	900	3	19
YNB0809(p1)-dev10	400	1000	3	73
YNB0809(p1)-dev41	2000	3600	3	85
YNB0809(p1)-dev24	300	800	3	79
YNB0809(p1)-dev11	400	1000	3	74
YNB0809(p1)-dev12	400	1000	3	78.5
YNB0809p2-dev17	200	750	3	57
YNB0809p2-dev16	400	950	3	76
YNB0809p2-dev13	350	1000	3	16
YNB0809p2-dev15	400	1000	3	25

(5.2)

5.2 Signature of the fabrication process improvement

Most of T_C's are collected in figure 5.3 and a discussion on the general trends introduces relevant arguments on the fabrication process. Depression of superconductivity is expected to be more relavant when the channel width is reduced. This behavior is linked to the partial oxygen desorption from the sides of the bridges which may take place on the scale on tenth of nanometers and therefore may be more relavant in nanostructures. Once the most important parameters of EBL procedure have been optimized the variations of properties of the sub micron bridges mostly depend on the details of the ion milling. Altogether the samples processing requires twice the use of the ion milling, the first one transfers the titanium mask on the YBCO film and takes 22 minutes, the second one removes the gold cup layer from the nanostructures and it is just 3 minutes long. Therefore the former ion milling affects more heavily the quality of the nanostructures and it can be considered as the main cause of samples' degradation. The ion etching heats the nanostructures and stimulates oxygen desorption. The degradation of samples is partially limited by keeping cold at about $-140^{o}C$ the sample during the milling process. Nevertheless a thermal excursion is always revealed at the end of the process.

A robust improvement of samples performances has been obtained increasing the number of steps of the ion milling procedure. The first couple of film patterned have undergone an etching divided into 11 steps of two minutes, taking one minute of rest between two consecutive ions bombardments. The temperature measured by a thermocouple changed from $-140^{o}C$ to $-110^{o}C$. Later a more careful procedure has been adopted dividing the whole etching interval in 22 steps of one minute. With this change the final temperature of the process was $-130^{o}C$, and the samples quality has been significatively improved. In figure 5.3 the critical temperatures of those samples etched by softer milling lie over the blue dashed line. The average critical temperature of samples narrower than 500 nm has been enhanced of about 15K, passing from 57K to 74K. The reduced damage of samples can be evaluated also noting the improvement of critical current densities (J_C) of samples. In figure 5.4 the J_C's are reported for different samples at 4.2 K as function of the channel width.

The performances of our nanostructures, in terms of both T_C's and J_C(4.2 K) are on the same order of magnitude with the outcomes of other nanostructures fabricated with the carbon mask technique[33]. Considering just the best results in the figures 5.3 and 5.4, the critical temperature reduces only of 7 kelvin passing from a 1μm wide sample down to a 150 nm wide one, while the J_C's remain substantially independent on the channel width.

5.3 Resistive transitions

The resistive transition(R(T)) allows to achieve two important information on the quality of a sample. The R(T) defines the critical temperature of a nanostructure and in addition the width of the transition documents the sample homogeneity. We measure the resistance by a lock-in amplifier. Furthermore to avoid any heating effect we feed the samples with an excitation current I_0 much smaller the heating one $I_h = k_B Tc/\Phi_0$ [9]. Typically we used 100nA as excitation current. In figure 5.5 are reported four resistive transi-

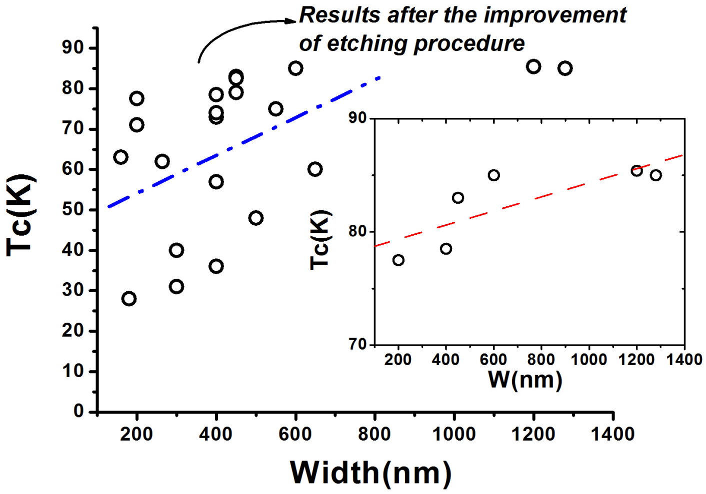

Figure 5.3: Critical temperatures as function of the width. The blue line identify, substantially, the Tc' of samples which have been etched with the softer procedure (see the text for a wider explanation). Inset: Zoom on the best results varying the channel width.

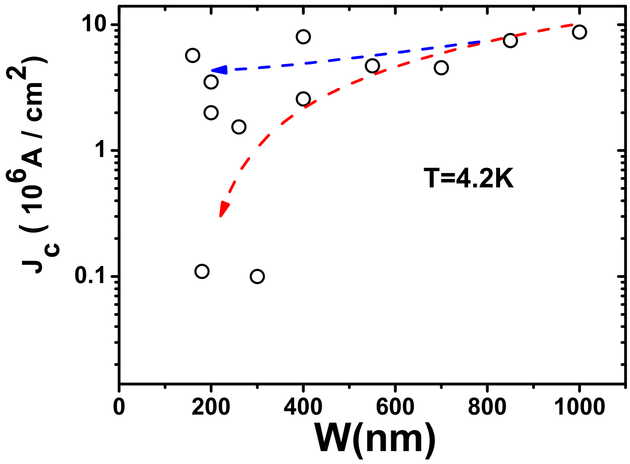

Figure 5.4: Critical current densities as function of the width. The red arrow traces the trend of the first generation of bridges. before the ion etching optimization. The blue arrow points out the trend of more recent outcomes.

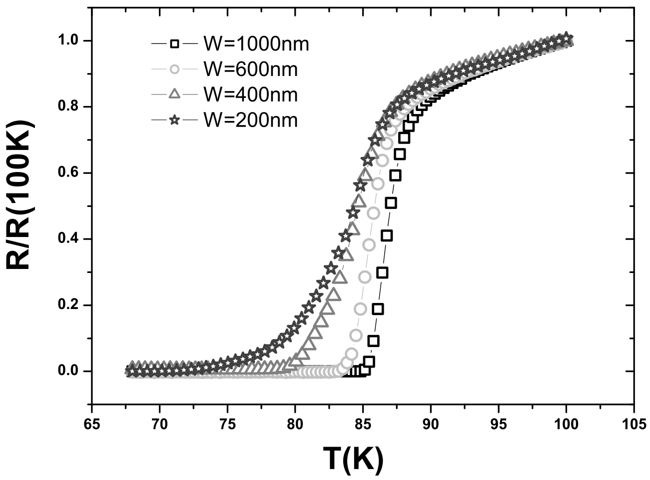

Figure 5.5: In the figure are reported the resistance versus temperature of five samples with different widths.

tions belonging to samples with different width and patterned on the same film. The widths of samples as function of the symbol are: 1000nm(squares), 600nm(circles), 400nm(triangles), 200nm(stars) respectively. The critical transition temperatures decrease as the width of the sample reduces in agreement with all data available in literature ([34] and references therein). Also the broadening of the transitions increases when the width of the channel is reduced. We estimate the width of a transition counting from the first bending of the R(T) (the knee of the curve) down to the zero resistance state. The transition of the 1000nm wide bridge has a tail 3 kelvin long, while the transition of the 200 nm wide bridge is about 16 kelvin broad. The critical temperature of the wider bridge is 85 Kelvin, just 2 kelvin lower than the critical temperature of the unpatterned film, while the T_C of the narrower bridge is 71 kelvin. Furthermore the continue decreasing of an R(T) indicates that the YBCO of the sample presents a certain degree of homogeneity [23]. This feature of the R(T) is relevant especially when the curve is used to study thermally activated dynamics [9],[5]. For instance the R(T)'s in figure 5.5 are a clear example of homogeneity of the samples. The broadening of the curves can be addressed just to the shrinking of the channel width. Although the processing can still be improved the scaling of T_C versus the channel width along with the homogeneity of R(T)'s place the presented results among the best outcomes in the literature of YBCO nanostructures [37], [36], [8].

5.3.1 The effects of heating and aging on the resistive transitions

The superconducting properties of the YBCO depend on the oxygen concentration [21], [10]. The change of oxygen concentration manages the hole doping and therefore the robustness of superconductivity of nanostructures. As already mentioned the principal cause of oxygen desorption is due to the heating produced during the ion milling process. Since each nanostructure is protected by a gold cup layer during the ion milling, the damage affects mostly the sample edges. In agreement with other authors [9] the sample is likely composed by a series of regions characterized by its own critical temperature/oxygen content. In figure 5.6 is reported an example of a resistive transition characterized by an inhomogeneous loss of oxygen(left). The sample is a nanobridge 200 nm wide and 500 nm long, and a sketch of the possible critical temperature distribution in the sample is depicted in the right panel of figure 5.6. As opposed to the smooth resistive transition of the 200 nm wide nanobridge presented in figure 5.5, the R(T) of figure 5.6 presents a series of bumps. The first one, that points out T1, can be associated to the superconducting transition of the leads, whereas the other two(T2, T3) refers to the transition of more underdoped zones sited in the nanostructure.

However every sample is affected by aging and whatever is the initial quality of a nanostructure after the fabrication, its performances tend to get worse. The main cause of samples aging is the water contained in the air. For this reason the patterned chips are usually kept in vacuum and in presence of silica gel that absorbs the residual humidity to further reduce this effect. In order to study the stability on the patterned samples we left aging a chip to be damaged by air humidity for seven months. The effect of aging on a nanostructure can be observed in figure 5.7 where are reported the resistive transitions of four samples with different widths. In this figure the black curves have been measured in the same month (march 2008) instead the red curve has been recorded seven months later the fabrication. The information on the aging is expressed by the shift of the knee of the red R(T). The R(T) knee identifies the transition of leads which are surfaces 1000 times bigger than the nano-sample. The knee is an optimal reference to investigate the effect of aging because it refers to those parts of the sample whose superconductivity is not affected by the fabrication process. In this case the loss of oxygen has produced a decrease in critical temperature of roughly five kelvin. By using the relationship between the critical temperature and the hole doping(p) [10], we can express the aging in terms of a change in p. The critical temperature depends parabolically on p,

$$Tc(p) = Tc,max\left[1 - 82.6\,(p - 0.16)^2\right]. \tag{5.3}$$

and the maximum critical temperature is obtained for a hole doping of

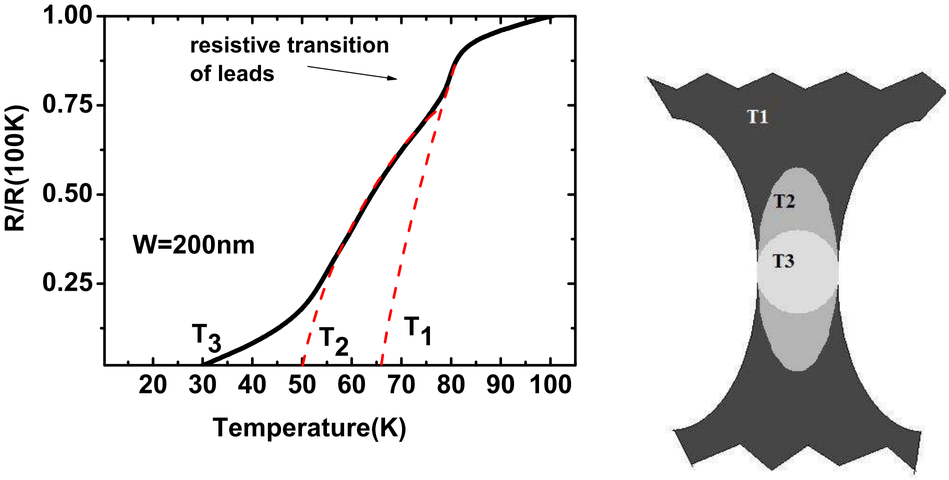

Figure 5.6: Left panel: R(T) of a nanobridge 200 nm wide. T_1 points to the transition of superconducting banks, whereas T_2 and T_3 represent the transitions of two regions inside the nanobridge each one characterized by its own oxygen content. The red lines are guide for the eye. Right panel: Sketch of the nanobridge referred to the R(T) reported in the right panel, at each color is associated a different oxygen content(see text).

0.16 (figure 5.8). By fixing Tc,max=90K, the reduction of the leads T_C from 88K to 83 K corresponds to a decrement of "p" of about 8%.
The aging affects so slowly the performances of a sample that it can be *per se* a way to control the sample doping. A possible way to block the aging is to deposit a thin insulating film on nanostructures after the accomplishment of fabrication.

5.4 Resistive transitions in magnetic field

An external magnetic field tends to suppress the superconductivity. The critical transition temperature and supercurrents decrease when a magnetic field is applied to the system. Within the BCS framework a magnetic field affects the spin and angular momenta symmetries of Cooper pairs and essentially it stimulates the decoupling of electron pairs [1]. In fact the literature is plenty of papers showing the broadening of the resistive transitions in presence of a perpendicular magnetic field [11],[5]. In figure 5.10 is reported this effect on a YBCO single crystal. As opposed to thin films some measurements on superconducting nanowires have shown enhancement[22][9] or even activation of superconductivity in presence of a magnetic field. In both cases

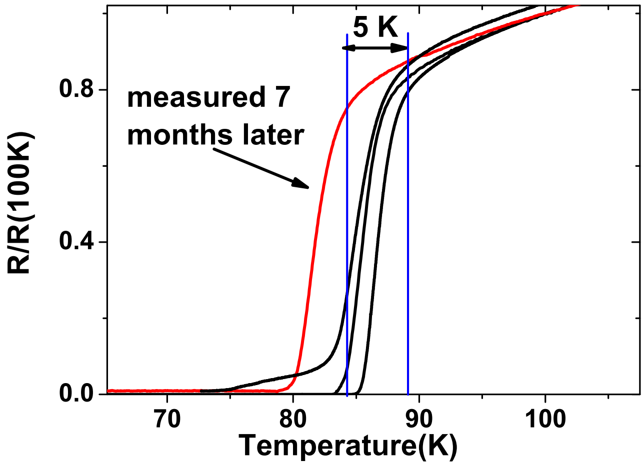

Figure 5.7: The nanostructures, whose R(T)'s are presented in this picture, have been let to degrade under the effect of a free exposition to the air. The red R(T) has been measured seven months later the other black curves, which have been measured after the completion of the fabrication process. The five kelvin shift of the red knee with respect the black ones is a fingerprint of the sample aging.

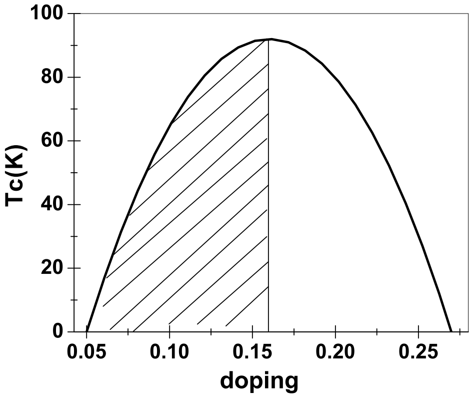

Figure 5.8: Dependence of the critical temperature as function of the doping(equation 5.3).

the mechanism is unclear and the theoretical background is controversial. Wei and co-workers claim that magnetic impurities can enable an enhancement of superconductivity [24], while Chen and collaborators [23] take into account also of a possible Josephson coupling among grains. The interpretation of Chen is particulary interesting because it is widely proved, through transport measurements, the Josephson coupling among YBCO grains [35]. The transport in granular means is expected to be further dependent on the intergrain coupling when the channel has the width comparable to that of a grain it self. In fact the superconducting-insulating transition is expected to be controlled by the ratio between Coulomb energy(E_C) and Josephson energy(E_J) among grains [25]. Targeting the interplay among E_J andE_C in a channel wide about as a grain we report the first analysis and comments on a resistive transition in presence of a perpendicular magnetic field. The YBCO bridge is 200 nm wide and 1 μm long and it is immersed in a magnetic field of 90 mT. The field was directed perpendicular to the transport direction as sketched in figure 5.9, and it penetrates everywhere in the bridge because the Pearl length[1] is wider than the bridge width. Following the same measurement technique reported in reference [12] we have periodically switched on and off the magnetic field, recording the sample response as function of the temperature. This technique allows to investigate the variations induced by a magnetic field on the R(T) ruling out any effect induced by the time variation of temperature. The intervals in which the field was on (or off) are about 300 mK. As opposed to outcomes of Tinkham [11], reported in figure 5.10, the resistance does not broaden uniformly. The sample manifests two separated reactions to the field, the first in correspondence of the leads transition and the second occurs when the nanobridge is becoming superconducting. Hence it has been found a temperature range in which no effect of the magnetic field is observed. The same type of measurement has been applied also to another nanobridge achieving the same result. The phenomena is quite robust and reproducible. In figure [5.11 a)] is reported the zero field R(T) of the nanobridge. The blue and the red segments point the intervals in which has been observed a reaction to the field. A zoom of the R(T) in magnetic field in the temperature range of the leads transition is depicted in figure [5.11 b)]. For clarity in the figure have been written the times when the field has been switched on or off either. It is evident that the resistance between 86 K and 85 K tends to increase while it decreases from 85K and 84 K. In the range of temperature between 84K and 82K the response is very reduced and substantially negligible. Below 81.5K the curve starts to widen (figure 5.11 c)), reproducing the expected dynamic as in the case of the YBCO single crystal 5.10. We are interested into this separate response of leads and of nanobrige. What can be noticed, for now, is that the shape of the R(T) unaffected by the magnetic field shows a concavity. Simulations on the YBCO transport has proved that this shape in the resistive transition is induced by an overdamped Josephson coupling between

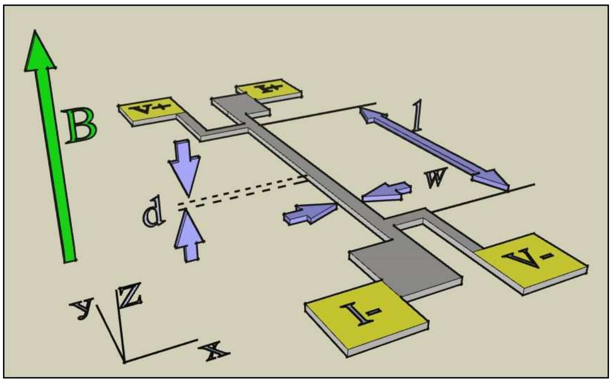

Figure 5.9: Sketch of the sample(not in scale). The figure shows the direction of the magnetic field with respect to the current flow.

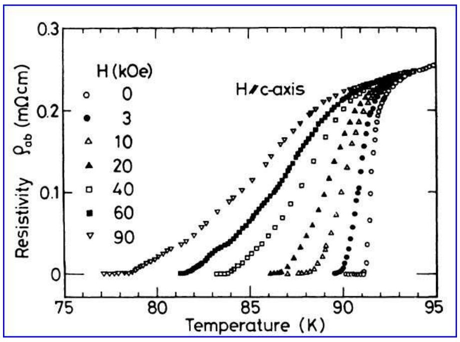

Figure 5.10: Dependence of the resistive transition of a YBCO single crystal on the magnetic field [11].

grains[15]. In this scenario we can deduce that only when the Josephson energy $E_j(T)$ is bigger than the Coulomb energy $E_C(T)$ the resistance is reactive to the field.

5.5 Evidence of weak link arrays transition

The epitaxial growth of YBCO thin film, inevitably implies the formation of grains[18]. This affects for several aspects the transport properties of the compound even when the sample is a couple orders of magnitude bigger than the main size of a grain [35], whose main transversal dimension is roughly hundreds of nanometers. The grain boundaries distribution manages the penetration of the magnetic field lines and practically the current flow inside a sample [5]. Furthermore many experimental evidences have emphasized the Josephson coupling among grains, for instance measuring the modulation of

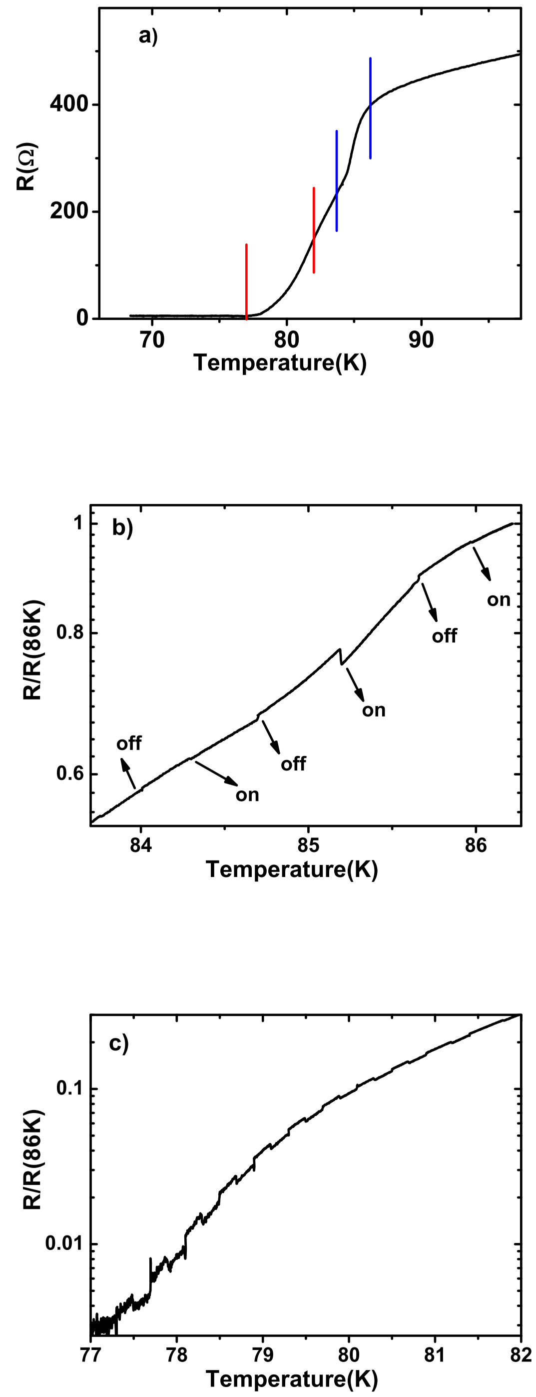

Figure 5.11: a): resistive transition of 200 nm wide and 1 μm long nanobridge. The blue and red segments point out the intervals of temperature in which have been observed a response to the magnetic field. b) zoom of the resistance in magnetic field (90mT) in correspondence of the pads transition. c) zoom of the resistance in magnetic field (90mT) in correspondence of the nanostructure transition. See the text for a clearer overview.

the critical current as function of the magnetic field.[35].
Lately has been published a paper [15] where some simulations state the possibility to observe the signatures of superconducting transition of weak link in a YBCO specimen. The YBCO is arranged as a two dimensional network of weak links. Every weak link is modelled as a nonlinear resistor that behaves as a Josephson junction. The sample shows the zero state when all the weak link arrays are superconducting. A simulation of a resistive transition of a YBCO layer constituted by 30×30 superconducting grains is reported in figure 5.12. The curve presents some jumps in the resistance in correspondence of the transition of the weak links arrays. The simulated resistive transition is normalized with respect the resistance value of the knee of the R(T). The jumps in the resistive transition are less than one percent. In full agreement with ref. [15] our findings state that the transport in narrow bridge($W < 300nm$) is mediated by weak links. The measurements are robust and has been observed in seven samples having different lengths and doping. The effect is remarkably evident when the resistance is smaller than 10 Ohm. In figure 5.13 are presented three examples of the phenomenon. For a better comparison with the simulation the curves have been normalized with respect the normal state resistance(R_N) of the nanostructure.

In figure 5.14 we compare the resistance versus temperature of the same nanobridge reported in figure [5.13, c)] with a simulation reported in [15]. The R(T) simulated has just the concave part of the curve more pronounced, but essentially matches with the measured curve. The simulation has been obtained conferring an overdamped character to weak links. Furthermore the sample show a Josephson like behavior in IV curves.
In addition we found an intriguing "noise" superimposed to the steps during the transition that, we speculate, is mainly due to the thermal fluctuations of the weak links. We also believe that these fingerprint in R(T)'s can have connections with the phase slips centers theory or with the fluctuation of domain structures either[37].
The large number of data collected make the weak links transition the starting point for wider investigations which involve several aspects of the transport in nanochannels, as the superconducting insulator transition[12], the anomalies in presence of a magnetic field[22], or the phase slipping dynamic [37], [36].

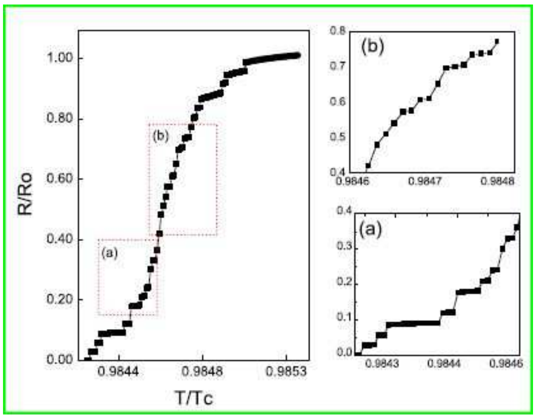

Figure 5.12: Simulation of a resistive transition of a two-dimensional network of $30 \times 30grains$. The calculation details can be found in the reference [15]

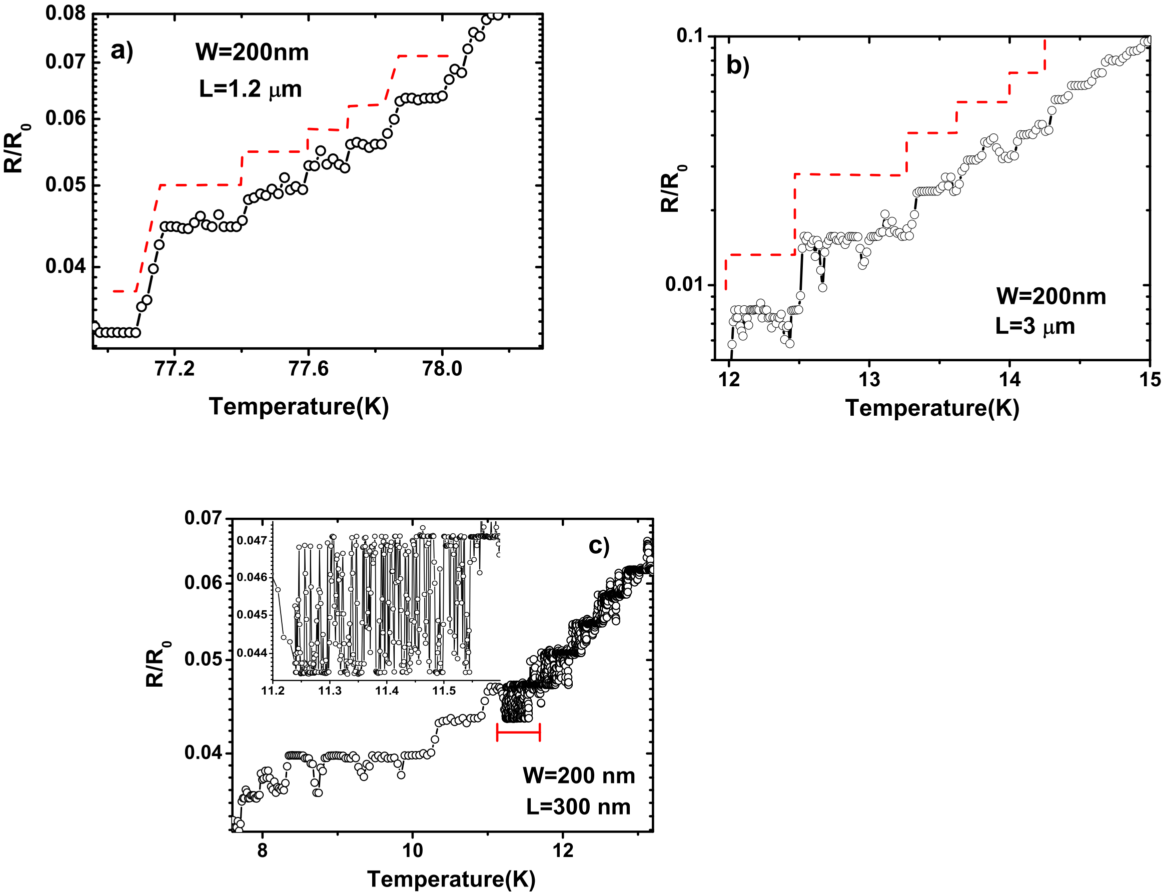

Figure 5.13: Zoom of three R(T) in log linear scale in proximity of the samples transition. All the samples are 200nm wide, whereas the length are a) 1.2μm , b)3μm, c)300nm. The staircase shape refer to the transitions of last weak links among grains. In panels a) and b) the red dashed lines are guide for the eye. Inset of panel c): enlargement of the resistance oscillations underlined by the red segment.

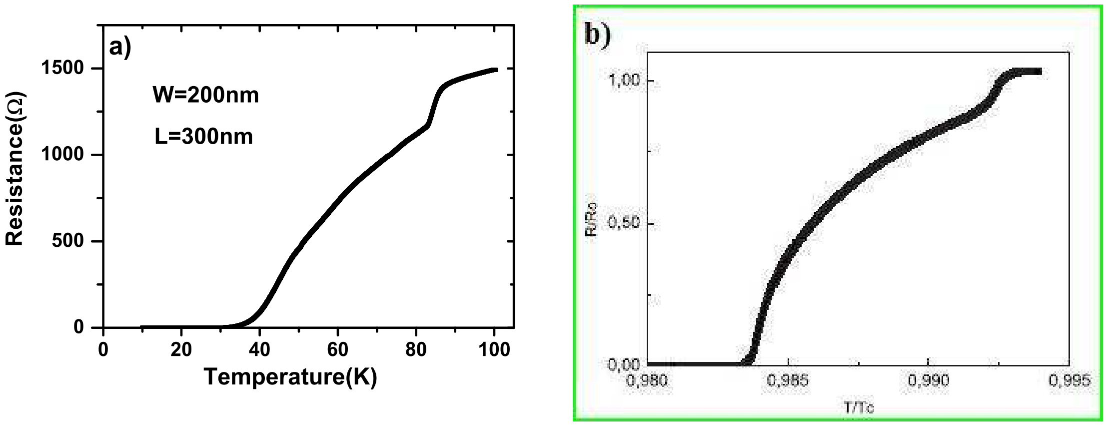

Figure 5.14: a) R(T) of a short nanobridge 200 nm wide and 300 nm long. b) Simulation of a resistive transition of a YBCO specimen. The sample is arranged as a two-dimensional network of 30 × 30 weak links. Every weak links are assumed to behave as overdamped Josephson junctions.

Bibliography

[1] A. Bezryadin, *J. Phys.: Condens. Matter*, vol. **20**, p. 043202, (2008).

[2] K. Y. Arutyunov , D. S. Golubev, and A. D. Zaikin, *Physics Reports*, vol.**464**, p 1 – 70, (2008).

[3] M. Zgirski and K. Yu. Arutyunov *Phys. Rev. B* **75**, 172509, (2007)

[4] G. Papari *et al. IEEE Tran. on appl. superc.* **19**, 183 (2009)

[5] J. T. Chen *et al.*, *Phys. Rev. Lett.* **58**, 1972 (1987)

[6] J. A. Bonetti *et al.*, *Phys. Rev. Lett.* **93** 087002 (2004)

[7] P. Mikheenko *et al.*, *Phys. Rev. B* **72** 174506 (2006)

[8] Ke Xu and James R. Heath *Nano Lett.* **8**, 3845 (2008)

[9] M. V. Pedyash *et al. Appl. Phys. Lett.* **68**, 1156 (1996)

[10] V. M. Matic *et al.*, *Supercond. Sci. Technol.* **21**, 075012(2008)

[11] M. Tinkham *Phys. Rev. Lett.* **61**, 1658 (1988)

[12] M. Zgirski *et al.*, *Phy. Rev. B* **77**, 054508 (2008)

[13] W. A. Little *Phys. Rev* **156**, 396 (1967)

[14] D. E. McCumber and B. I. Halperin *Phys. Rev. B* **1**, 1054 (1970)

[15] L. Ponta *et al.*, *Phys Rev B* **79**, 134513 (2009)

[16] H. E. Brandt *Rep. on Prog. Phys.* **58**, 1465 (1995)

[17] P. Bernstein *et al.*, *Phys. Rev. B* **78**, 054517 (2008); P. Bernstein *et al. Physica C* **468** 200 (2008) ; M. Pannetier *et al. Phys. Rev. B* **62** (2000);

[18] H. Hilgenkamp and J. Mannhart *Rev. Mod. Phys.* **74**, 485 (2002)

[19] P. Mazzetti *et al.*, *Phys. Rev. B* **77**, 064516 (2008)

[20] J. A. Bonetti *et al.*, *Phys. Rev. Lett.* **93** 087002 (2004)

[21] J. Orenstein *et al.*, *Science* **288**, 468 (2000)

[22] A. Rogachev *et al.*, *Phys. Rev. Lett.* **97** 137001 (2006)

[23] Y. Chen *et al.*, *Phys. Rev. Lett.* **103** 127002 (2009)

[24] T. C. Wei *et al.*, *Europhys. Lett.* **75** 943 (2006)

[25] A. T. Bollinger *et al.*, *Europhys. Lett.* **76** 505 (2006)

[26] M. Tinkham *Introduction to superconductivity* (2ed., MGH, 1996)

[27] A. T. Bollinger *et al.*, *Phys. Rev. Lett.* **101** 227003 (2008)

Chapter 6

Critical current densities and I-V curves

In the field of low temperature superconductors (LTS) Likharev[6] recognized three "characters" to the transport in small channels. As showed in figure 6.6 the typology of transport depends just on two ratios, L/ξ and W/ξ, where ξ is the coherence length, L is the length and W is the width of the channel respectively. It is relevant observing that the transport/dissipation in LTS weak links is just function of one characteristics length. Also the vortex dissipation dynamic, whose energy scale Φ_0^2/λ_L [1] is by definition fixed by the London penetration length λ_L, is delimited in figure 6.6 in an "area" proportional to ξ^2. This is possible because the LTS's are characterized by a ratio $\xi/\lambda \sim 1$. The HTS's are hard II type superconductors, characterized by a ratio $\lambda_L/\xi_0 \sim 100$. This property make difficult to turn the fig. 6.6 to HTS transport features. In fact the version of figure 6.6 adapted to describe the transport regimes of high critical temperature superconductors (HTS) is still missing. As opposed to LTS's, the HTS's transport regime is more subtle because it does not depend only on the geometry of the weak link. The very small coherence length[1] makes the transport of HTS strongly dependant on defects. Indeed the dissipative regime of vortex flow[5],[5] or the Josephson coupling among grains[35] are two relevant phenomena affected by defects as oxygen vacancies or twin boundaries respectively.
In this chapter are traced out the characters of the samples as function of the bridge geometry. However if we adopt the graph of figure 6.6 to describe the character of YBCO samples we state that the transport regime of all structures is always immersed in the "Abrikosov vortex motion" region. In fact in the following section we confirm this behavior through the investigation of critical current density as function of the temperature $J_C(T)$. In the successive sections addition we comment some IV curves in the limit of low and high excitation current. With low excitation current we mean that the maximum bias current(I) with which we feed the sample is comparable

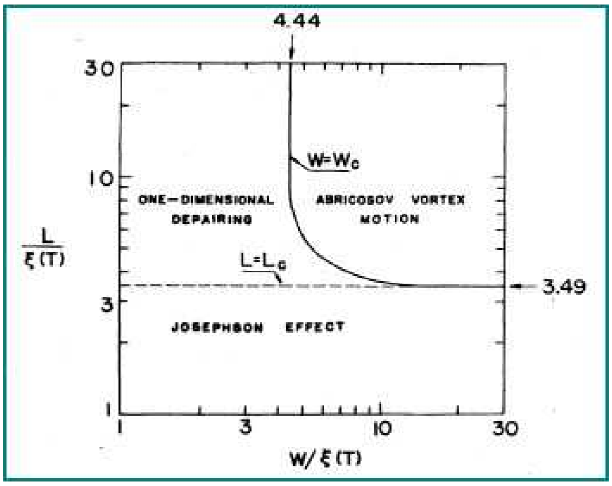

Figure 6.1: Transport characterization of low temperature superconductors weak links.[6]

with the critical one(I_C), while with high excitation current we mean that $I >> I_C$.

6.1 Critical current densities

The shape of critical current density curves $J_C(T)$ gives important information on the dissipation dynamic and are a measure of reproducibility of patterned samples.
In figure 6.2 are reported some $J_C(t)/J_C(4.2K)$ curves for samples with different widths. "t" is the reduced temperature $t = T/T_C$, where T_C is the temperature at which the current shows an Ohmic shape. All curves collected corresponding to samples having channel widths down to 300 nm sit on the same curve, while the trend for narrower bridges is different. The reproducibility of obtained results is impressive. The black curve in the figure 6.2 represent the theoretical trend of current when in the system dominates the "δl pinning" [5], [6], [7]. The pinning refers to the capability of defects to trap the vortices. The dependance on temperature of pinning potential is related to the activation dynamic of vortices and is relevant for the amplitude of the critical currents [5](see chapter 1). In HTS's can be individuated two sorts of pinning according to the disorder in the sample. When the pinning is caused by spatial variations of the charge it takes the name of δl pinning, where "l" stays for the mean free path otherwise the pinning is managed by the spatial variations of the critical temperature and is called δT_C pinning. Within the Ginzburg-Landau theory, the δl pinning refers to variations of the $|\nabla\Psi(\vec{r})|^2$, where $\Psi(\vec{r})$ is the order parameter, instead the δT_C pinning

derives from spatial variation of $|\Psi|^2$. The black curve in graph 6.2 is

$$J_C(T)/J_C(4.2K) = (1-t^2)^{5/2}(1+t^2)^{-1/2}. \tag{6.1}$$

By the optimal matching between $J_C(t)$ data with the theoretical trend we can deduce that as long as the channel width is larger than 300 nm the dissipation involves the vortex motion, so basically down to this size the samples dissipate like thin YBCO films [6],[39]. When the bridge width is reduced down to 200 nm or less a net change is observable in the $J_C(t)$ trend. The red data in the figure have been collected from bridges with different length, ranging between 1.5 μm and 300 nm, and as opposed to black data, decrease substantially linearly to zero. This is highlighted in the inset of figure 6.2 through a log-log graph. The red and the green curves are linear fit of the function

$$Jc(T)/Jc(4.2K) = (1-t)^p \tag{6.2}$$

with $p = 1.18$ and $p = 1.45$ respectively. The fits have an uncertainty of 1%. Between these two angular coefficients fall all the other linear trends. In agreement with other results[33] the average value of p is confident with the depairing current [1] within an error of 10%. The depairing current represents the maximum amplitude of $J_C(0)$ expected when the channel width is comparable with the coherence length. We exclude this hypothesis because the narrowest bridges presented here are hundreds coherence lengths wide. We are sure that the dissipation dynamic that limits the $J_C(0)$'s in 200 nm is still based on vortex motion. Indeed we have observed the penetration of vortices in bridges 200 nm wide through the analysis of the magnetoresistance[1]. In addition the the saturation of all critical currents at low temperature is a clear fingerprint of thermally assisted quantum creep of vortices [6], [7].

6.2 Current-Voltage characteristics at low bias current

The figure 6.3(left) presents the IV curves for several temperatures. The bridge is 200 nm wide and and 1μm long. As mentioned above the bridges of this size dissipate through vortex motion. In the right panel of figure 6.3 is reported an IV curve of a YBCO microbridge 23 μm wide[35]. The author proves that the dissipation dynamic in the bridge is due to flux motion[24]. The different size of the sample reflects in a higher critical current but the bending of the curve is substantially similar to those shown in the left panel of figure 6.3. In fact this scenario is also supported by the analysis of ref. [25] whose main findings are shown in figure **??**. The curvature of the voltage

---

[1] see the chapter "Macroscopic coherence in YBCO nanostructures"

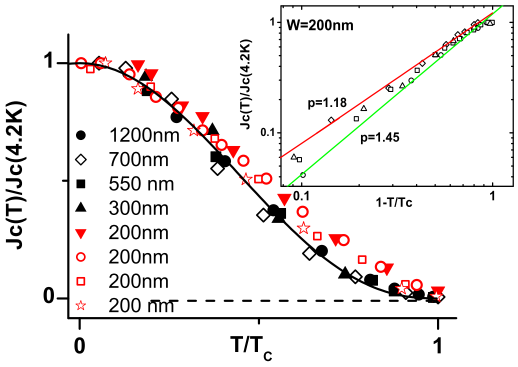

Figure 6.2: Critical current densities(Jc) of different YBCO nanostructures with different widths. The black line is the modulation of $J_C(T)$ as modelled by δl pinning theory. Inset: log-log graph of 200 nm wide bridges. The red line is the curve $(1-t)^{1.2}$

saturates reaching a dissipation state in which dominates the flux flow.
The IV curves shown in fig. 6.5 are quite different from the previous sample. This sample has the same width of the previous one but is only 300nm long. The behavior of the sample resembles the Josephson effect and in addition is also visible a slight hysteresis at low temperature. Likharev[6] suggested that the Josephson effect can switch on in weak links having both length and width smaller than the coherence length. These samples show as typical IV characteristics the curves shown in figure 6.6. Although the figure 6.5 is qualitatively in accordance with the trend reported in figure 6.6, the YBCO sample does not satisfy the weak link condition of Likharev at all. The most promising solution is that the fabrication process has degraded heavily the channel, hence the effective link is fairly smaller than what can be observed through the SEM picture.

6.3 IV curves at high bias current.

The IV curves of 200 nm wide bridges, show an intriguing behavior when the current injected pushes the voltage state at values as high as 500 mV. In figures 6.7 and 6.8 are presented the current voltage characteristics of two YBCO nanobridges patterned with the same geometry. The samples are 200 nm wide and 1.2μm long. The level of reproducibility is very high, in fact the nanobridges show the same dissipative dynamic. As discussed above, when the current is increased over the critical one a vortex motion dynamic

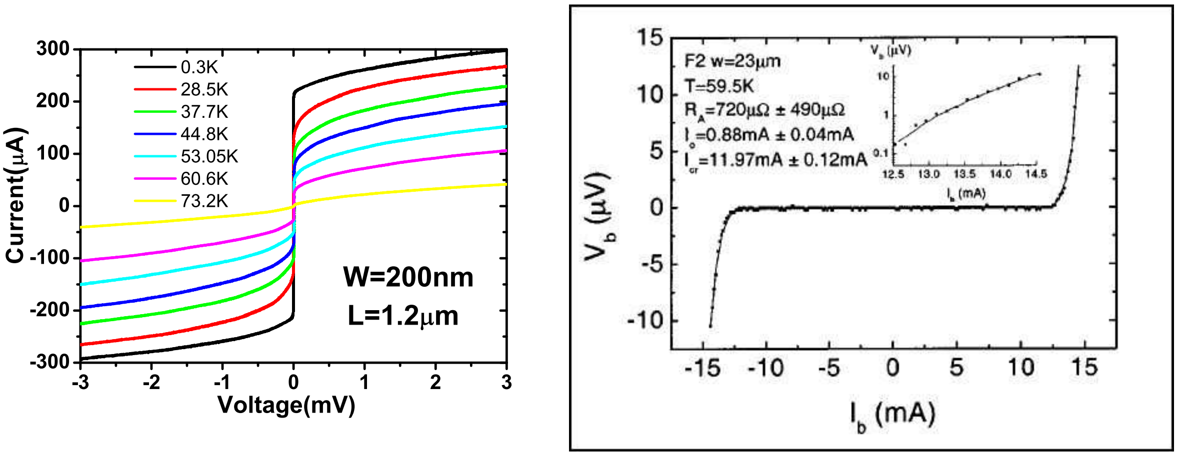

Figure 6.3: IV characteristics of a YBCO bridge 200 nm wide and 1.2 μm long.

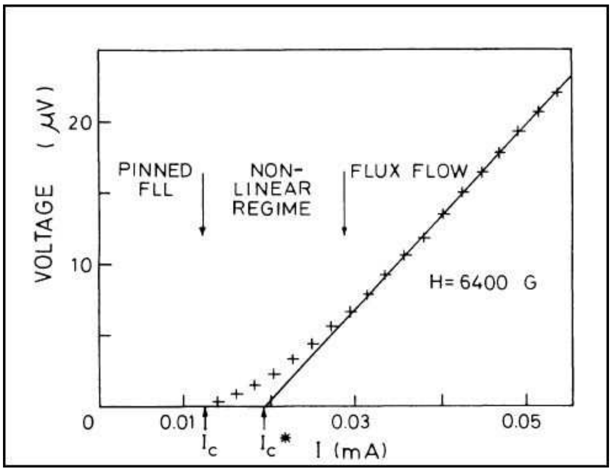

Figure 6.4: Definition of flux flow dissipation regime [25].

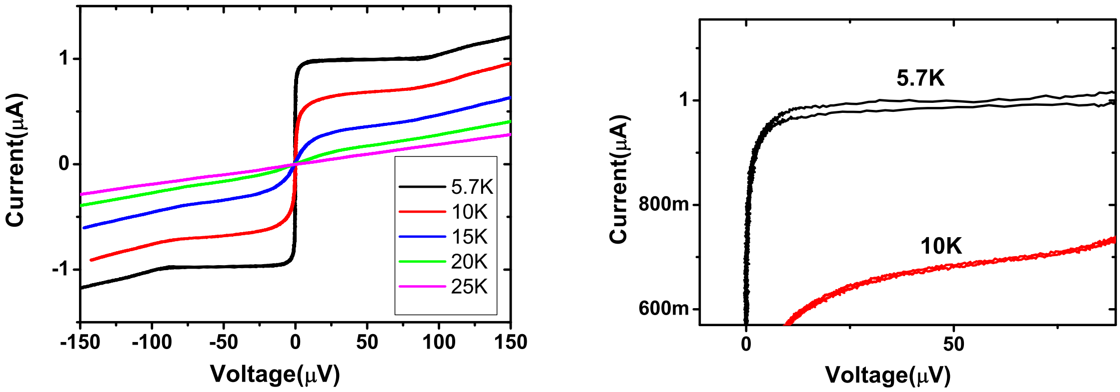

Figure 6.5: Left: IV characteristics of a YBCO bridge 200 nm wide and 300 nm long. Right: Zoom of the left image on the hysteresis of the IV curve at low temperature.

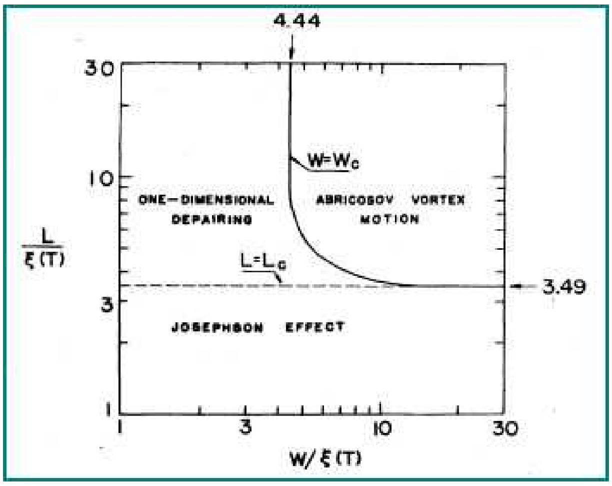

Figure 6.6: Theoretical dynamic of the IV curves for a weak link with a length and width lower than the coherence length. [6]

manages the dissipation. The voltage increases monotonically as long as the voltage state is lower than 20 mV$\sim$ Δ(the superconducting gap in YBCO). After the sample undergoes a non equilibrium state until it reaches quasi-Ohomic state. Indeed the resistive state after the switch is rather not linear, although the linear fit of the voltage branch after the switching is consistent with the normal resistance state $R_N = 1.6k\Omega$. Furthermore the curves present a robust hysteresis at low temperature. The two samples have comparable switching currents but differ for the hysteresis amplitudes.
Negative values of differential resistance, in both the switching and "retrapping" current can derive from an inappropriate choice of the shunt resistance. Our measurements are reliable but are a mixture between four and two probe measurements. More precisely, the amplitudes of supercurrents and also the resistance state after the switching are both not affected by the measurement technique, only the "phase diffusion" branch suffers this dependance[26]. Negative differential resistances have been measured, by two probes measurements in Sn or Pb granular nanowires [16] and have a solid interpretation in terms of phase slip centers or lines([37],[26],[18] and reference therein). To the best of our knowledge high bias current characteristics in YBCO nanowires have been studied only by other two groups [36] and [37]. Outcomes of these authors are presented in figure 6.9. In the image the left panel describes the IV curves collected in a 250 nm wide bridge while the right panel of figure 6.9 represent IV characteristics of a 100 nm wide bridge. In both papers the authors interpret the results mainly as due to the activation of phase slips centers(PSC)[17] or lines(PSL)[18] either, according to the dimensionality of the phase slipping mechanism. The novelty with respect to the precedent findings is that ours IV's characteristics show just one continuous phase diffusion dynamic characterized by an impressive hysterersis. Following the interpretation of [36] our nanobridges likely involve a single phase slip center. In agrrement with the Bonetti scenario our samples have a single domain structure[37]. Bonetti[37] speculates also in the role played by the layered structure of the compound to justify the steps in IV's. As support to this scenario Bonetti's samples are 100 nm thick, a double depth with respect the our samples. Our YBCO phase slip dynamic resemble other results obtained in niobium and MoGe nanowires [21], [20], [19]. In all these works the nanowires present a single phase slipping dynamic and all the IV's show a clear retrapping current. Although the literature is plenty of works on phase slipping in IV's the phenomena remains controversial. The difficult interpretation raises also by a lack in the reproducibility, for instance MoGe nanowires in ref. [19] experience a temperature independent hysteresis, but it does not happen in [21] even if the technique of sample fabrication is the same. We are going to continue our analysis also planning to perform measurements in samples with different geometries and thickness.

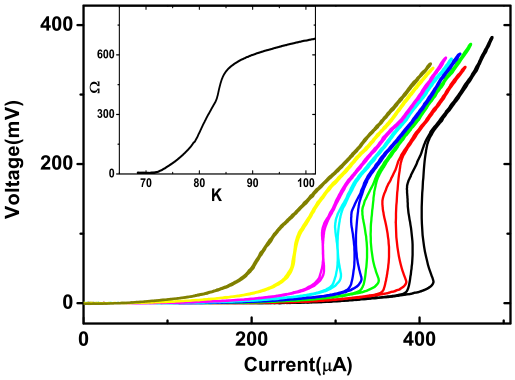

Figure 6.7: IV characteristics of a nanobridge 200 nm wide as function of the temperature.

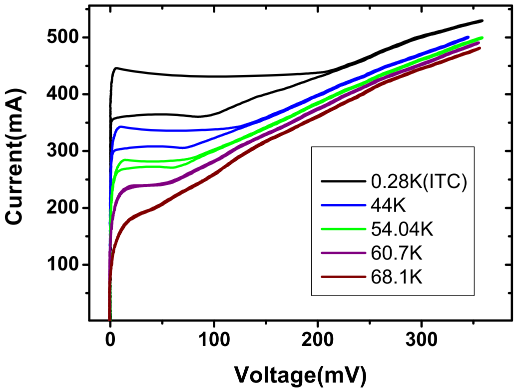

Figure 6.8: VI curves of a 200 nm bridge for several temperature. Inset: Resistance versus temperature of the bridge.

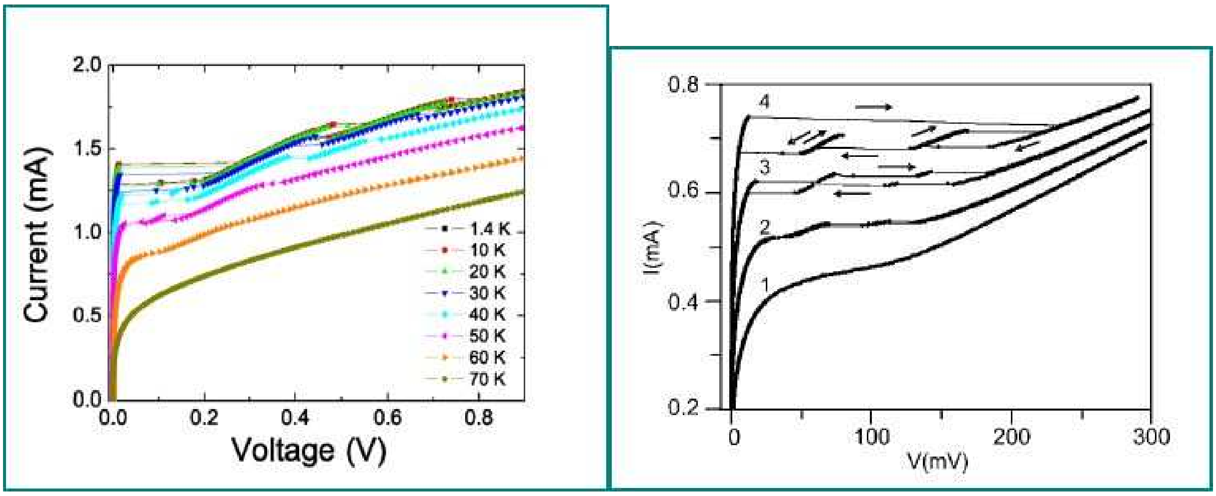

Figure 6.9: Two images of IV curves showing a phase slipping dynamic in YBCO nanobridges. The left image belongs to a nanobridge 250 nm wide [37], instead the right image is taken from [36] in which are studied the IV curves of 100nm wide bridge.

Bibliography

[1] M. Tinkham *Introduction to superconductivity* (2ed., MGH, 1996)

[2] K. K. Likharev *Rev. Mod. Phys.* **51**, 101 (1979)

[3] H. E. Brandt *Rep. on Prog. Phys.* **58**, 1465 (1995)

[4] E. V. L. de Mello *et al. Phy. Rev. B* **67** 024502, (2003)

[5] G. Blatter *et al. Rev. Mod. Phys.* **66**, 1125 (1994)

[6] *et al. Phy. Rev. Lett.* **72**, 1910 (1994)

[7] Hai-Wu Wen *et al. Phisica C* **241**, 353 (1995)

[8] G. Stan *Phys. Rev. Lett.* **92** 097003, (2004)

[9] M. J. M. E. de Nivelle *et al. Phys. Rev. lett* **70**, 1525 (1993)

[10] Z.G. Ivanov *et al. Low. Temp. Phys.* **30**, 203 (2004).

[11] J. Schneider *et al. Appl. Phys. Lett.* **65**, 2475 (1994)

[12] S. E. Romaine *et al. Appl. Phys. Lett.* **59**, 2603 (1991)

[13] M. V. Pedyash *et al. Appl. Phys. Lett.* **68**, 1156 (1996)

[14] A. J. J. van Dalen *et al.*, *Phys. Rev. B* **54**, 1366 (1996)

[15] R. Gross *et al.*, *Phy. Rev. Lett.* **64**, 228 (1990)

[16] S. Michotte *et al. Appl. Phys. Lett.* **82**, 4119 (2003)

[17] F. S. Jelila, *et al.*, *Phy. Rev. Lett.* **81**, 1933 (1998)

[18] A. G. Sivakov, *et al.*, *Phy. Rev. Lett.* **91**, 167001 (2003)

[19] M. Sahu *et al.*, *Nature Physics* **5**, 503 (2009)

[20] A. Rogachev *et al.*, *Appl. Phys. Lett.* **83**, 512 (2003)

[21] A. Rogachev, *et al.*, *Phy. Rev. Lett.* **94**, 017004 (1995)

[22] T. Senthil and M. P. A. Fisher *Phy. Rev. Lett.* **86**, 292 (2001)

[23] P. Bernstein *et al.*, *J. Appl. Phys.* **95** 2569 (2003);

[24] K. Fosseheim and A. Sudbø *Superconductivity Physics and Applications* John Wiley & Sons, (2004)

[25] F de la Cruz *et al.*, *Phys. Rev. B* **36**, 6850 (1987)

[26] J. Y. T. Wei *et al. Proceeding of Spie* **593210** (2005)

[27] J. A. Bonetti *et al.*, *Phys. Rev. Lett.* **93** 087002 (2004)

[28] P. Mikheenko *et al.*, *Phys. Rev. B* **72** 174506 (2006)

Chapter 7

Macroscopic coherence in YBCO nanobridges

The minimum channel width in which the superconducting transport can be sustained can be wide as about the coherence length(i.e. the size of a Cooper pair) [1],[8],[9]. The very short coherence length($\sim 1nm$)[19] makes the YBCO as optimal candidate to be nanostructured. Along the argument of the robustness of the superconductivity at nanoscale it is relevant to take in consideration the effect of a magnetic field. Indeed there are several experimental evidences, for low temperature superconductors, that the first critical field H_{C1} is enhanced when the superconducting bridge has a width narrower than the London penetration λ_L depth[18],[17]. Hence we can find two limits which identify the optimal width at nanoscale. Certainly the upper limit is λ_L while the lower one is a few times the coherence length[6]. The last condition was suggested by Likharev to prevent dangerous fluctuations of superconducting phase. In agreement with Tinkham[8], who fixed as safe lower limit for a nanowire 20 nm, we can state that the optimal width for a superconducting nanowire is comprised between 20 nm and 150 nm.
Within this issue we investigate the enhancement of superconductivity resulting from the reduction of the bridge width. We report the first analysis of the magnetoresistance(MR) fluctuations of two YBCO nanobridges patterned with different widths. The wider bridge is 450 nm and the second 200 nm wide respectively and are both 1 μm long. In the following are first reported the main benchmarks of the theoretical framework concerning the transport dynamic of nanobridges immersed in a perpendicular magnetic field and then are presented both the measurements and the first interpretation of data.

7.1 II type superconducting submicron channels in magnetic field

The magnetoresistance(MR) measurements of II type superconducting(SC) nanobridges are extremely interesting because they present features which are a pure effect of the finite size of vortices[16],[18],[17]. The resistance shows some minima when the magnetic field nucleates vortices whose size fits the channel width. This has been clearly shown by Tinkham[4] and Parks[16]which show that the fluctuations of the resistance gives hints on the dependance of the supercurrent on the magnetic field.

As the magnetic field is switched on the superconductor react by means of the Meissner effect. In a bulk II type superconductor when the field reaches the value $H_{c1} \approx \Phi_0/\lambda_L^2$[1] the magnetic field lines can penetrate the superconductor in shape of vortices and consequently the kinetic energy(supercurrents) decreases. In the limit of $H \sim H_{C1}$ the penetration length of the magnetic field can be thought as the radius of a vortex. Therefore it is rather intuitive that if the conducting channel is narrower than λ_L the magnetic field H_{C1} is not sufficient to nucleate fluxons. It is necessary a magnetic field $H'_{C1} \approx \Phi_0/W^2$, where W is the width of the channel, to generate vortices which can fit the channel width.
The last theoretical papers achieve the amplitude of the critical field sufficient to enter vortex in the bridge calculating the minima of the Gibbs free energy[13],[14]. For a SC nanobridge wide "W" and thick "d" the variation of the Gibbs energy for a single vortex in the bridge is [14]

$$\Delta G = -\frac{\Phi_0 \, B W^2}{16\pi \, \lambda_P} + \frac{\Phi_0^2}{8\pi \, \lambda_P} \ln \frac{2W}{\pi \, \xi} \tag{7.1}$$

where $\Phi_0 = h/2e$, $\lambda_p = 2\lambda^2/d$ is the effective magnetic penetration depth in thin films and is assumed that $\lambda_P >> W >> \xi$. The first term is associated with the interaction of the screening currents with the vortex, instead the second one represents the interaction of the flux line with an image one, of opposite sign, placed symmetrically out of the bridge [15]. For Likharev[13] the equilibrium configuration is reached for $\Delta G = 0$, that yields

$$B_L = \frac{2\Phi_0}{\pi \, W^2} \ln \frac{2W}{\pi\xi} \tag{7.2}$$

Therefore H_{C1} is increased from the thin film value ($\sim \Phi_0/\lambda_P^2$) of a factor W^2/λ_P^2. A YBCO sub micron bridge 300 nm can enhance its critical field H_{C1} of a factor 10, assuming a penetration depth $\lambda = 150nm$[19]. The reduction of the channel size strengthens the superconducting state because the increasing of H_{C1} represents also an enhancement of the critical current density[1]. As opposed to the Likharev interpretation, Clem[14] found the first critical field B_C by imposing a metastable penetration of the vortex.

The Clem condition implies to solve $\partial_x^2 G = 0$ with respect to the magnetic field, that yields

$$B_C = \frac{\pi\Phi_0}{4W^2} \tag{7.3}$$

B_C is smaller than B_L because of the term $\ln\frac{2W}{\pi\xi}$ that could be relevant for cuprates where the coherence length is a few nanometers. The two equilibrium configurations of Likharev(B_L) and Clem(B_C) can be observed in the figure 7.2[42].
In an infinite long SC bridge when the external magnetic field reaches the value, say, B_L the vortices penetrate the edge and sit at the center of the bridge. Raising the amplitude of the magnetic field, the equilibrium configuration is broken and is recovered when another array of vortices can be displaced in the bridge[21]. The vortex dynamic in a real superconducting bridge is clear for decades and is sketched in figure 7.1. Nevertheless this dynamic has been truly unveiled recently by means of imaging techniques as scanning SQUID microscopy[42] or scanning Hall microscopy [22]. The former experiment has been carried on niobium strips while the latter has observed the nucleation of vortices in YBCO strips. In ref. [42] has been calculated another critical induction

$$B_K = 1.65\,\Phi_0/W^2 \tag{7.4}$$

that corresponds to a Gibbs curve placed between the other two solutions B_L and B_0(see figure 7.2).
The penetration of vortex arrays in SC channel can be detect also by means of transport measurement. Typically the measurements are collected near T_C where the condensate is more sensitive to an external magnetic field and the thermally activated dynamics is enhanced[16]. A suitable excitation current(usually hundreds on nA's) leads to a voltage state that can be employed as a probe to detect the development of Meissner currents and hence to reveal the vortex penetration[17]. A magnetoresistance measurement performed on a SC bridge (W«λ) presents a quasi-periodic distribution of minima superimposed to a parabolic background(see fig. 7.3). The monotonic background is typically addressed to the flux flow in the macroscopic superconducting leads[17]. In these regions which are more extended than the penetration depth λ_P the mesoscopic effect does not show up and the voltage increase continuously[17]. In a real experiment there are other two important issues to take into account as the defects / grain boundaries which can create preferential paths for the magnetic field penetration and the effect of pinning of vortices[17],[18]. Both topics can affect the homogeneous penetration of the magnetic field in the bridge[22].

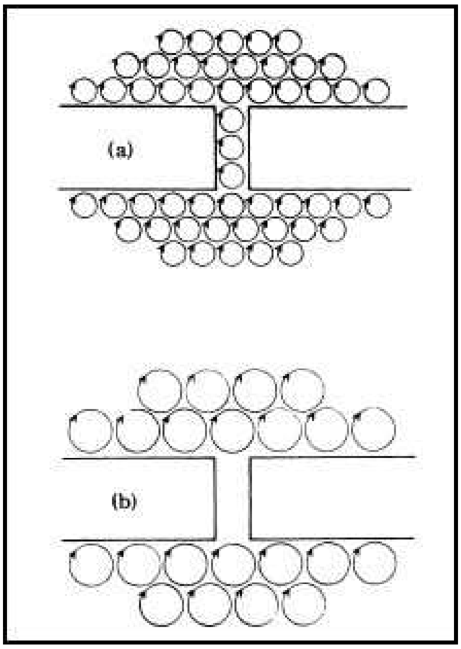

Figure 7.1: The two pictures sketch the vortices configurations a) when the external field is lower than the critical one b) when the external field matches the critical field [?]

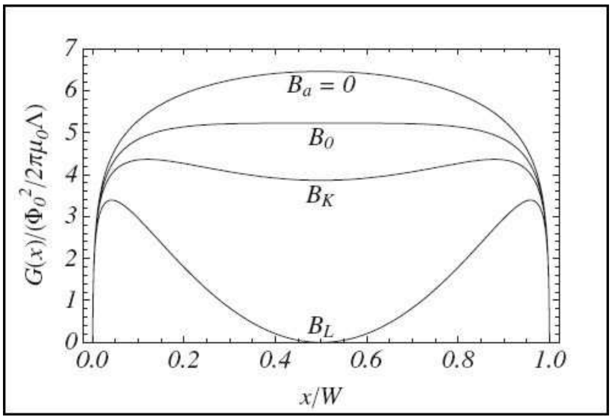

Figure 7.2: Gibbs free energy of an isolated vortex, by [42]

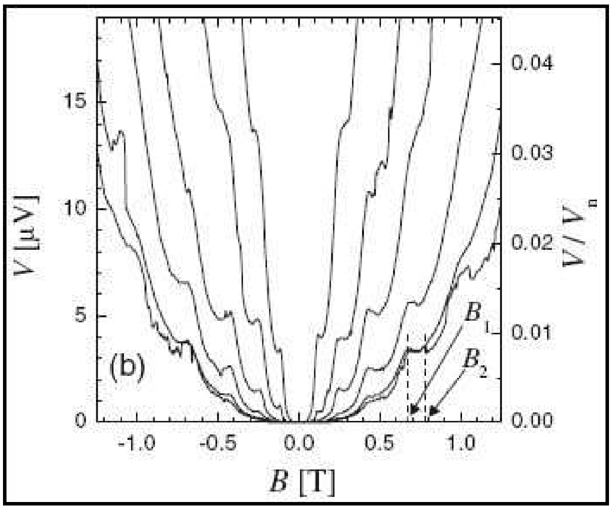

Figure 7.3: Voltage versus magnetic field of a niobium nanobrige 200 nm wide, by [42].

7.2 Magnetoresistance measurements of YBCO nanobridges

Up to date MR measurements have been performed only on low temperature superconducting(LTS) nanobridges [16], [17], [18]. Here we present the first outcomes on two YBCO submicron bridges. The sample A is a bridge 450 nm wide while the sample B is 200 nm wide. Both samples are roughly 1 μm long. The main findings of experiments are summarized in figures 7.4 and 7.5 for the sample A and B respectively. The two figures show in panels a) the resistive transitions, in panels b) are reported the V(I) curves at the same temperatures of the MR's, which are showed in panels c). The MR's have been collected by measuring the voltage with a lock in amplifier and injecting an ac current at 11.5 Hz in the samples. As already shown by other results [17], [18] the MR's present a modulation superimposed to a monotonic growth as function of the external field.

For both bridges the V(I) curves at lowest temperature, exhibit a net critical current I_C(17 μA for sample A and 4μA for the sample B) that, are substantially expired at the highest measurement temperature. Since the excitation currents used(2μA for sample A and 300nA for sample B) to feed the samples during MR's are smaller than I_C's we have also take into account of role played by pinning to the best interpretation of data [17],[22]. In order to improve the comparison among the curves collected at different temperatures we have them shifted and normalized. In figures 7.6 and 7.7 are reported the scaled curves of sample A and B respectively. In addition to the MR's of preceding articles here two types of minima are visible. These two species of minima differ for the way they disappear with the temperature. For instance the sample A evidences the "principal minima" at 22 mT, 75 mT and 145 mT[1], at all the temperatures under analysis, while the "secondary minima" are placed at 37 mT, 60 mT, 105 mT and 122 mT, which sit among the principal one and these tend to vanish raising the temperature. In particular the secondary minima turn into a plateau at the highest temperature. The sample B exhibits just two principal minima at 117 mT and 234 mT. In this sample the secondary minima also expire at high temperature but at 64 K the MR shape does not present any staircase shape as for the sample A. For both bridges we interpret the principal minima as the result of the entry of vortex arrays along the bridges. The interpretation is supported by calculating the mean extension of vortices as function of the applied field. Trivially we evaluate the mean vortex extension by using the distance "D" among Abrikosov vortices in a triangular lattice [5] that is

$$D \approx \sqrt{\frac{\Phi_0}{B}}. \tag{7.5}$$

The order of magnitude of formula 7.5, could be achieved also reversing one the critical field expressed in equations 7.2, 7.3 or 7.4. The curve of equation 7.5 is reported as a blue dashed line in the figures 7.6 for sample A and in figure 7.7 for sample B respectively. To the three principal minima of sample A (22, 75, 145)mT correspond a vortex diameter of $D_{A1,A2,A3}$=290nm, 165nm, 145nm respectively. These vortex diameters, or equivalently the distances between vortices, are exactly in agreement with our interpretation and automatically exclude any other configuration. Equivalent findings are obtained on sample B. The first minima corresponds to the entry of a vortex array whose diameter is D_{B1}=132 nm wide and the second principal minima is associated with a relative distance among the vortex arrays of D_{B2}=93 nm.

The dynamic of the secondary minima is simply addressed to the distribution of the pinning potential along the bridges. The pinning potentials tends to trap the vortices on defects. In epitaxial thin film the main defects are due to oxygen vacancies and twin boundaries [5], [35] (and reference therein). At low temperature pinning and defects affect the uniform distribution of magnetic field lines inside the bridge. Hence there are some regions of the bridges where the vortices can enter easier than others. Therefore the secondary minima mean that at lower temperature the array of vortices is not formed in one time but in several steps. The number of steps to form a complete array tend to match with the number of secondary minima between two principal minima. At higher temperature the pinning disappear and the nanobridge becomes "homogeneous" to the vortex penetration. In the wider

---

[1] the measurements do not prove effectively that at 145 mT the curve present a principal minimum, but this interpretation is in agreement with our findings. Furthermore whatever it is not a principal minima the whole interpretation remains self consistent.

bridge this manifests through the staircase shape of the MR in agreement with the measurement of reference [17]. Also the narrower bridge at the higher temperature presents substantially only the principal minima, which here are more robust in temperature.
There are also other features in the curves which can not be explained by using the previous interpretation. Indeed looking at the figure 7.7 the first oscillations(i.e. at 33 mT) are associated with a "vortex diameter" slightly bigger($\sim 250nm$) than the bridge width. In this case it is reasonable to think that the measurement is not only sensitive of the vortices in the narrower side of the sample but also of the fluxons entering between the superconducting leads and the bridge, which are regions slightly wider than the bridge. Somehow these penetrations can still be detected in measurements introducing a small modulation in the R(H)'s.
We have analyzed the data also performing the fast Fourier transform(FFT) of MR's at lowest temperature, where the pinning potential is fully active. In order to detect only the oscillating components we have subtracted the polynomial background to the curves. In figures 7.8 and 7.9 are depicted the FFT's of samples A and B respectively. The FFT of sample A is picked on a periodicity of about ΔH_1=22 mT instead FFT of sample B defines a main period of ΔH_2=60 mT. With these magnetic field we can obtain the size of the independent regions inside the bridges which are the sources of the inhomogeneous distribution of the magnetic field. By calculating $\Phi_0/\Delta H$ we find $S_1(\Delta H_1) = 9.410^{-14}m^2$ and $S_2(\Delta H_2) = 3.410^{-14}m^2$ for sample A and B respectively. As consequence of our interpretation $S_{1,2}$ identify the average surface where a single vortex can sit, and are on the order of $100nm^2$ in agreement with the typical grain size. The scenario that envisages the bridge as a puzzle of grains coupled by Josephson currents is broadly accepted [5], [35]. As matter of fact MR's curves of Josephson junctions networks resemble our curves [23], [24].
In conclusion the MR's measurements on YBCO submicron bridges show two type of minima. The principal minima identify the stable configurations of vortices inside the bridges. The secondary minima are robust at low field but tend to disappear at high temperatures. We argue that the principal minima are found when arrays of vortices are nucleated at the center of the channels, instead the secondary minima derive from the inhomogeneous distribution of pinning inside the bridges. In other words there are some regions in which the vortices can penetrate easier than in others. The secondary minima just represent the partial penetration of vortices in the bridge. The analysis of FFT's sustain this hypotheses and allows to calculate the main size of the indipendent regions composing the bridge ($\sim$ $100nm^2$). The secondary minima tend to flatten at high temperature because the pinning disappear and vortices(field) entry in the bridge uniformly.

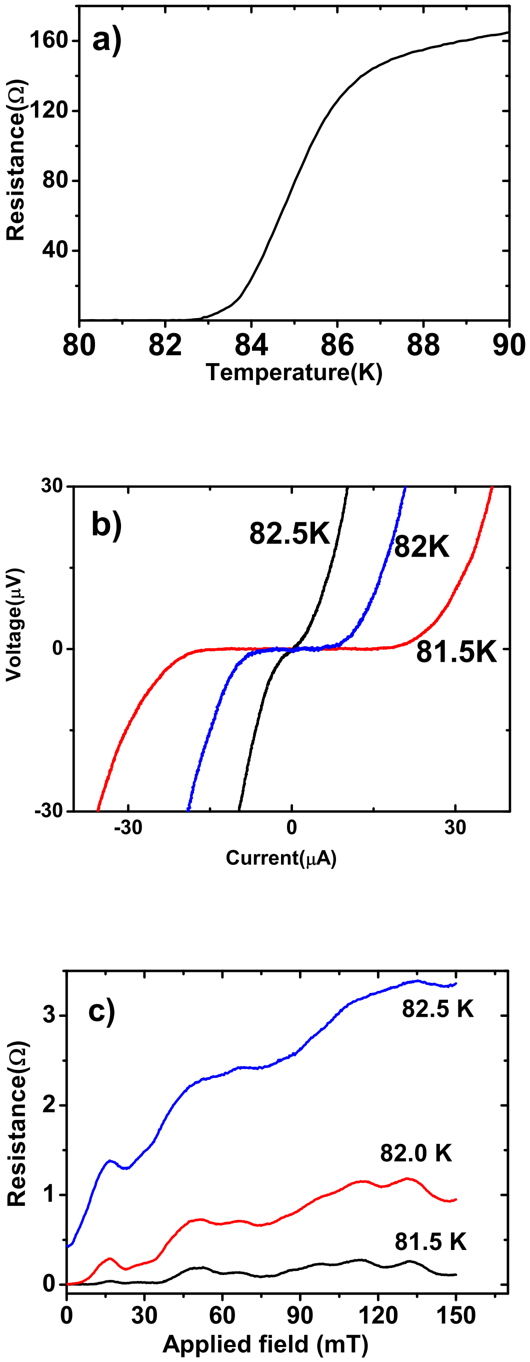

Figure 7.4: a) Resistive transition of a YBCO sub micron bridge 450 nm wide(Sample A). b) V(I) curves at temperatures close T_C. c) Magnetoresistance measurements at different temperatures.

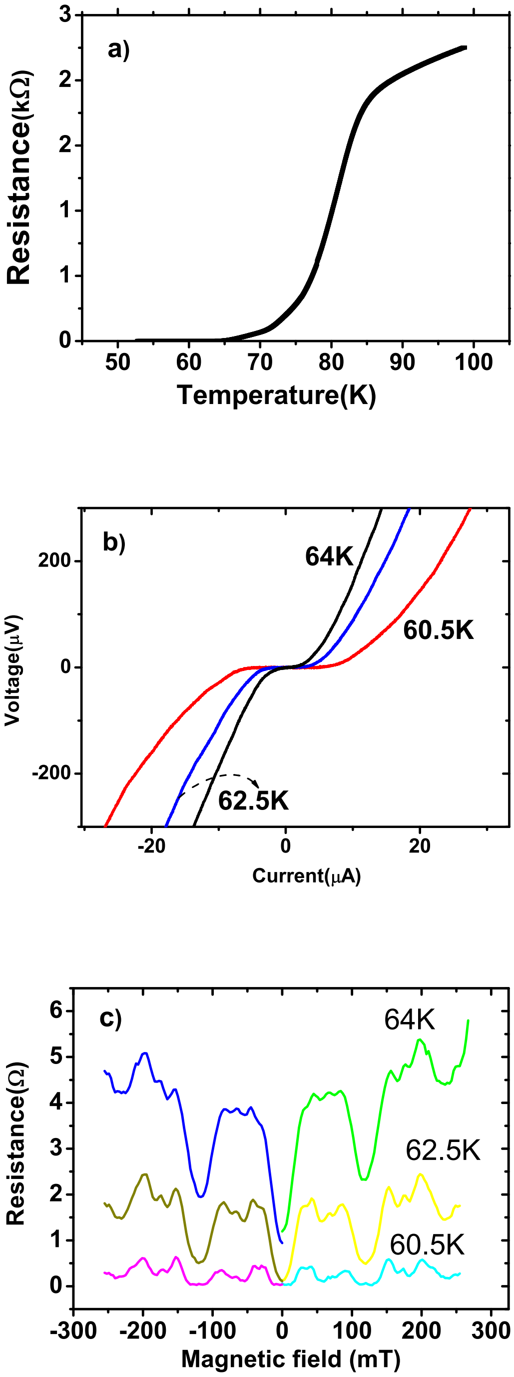

Figure 7.5: a) Resistive transition of a YBCO sub micron bridge 200 nm wide(sample B). b) V(I) curves at temperatures close T_C. c) Magnetoresistance measurements at different temperatures.

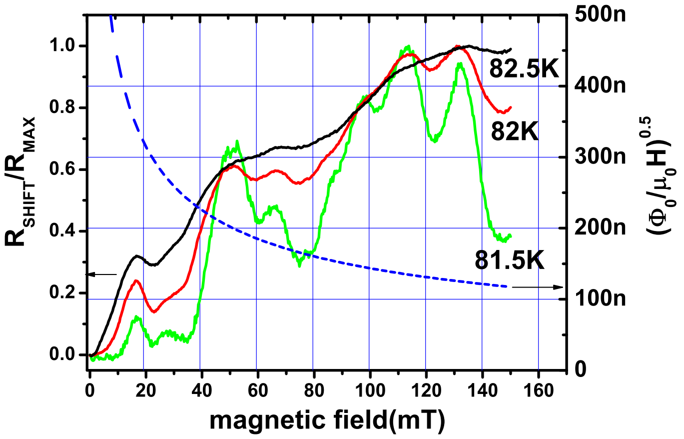

Figure 7.6: Sample A. The magnetoresistance measurements on the sample 450 nm wide have been normalized and shifted to improve the comparison. The blue dashed line is the function $\sqrt{\frac{\Phi_0}{\mu_0 H}}$.

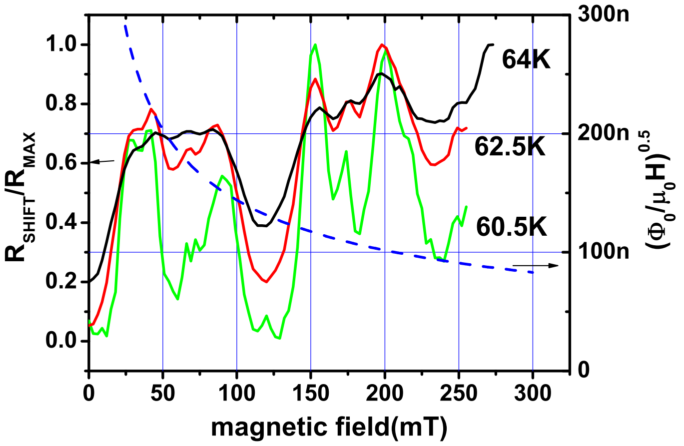

Figure 7.7: Sample B. The magnetoresistance measurements on the sample 200 nm wide have been normalized and shifted to improve the comparison. The blue dashed line is the function $\sqrt{\frac{\Phi_0}{\mu_0 H}}$.

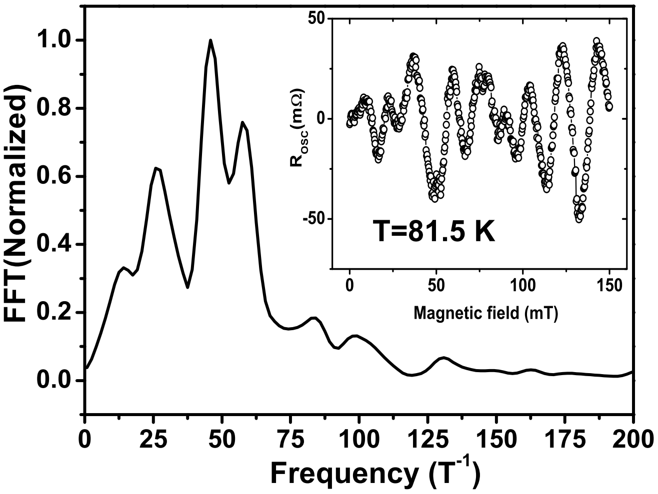

Figure 7.8: Fast Fourier transform of the curve shown in the inset. Inset: magnetoresistance of the sample 450 nm wide at which has been subtracted the polynomial background.

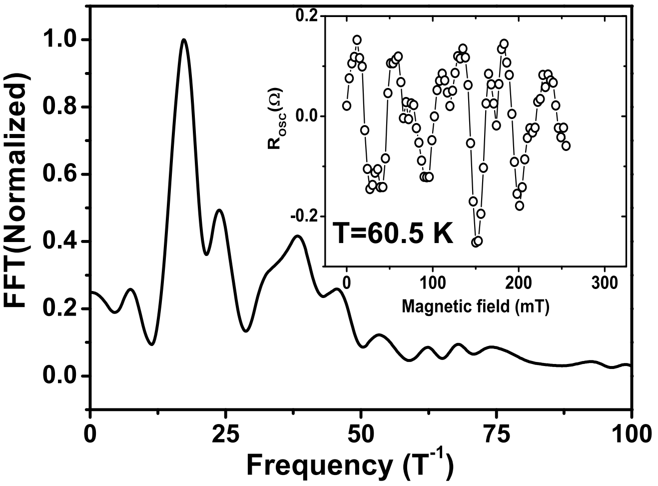

Figure 7.9: Fast Fourier transform of the curve shown in the inset. Inset: magnetoresistance of the sample 200 nm wide at which has been subtracted the polynomial background.

Bibliography

[1] A. Bezryadin, *J. Phys.: Condens. Matter*, vol. **20**, p. 043202, (2008).

[2] [nanolett] M. Bae *et al. Nano Lett.* **9** 1189 (2009)

[3] F. Altomare *et al. Phys. Rev. Lett.* **97**, 017001 (2006)

[4] M. Tinkham *Phys. Rev.* **129**, 2413 (1963)

[5] H. E. Brandt *Rep. on Prog. Phys.* **58**, 1465 (1995)

[6] K. K. Likharev *Rev. Mod. Phys.* **51**, 101 (1979)

[7] [lambda ybco] J. E. Sonier *et al. Phys. Rev. B* **76**, 134518 (2007)

[8] [quantum limit to phase coherence] M. Tinkham and C. N. Lau *Appl. Phys. Lett.* **80** 2946 (2002)

[9] [experimental limit phase slips] M. Zgirski and K. Yu. Arutyunov *Phys. Rev. B* **75**, 172509, (2007)

[10] M. Tinkham *Introduction to superconductivity* (2ed., MGH, 1996)

[11] P. Bernstein *et al.*, *Phys. Rev. B* **78**, 054517 (2008); P. Bernstein *et al. Physica C* **468** 200 (2008) ; M. Pannetier *et al. Phys. Rev. B* **62** (2000);

[12] A. T. Bollinger *et al.*, *Phys. Rev. Lett.* **101** 227003 (2008)

[13] K. K. Likharev, *Sov. Radiophys.* **14**, 722 (1972)

[14] J. R. Clem, *Bull. Am. Phy. Soc* **43**, 411 (1998)

[15] C. P. Bean *et al.*, *Phy. Rev. Lett.* **12**, 14 (1963)

[16] R. D. Parks *et al.*, *Phy. Rev. Lett.* **11**, 354 (1963); R. D. Parks *et al.*, *Phy. Rev. Lett.* **13**, 331 (1964)

[17] I. Kokanovic *et al.*, *Phy. Rev. B* **77**, 172504 (2008)

[18] U. Patel *et al.*, *Phy. Rev. B* **80**, 012504 (2009)

[19] J. E. Sonier *et al.*, *Phy. Rev. Lett.* **79**, 2875 (1963)

[20] H. K. Kuit *et al.*, *Phy. Rev. B* **77**, 134504 (2008)

[21] E. Bronson *et al.*, *Phy. Rev. B* **73**, 144501 (2006)

[22] G. Stan *et al.*, *Phy. Rev. Lett.* **92**, 097003 (2004)

[23] C. D. Chen *et al.*, *Phy. Rev. B* **54**, 9449 (1996)

[24] I. Elsayed *et al.*, *Phy. Rev. B* **80**, 052502 (2009)

Chapter 8

Novel Little and Parks effect in YBCO submicron rings

Multiply connected geometries are interesting systems because allow to investigate quantum coherent phenomena related to gauge invariance [1], [2]. Experimental cornerstones of quantum coherence in normal or in superconducting loops are the Aharonov-Bohm(AB) [3] and the Little and Parks(LP) effects ([4], [5], [6]) respectively. In particular the AB effect has demonstrated the undulatory nature of electrons in mesoscopic structures[2] while the LP effect has showed that the elementary charge of a superconducting condensate is a couple of electrons[1]. Low temperature superconducting(LTS) structures fabricated at mesoscopic scale, i.e. with dimension comparable with the coherence length (ξ_0) give access to a number of exciting experiments at nanoscale ([5]-[8]). Similar scaling regimes cannot be achieved in the case of high critical-temperature superconductors (HTS) because of the very small value of the coherence length in perfectly doped HTS ($\xi_0 \sim 1.5$ nm). Nevertheless the current performances of fabrication facilities allows to pattern linewidths of the order of tens of nanometers which in HTS open the way to experiments where the scales are comparable or smaller than the London penetration depth(λ_L), or the typical grain size in epitaxial thin film, or the possible stripe charge order correlation length (40nm)[9]-[37]. Rings on deep submicron scale are expected to shed light on different issues on HTS pairing mechanism [9]-[13] or to novel vortex state induced by the d-wave order parameter(OP) symmetry. Furthermore it had been recently claimed that low energy gapless quasiparticles could produce in d-wave rings a crossover from the typical h/2e oscillation period to h/e flux periodicity([12],[14],[15],[18]). We have measured, for the first time in a single YBCO nanoring, h/2e Little and Parks oscillations. In addition to the precedent LTS experiments performed on comparable annuli [19],[20], or on arrays of micron sized HTS holes[21], our findings provide clear evidence of a concentric vortex structure which results from the hard II type YBCO superconductivity. Our results focus on the OP anomalies which result in a non-uniform superfluid vorticity that is caused by the very short coherence length and the very large penetration depth, which in turn is larger than the width of rings arm.

8.1 Low magnetic field measurements

Isothermal magnetoresistances R(H) of submicron YBCO rings were performed at temperatures close to T_C. The acquired oscillations of resistance as function of the magnetic field allow to calculate, indirectly, the normal superconducting phase boundary [5],[6] in full analogy with the original LP experiment[4]. In HTS the detection of T_C vs. H oscillations can be very challenging since their amplitude (ΔT_C) is expected to scale with $(\xi_0/r)^2$. Up to now the unique successful attempt, was measured a $\Delta T_C \approx 40mK$ in a 50×50 array of $1\mu m \times 1\mu m$ holes in YBCO c-axis films [21]. According to the scaling of the T_C oscillations in our rings, with a mean radius of hundreds on nanometers, were observed critical temperature oscillations of about 500mK. A single ring configuration has the advantage to be just h/2e periodic[22], therefore it exclude in the R(H) oscillations higher spurious harmonics which can appear in multi holes structures[21]. Hence the systems constituted by array of holes can provide misleading interpretations for the current distribution associated to each single hole.

We shall report on measurements performed on four YBCO rings having nominally identical shape (internal radius r_i = 200nm, external radius r_o = 500nm), but different critical temperatures ranging from 74K to 19K. These samples allow us to cover a large part of the superconducting phase diagram in the under-doped regime. At lower T_C interference due to quasiparticles is expected to play a larger role also owing to the longer thermal length. To the best of our knowledge single-particle Aharanov-Bohm interference was recorded up to the maximum temperature of 20K on semiconductor rings with similar size [23].

We fabricated our nanostructures starting from 50 nm-thick (001)-oriented YBCO films grown on YSZ and $SrTiO_3$ substrates. The typical value of the surface roughness was lower than 3 nm. A 20 nm gold layer was deposited in situ to protect YBCO films during all following fabrication steps. In order to fabricate the nanostructures we deposited on top of the YBCO/Au bi-layer a 50 nm-thick Ti mask that was patterned by electron-beam lithography and lift-off. The exposed YBCO/Au bilayer was etched by ion-beam etching (IBE) while the sample was cooled down at -140°C in order to minimize oxygen loss from YBCO films. Subsequently the Ti mask was removed by a highly-diluted HF solution (1:20) and the gold layer by a short and low-energy IBE. Figure 8.1 reports a scanning electron microscope picture of one of the nanostructures (D1). The critical temperature of a device patterned using this procedure depends on the linewidth and on etching conditions. The more energetic is the dry etching and the smaller are the linewidths, the more depressed are the superconducting properties of nanostructures. This makes it possible to tune the ring doping level. We measured four rings, with an average radius of 350 nm and branch width ranging from 270 to 300nm. For all devices the transition temperature of the larger YBCO areas, i.e. wiring and pads, corresponds to that of the unpatterned film (86K). All samples showed the expected tail in the resistance vs. temperature curve associated to the superconducting transition of the submicron part of the device (see Fig.8.2 for device D1). Measurements were performed in a custom He3 cryostat. The temperature was monitored by a thermometer nested in to the sample holder. A PID program ensured the temperature stability acting on a heater close to the He3 pot. The electrical wiring were equipped by two stages of RC filters. One was at room temperature and the other was thermal anchored at 4.2 K. A further stage of copper powder filters was anchored to the He3 pot. Spurious external magnetic field was shielded protecting the sample by means of a trilayer cylinder composed by cryoperm, Pb and Nb foils. The magnetic shield is inserted the measurement dewar and is continuously cooled by the the liquid He bath. For all the measurements reported here we consider the differential resistance (dR = dV/dI) at zero bias as function of temperature and magnetic field. dR is measured by biasing the device with a small ac current (typically 300 nA) at about 11 Hz and detecting the corresponding ac voltage with a lock-in amplifier.

We measured the resistance as function of the magnetic field at several temperature above the critical one. The critical temperature is identified as the one at which the voltage drops to zero within the error of the instrument. In full agreement with the prescription of the LP experiment we calculated the phase boundary by the acquired magnetoresistances(see fig.8.3 for D2) and the R(T) curve [4]. In all devices ΔT_C oscillations show a periodicity h/2e as function of the flux enclosed by the ring average area A $=\pi r_{avg}^2$, as shown in Fig. 8.4 for D1. For our geometry this area matches with theoretical predictions for annulus of arbitrary r_i/r_o [24]. Consistently with similar measurements on the LP effect([4]-[6],[21],[25]), the periodic dependence of ΔT_C is superimposed on a parabolic background determined by the contribution to R(H) of the screening currents flowing in the arms of each ring[25],[26]. The amplitude of ΔT_C oscillations depended on the temperature at which the R(H) was measured. The maximum value of $\Delta T_C =$ 600 mK was recorded at 73K, and far exceeds the value predicted by theory for clean superconductors: $\Delta T_C = 0.14 T_C (\xi_0/r_i)^2 \sim 1mK$, assuming a zero-temperature coherence length $\xi_0 = 1.5$ nm. This large discrepancy is consistent with previous experiments in HTS [21] and conventional systems [25] and has been linked to a smooth R(T) since early times [25].

8.2 High field measurements

The behavior at larger magnetic fields (300mT) shows a few striking features when compared to existing data on LTS ([4]-[6],[25]). Data for D2 are shown in Fig. 8.5(down) (the polynomial background was subtracted). Oscillations have an amplitude modulation with at least three nodes before completely disappearing at high fields. This beating pattern results from the mix of two or more frequency components that are related to the inverse of the magnetic field. Fast Fourier transform (FFT) of the data shown in Fig. 8.5(top) yields all frequency components in the data. The FFT of data have been displayed as function of the effective radius $r_{eff} = \sqrt{\Phi_0/\pi\Delta H}$ where $1/\Delta H$ is the frequency provided by the FFT. The fast fourier transform procedure was successfully used in Ref.[26] to detect the characteristic periodicity arising from fluxoid quantization in two distinct concentric aluminum rings. In our work, apart from the expected peak matching the fundamental periodicity $\Delta H = \Phi_0/r_{avg}^2\pi$, we found additional peaks. They occur at the same position for all temperatures. Each FFT peak indicates the existence of a characteristic radius associated with flux quantization. To our knowledge this is the first report of such a multi-frequency behavior in a superconducting ring. It is made possible by the size of the ring in relation to the characteristic lengths of HTS. The "multiple-peak frequency" behavior must be ascribed to the finite width (W) of the ring arms which is here much larger than the superconductor coherence length. In LTS systems, T_C oscillations were detected in hollow cylinders and rings with walls or arms thinner than ξ. In this case the order parameter can be considered constant along the radial direction and depends only on the azimuthal angle. In the $r >> \xi$ regime, T_C and other thermodynamic properties, e.g. the magnetization, are strictly h/2e periodic. In HTS systems it is possible to have access to a regime where the radius of the ring is small enough to yield sizable LP oscillations, while the width of the arms still supports a significant variation of the order parameter along the radial direction. This sustains a discrete number of concentric independent domains where supercurrent density is different from zero. For a superconducting annulus close to T_C with arbitrarily wide arms, Ginzburg-Landau equations can be used to determine the order parameter (which, for the cylindrical symmetry of the sample, can be written as $\Psi(\vec{r}) = f_L(\vec{\rho})e^{iL\theta}$L(r), where θ and ρ are cylindrical coordinates (origin at the center of the ring). L is called winding number or vorticity and can be thought of as the angular momentum of the superfluid density. For W « ξ_0, $f_L(\rho)$ is a constant, while in our case, W » ξ_0, $f_L(\rho)$ varies along ρ. In our samples the lateral penetration depth exceeds W, so that the magnetic field in the structure can be taken equal to the external magnetic field. For the nucleation of superconductivity linearized GL equations can be used ([1],[5],[6]) and the most general solution is a linear combination of states with different winding number $\Psi(\vec{r}) = \sum_L a_L \, \psi_L(\vec{r})$ [27]. Each L(r)

is characterized by a different average radius and consequently a different periodicity in H. Coefficients a_L must be chosen by minimizing the free energy of the system and maximizing the flatness of Ψ (see Ref. [27]). If the external radius $r_o > \pi\xi_0$, $f_L(\rho)$ has nodes along the radial direction (between the minimum and maximum radius) with an overall spacing $\pi\xi$[28]. Consecutive nodes mark concentric domains in which the order parameter and the supercurrent are different from zero [28].
A stable solution with lower free energy may take place in a configuration with an order parameter having different vorticity in two domains of a ring separated by a zero-current line rather than the configuration with uniform vorticity[29]. In this case the total free energy of the ring will be a sum of contributions from domains with a different periodicity in H. On the basis of these approaches ([28], [29]), we associate each of the peaks in the FFT to the effective radius of one of the elements of a set of concentric current loops populating the ring, each labelled by different superfluid momentum, as schematized in Fig. 8.5(top). From each of the marked peaks in Fig. 8.5(top) we can calculate (g_n)and hence the radii $r_n = (\Phi_0 g_n/\pi)^{0.5}$. The ensemble of the peaks provided by the FFT at different field intervals allow to evaluate the mean spacing between the concentric domains. By means of FFT's analysis we achieve in the high magnetic field case($H = 90 - 250mT$) Δr =(21 ± 3nm) whereas we reach a radius spacing Δr =(28 ± 2nm) at low magnetic field ($0 - 90mT$). From this we can estimate the GL parameter $\xi = \Delta r/\pi = 12 \pm 1nm$. Finally from this ξ value, by using the expression for a clean superconductor $\xi_0 = \xi(1 - T/Tc)^{-0.5}$ with T = 70 K and T_C = 74 K, we obtain $\xi_0 = 1.5 \pm 1nm$. This findings are in agreement with the theoretical framework discussed in Ref.[30]. For a solution of GL equation with fixed vorticity L, the zero current line monotonously shrinks toward the internal radius of the ring with increasing magnetic field. The multiple-peak structure observed in FFT and the shift of the peaks to lower frequency at higher magnetic field closely resemble what experimentally observed and theoretically expected in Aharonov-Bohm multimode rings in the two-dimensional electron gas [31],[32]. We argue that this striking similarity holds because linearized GL equations, which model our system, are formally identical to the Schrodinger equation which describes single-particle states in a normal ring [1]. The main argument against the hypothesis of a role of quasiparticles interference is the absence of h/e periodicity [12]. Quantitative analysis also rule out explanations of multi-peaked FFT in terms of quasiparticle states with different angular momenta (and radii), as modeled in Ref. [32] for semiconductor multimode rings. In fact, in this case, the difference between two average radii associated with single particle states would be of the order $\lambda_F \sim 0.3nm$, where λ_F is the Fermi wavelength in YBCO (∼0.1nm).
In conclusion we performed LP experiment on several differently-doped submicron YBCO rings. Results indicate a multi-period dependence on H of the free energy close to T_C, consistent with a non uniform vorticity in the ring.

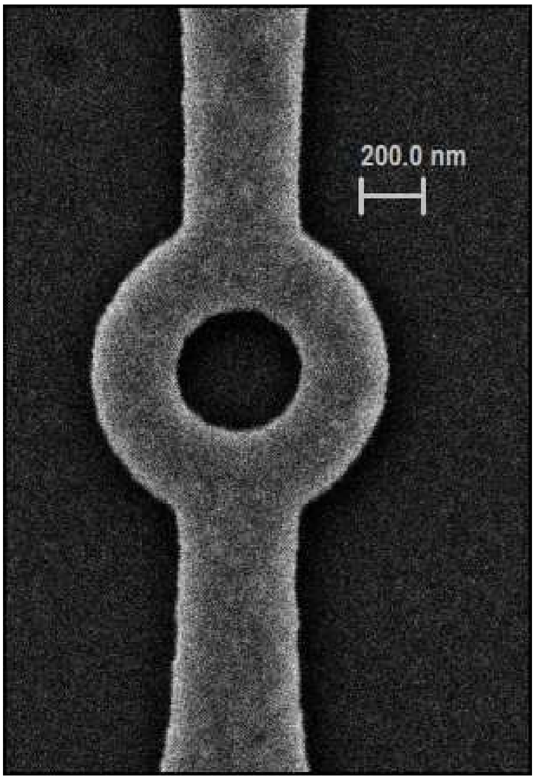

Figure 8.1: SEM image of a YBCO nanoring patterned on film a 50 nm thick. The arm of the ring is 200 nm wide and the average radius is 320 nm.

If confirmed this would be the very first observation of quantum effects due to mesoscopic confinement on HTS nanostructures. We believe these findings can provide useful guidelines for the design of nanoscale experiments targeting the investigation of fundamental properties of HTS.

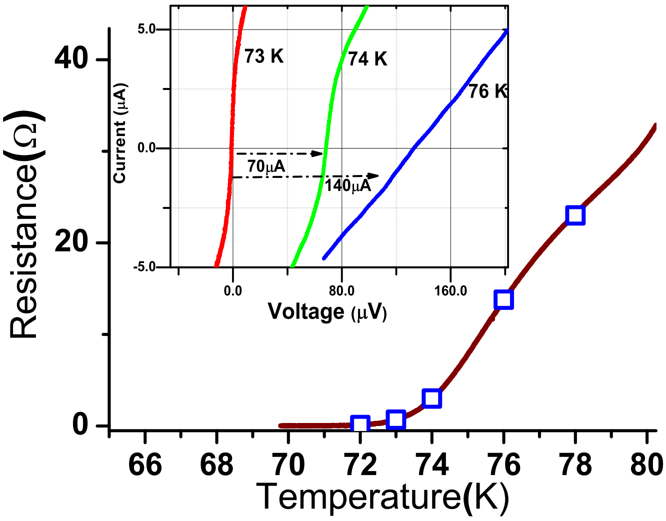

Figure 8.2: Resistive transition of a YBCO nanoring. The blue squares point the temperature at which the magnetoresistances have been collected. Inset: I-V curves measured at 73K, 74K and 76K. The last two curves have been shifted in current to improve the comparison.

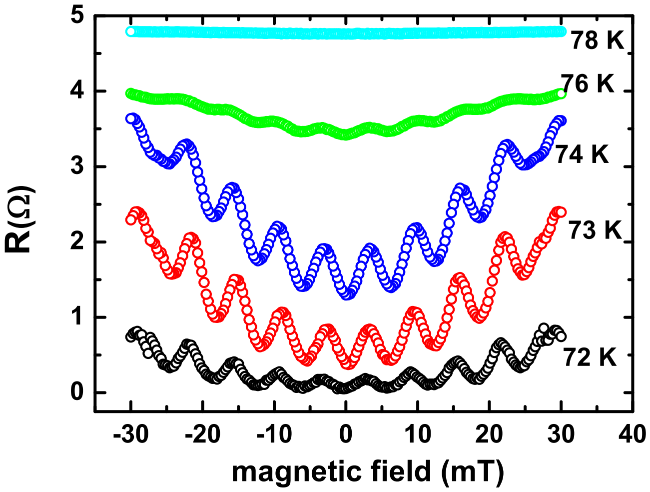

Figure 8.3: Magnetoresistance oscillations of a YBCO nanoring with an average radius of 320nm. The oscillation period is 55G.

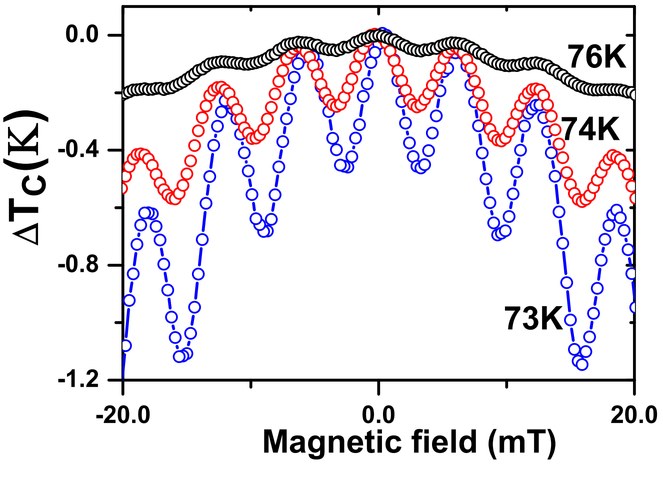

Figure 8.4: Little and Parks effect on a YBCO submicron annulus. The mean shift in temperature is $\Delta T_C = 0.5K$

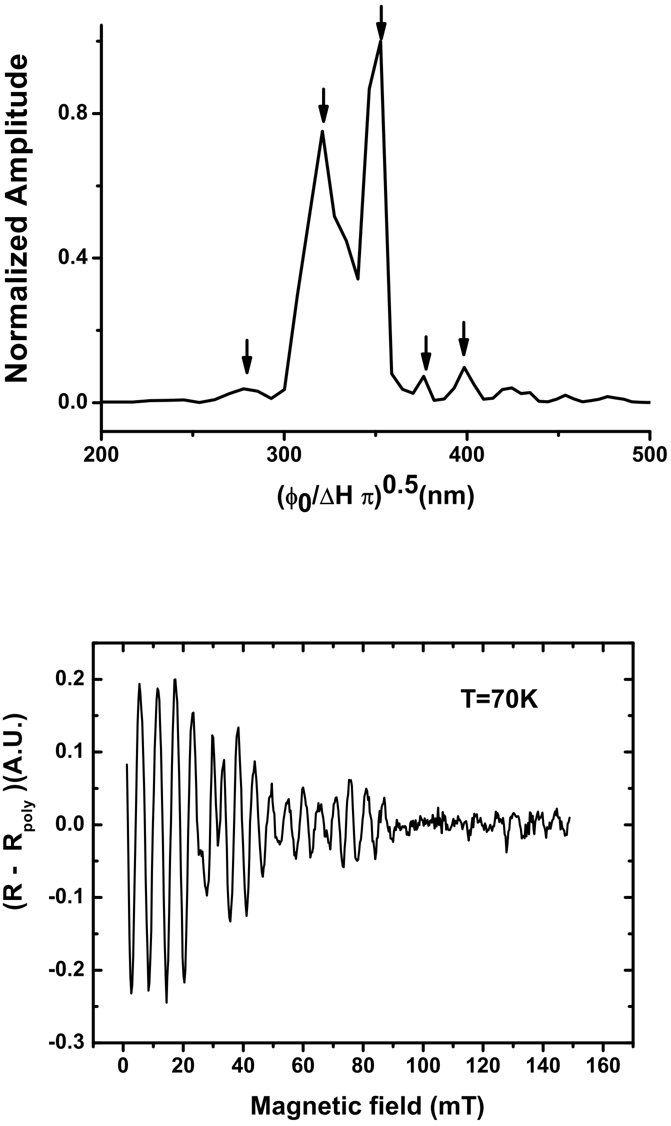

Figure 8.5: Top: FFT of a magnetoresistance(MR)(panel below) measured at 70K in the field range $H = (0 - 150)mT$. The x-axis is in function of the effective radius(see text). Down: MR acquired at 70K at which has been subtracted the polynomial background

Conclusions

A great deal of data collected on several samples with different geometries and doping make reliable relevant conclusions on the transport in YBCO nanostructures.

The fabrication based on the titanium mask has produced samples competitive with the best nanostructures available in literature ([33] and reference therein). The typical critical temperature(T_C) of samples is less than the 15% lower than the unpatterned films(87K). In agreement with all available data in literature ([34] and reference therein) the T_C's scale with the sample size while the critical current densities J_C remain substantially constant in the range of $10^6\, A/cm^2$. The dependence of J_C's on the temperature reveals that the dissipation dynamic is based on vortex motion. As long as the channel width is wider than 300 nm the $J_C(T)$'s do not differ from the $\delta\, l$-pinning dissipation dynamic measured in thin films of YBCO [38], [39], [40]. The analysis performed on 200 nm wide samples reveals a change in the trend of $J_C(T)$ which presents a linear decrease. Edge barriers [41],([42] and references therein) and grain boundaries[35] affect the fluxons dynamic and are the cause of the change in $J_C(T)$'s.

The analysis of the magnetoresistance(MR) of nanobridges and rings touches advanced concepts on vortex dynamics and macroscopic coherence in anisotropic d-wave superconductors. MR has been measured in channels of different widths and in rings enclosing the smallest areas ever investigated up to now for HTS, of the order of 300 nm. We have measured the Little and Parks effect(LPE) in YBCO nanoring. This is the first time that the LPE is recorded in a single high critical temperature superconductor(HTS) loop. The analysis of MR oscillations at higher field have exhibit novel effect which can be interpreted through a multi-vorticity state. These findings are in agreement with the hard II type character of the compound. We have also designed a set of experiments where MR oscillations have been investigated in different temperatures regimes by tuning the level of doping of the various nanostructures. We have found out in all conditions h/2e periodicity in the MR oscillations in analogy with classical systems. These experiments allow us to set an upper limit for the average radius of the ring, where any influence of the low energy quasi-particles on the flux periodicity can be ruled out[12].

Bibliography

[1] M. Tinkham *Introduction to superconductivity* (2ed., MGH, 1996)

[2] Y. Imry *Introduction to Mesoscopic Physics* Oxford University Press, (1997)

[3] Y. Aharonov, and D. Bohm, *Phys. Rev.* **115**, 485 (1959)

[4] W.A. Little and R.D. Parks, *Phys. Rev. Lett.* **9**, 9 (1962)

[5] V. V. Moshchalkov, *et al. Nature* **373**, 319 (1995)

[6] V. V. Moshchalkov *et al. Nature* **361**, 617 (1993)

[7] A.K.Geim *et al. Nature*, **396**, 144 (1998); A.K.Geim *et al. Nature* **390** , 259 (1997)

[8] Y. Liu *et al. Science* **294**, 2332 (2001)

[9] P. Mohanty *et al.*, *Physica C* **666**, 408(2004)

[10] E.W. Carlson *et al.* (Eds.), *The Physics of Conventional and Unconventional Superconductors*, Springer-Verlag, (2002), cond-mat/0206217

[11] J. A. Bonetti *et al. Phys. Rev. Lett.* **93**, 087002 (2004), H. A. Mook *et al. Phys. Rev. Lett.* **88**, 097004 (2002).

[12] F. Loder *et al. Nature Physics* **4**, 112 (2008). F. Loder *et al. Phys. Rev. B* **78** 174526 (2008); Y. S. Barash, *Phys. Rev. Lett.* **100**, 177003 (2008)

[13] C.C. Tsuei and J. R. Kirtley, *Rev. Mod. Phys.* **72**, 969 (2000)

[14] V. Vakaryuk, *Phys. Rev. Lett.* **101** 167002 (2008)

[15] V. Juricic, *Phys. Rev. Lett.* **100**, 187006 (2008)

[16] J.C. Wynn *et al.*, *Phys. Rev. Lett.* **87**, 197002 (2001); D. A. Bonn *et al.*, *Nature* **414**, 887 (2001).

[17] T. Senthil *et al.*, *Phys. Rev. Lett.* **86**, 292 (2001)

[18] T.C. Wei and P.M. Goldbart, *Phys. Rev. B* **77**, 224512 (2008)

[19] M. Morelle *et al.*, *Phys. Rev. B* 70 144528 (2004)

[20] V. Bruyndoncx *et al.*, *Phys. Rev. B* **60**, 10468 (1999)

[21] P.L. Gammel *et al.*, *Phys. Rev. B* **41**, 2593 (1990).

[22] J. Wei *et al. Appl. Phys. Lett.* **92**, 102502 (2008), Yu. Zadorozhny and Y. Liu, *Europhys. Lett.* **55712** (2001).

[23] F. Carillo *et al. Physica E* **32**, 53 (2006)

[24] V. G. Kogan *et al. Phys. Rev. B* **69**, 064516 (2004)

[25] R. P. Groff and R. D. Parks, *Phys. Rev.* **176**, 567 (1968)

[26] M. Morelle *et al.*, *Phys. Rev. B* **64**, 064516 (2001)

[27] V.V. Moshchalkov *et al.*, *Physica C* **207**, 307 (1993)

[28] G. Stenuit, *et al. Physica C* **332**, 277 (2000)

[29] H. Zhao *et al. Solid State Commun.* **125**, 59 (2003).

[30] S. V. Yampolskii *et al. Phys. Rev. B* **64**, 052504 (2001).

[31] J. Liu *et al. Phys. Rev. B* **48**, 15148 (1993).

[32] W. C. Tan and J. C. Inkson, *Phys. Rev. B* **53**, 6947 (1996). Tan, W. C. & Inkson, *J. C. Semicond. Sci. Technol.* **11**, 1635 (1996).

[33] P. Larsson *et al. Journal of Vacuum Science Technology* B 18(1), (2000)

[34] G. Papari *et al. IEEE Tran. on appl. superc.* **19**, 183 (2009)

[35] P. Bernstein *et al.*, *Phys. Rev. B* **78**, 054517 (2008); P. Bernstein *et al. Physica C* **468** 200 (2008) ; M. Pannetier *et al. Phys. Rev. B* **62** (2000);

[36] P. Mikheenko *et al.*, *Phys. Rev. B* **72** 174506 (2006)

[37] J. A. Bonetti *et al.*, *Phys. Rev. Lett.* **93** 087002 (2004)

[38] R. Griessen *et al.*, *Phys. Rev. Lett.* **72** 1910 (1994)

[39] A. J. J. van Dalen *et al.*, *Phys. Rev. B* **54** 1366 (1996)

[40] H. Wen *et al.*, *Physica C* **241** 353 (1995)

[41] S. Tahara *et al.*, *Phys. Rev. B* **41** 11203 (1990)

[42] H. K. Kuit *et al.*, *Phy. Rev. B* **77**, 134504 (2008)